

ABSTRACT

Dissertation Title: RESEARCH AND DEVELOPMENT OF LIQUID PHASE EPITAXY GROWN IRON GARNET THIN FILMS UTILIZING PLASMON RESONANCES FOR ENHANCEMENT OF MAGNETO-OPTIC EFFECTS

Garrett Seth Lang, Doctor of Philosophy, 2013

Dissertation Directed by: Professor of Engineering Isaak D. Mayergoyz
Department of Electrical and Computer Engineering

Plasmon resonance induced Faraday rotation enhancement in garnet films offers the promise for development of compact and higher performance polarization dependent optical devices. Enhancement of Faraday rotation has been achieved utilizing strong localized electric fields induced by the excitation of plasmon resonances in gold nanoparticles deposited on or in garnets. Experimental results are presented that reveal strong Faraday rotation enhancement in bismuth-doped garnet films with gold nanoparticles incorporated in or on the epitaxial films. The strength of the enhancement is governed by the thickness of the garnet films, the dimensions and separations of the nanoparticle assemblies, and the relative ratio between the height of the nanoparticles and the thickness of the films.

For samples with embedded nanoparticles, there have been noticeable effects on the magnetic properties of the films due to the presence of the embedded gold

nanoparticles. The embedding of nanoparticles in the films can be practically utilized to control the local anisotropy of the films. Special efforts have been made to improve the growth process and produce sub-micron thick films with thicknesses around 200nm to ensure that the induced electric fields are uniformly spread over the thickness of the films. At this thickness, nanoparticles have been incorporated on the surface of the liquid phase epitaxy grown garnet films rather than embedded in the films due to the low growth rate necessary to grow these films. New techniques have been developed to improve the accuracy of Faraday rotation enhancement measurements. Faraday rotation enhancement as high as 110% has been observed for samples with nanoparticle assemblies incorporated on the surfaces of the films but the enhancement depends on a number of factors and can be substantially lower. Stronger enhancement can be obtained by increasing the nanoparticle height to film thickness ratio as well as increasing the relative spacing between nanoparticles.

RESEARCH AND DEVELOPMENT OF LIQUID PHASE EPITAXY GROWN IRON
GARNET THIN FILMS UTILIZING PLASMON RESONANCES FOR
ENHANCEMENT OF MAGNETO-OPTIC EFFECTS.

By

Garrett Seth Lang

Dissertation submitted to the Faculty of the Graduate School of the
University of Maryland, College Park, in partial fulfillment
of the requirements for the degree of
Doctor of Philosophy
2013

Advisory Committee:

Professor Isaak D. Mayergoyz, Chair

Professor Romel Gomez

Professor Edo Waks

Professor Christopher Davis

Professor Lourdes Salamanca-Riba

©Copyright by
Garrett Seth Lang
2013

Dedication

I dedicate this dissertation to the following people:

- *My parents who taught me the importance of education and for all the love and support they have shown me along my journey.*
- *My grandfather Gerald Lang for encouraging me to further my education and pursue the field of electrical engineering.*
- *The memory of my grandfather Dr. Morton Fielding for teaching me to appreciate the arts and value education.*

Acknowledgements

I would like to take the time to thank all those who have given me the opportunity to work on this dissertation and who have helped me throughout my Ph.D. studies.

I would first like to thank my academic advisor, Professor Isaak D. Mayergoyz for his continued guidance and support over the last several years. From day one, he has seen my potential and believed in me, even when I had doubts. Through his wisdom, he has taught me what it means to be committed. He has always encouraged me to never give up and to work hard. Professor Mayergoyz has always gone above and beyond the call of duty to see that I succeed in the tasks at hand.

I would also like to thank Dr. Charles Krafft from the Laboratory for Physical Sciences for whom the research presented in this dissertation would not have been possible without. Dr. Krafft has been the backbone of my research and has provided me with a wealth of knowledge. He has been there for me as a helping hand, open ear, and source of advice throughout my studies. I am truly grateful for our countless discussions and the wisdom he has shared with me regarding the characterization and engineering of garnet films.

Additionally, I would like to thank Dr. Sergiy Tkachuk, my predecessor in the research on garnet films at the Laboratory for Physical Sciences for his involvement in my research and assistance in the development of my skills and knowledge of garnet growth and characterization from early on, as well as Dr. David Bowen for his help with gold deposition and assistance with the development of some of the experimental systems used in my research.

Lastly, I would like to thank all my family, friends and loved ones. None of this would be possible without their endless support. I would specifically like to thank my mother for always pushing me to do my best, my father for teaching me to always better myself, and my grandfather for encouraging me to follow in his footsteps and pursue the field of electrical engineering. Without the support and encouragement of my family and friends, I would not be where I am today.

Table of Contents

Dedication	ii
Acknowledgements.....	iii
List of Tables	vii
List of Figures.....	viii
List of Publications	xiii
Introduction.....	1
Chapter 1: Garnets and their Magnetic Properties.....	4
Crystal Structure	4
Magnetization	5
Macroscopic Origin of Magneto-Optical Effects	8
Microscopic Origin of Magneto-Optical Effects	18
Spin-Orbit Interaction	18
Light-Matter Interactions	19
Connection between Microscopic Phenomena and Macroscopic Values.....	20
Magnetic Interactions.....	22
Exchange Energy	23
Demagnetizing Energy.....	24
Zeeman Energy	26
Anisotropy Energy	26
Magneto-elastic Energy (Stress-Induced Anisotropy).....	27
Chapter 2: Film Growth and Melt Design	30
Liquid Phase Epitaxy Film Growth	31
Melt Engineering	36
Chapter 3: Plasmon Resonances and Numerical Modeling.....	40
Plasmon Resonances as an Eigenvalue Problem	40
Electrostatic Model of Small Dielectric Objects	41

Numerical Modeling of Plasmon Resonance Enhancement of Magneto-Optical Effects in Garnets.....	43
Chapter 4: Characterization of the Garnet Films	52
Lattice Mismatch Measurement.....	52
Film Thickness Measurement	55
Transmission Measurements.....	56
Atomic Force Microscopy (AFM) Measurements.....	58
Optical Hysteresis Loop Measurements	59
Ferromagnetic Resonance (FMR) Measurements	64
Optical Domain Imaging.....	72
Development of Improved Faraday Rotation Measurement Techniques	72
Chapter 5: Development of Garnet Films Utilizing Plasmon Resonances for Faraday Rotation Enhancement	83
In-Plane Garnet Films with Embedded Gold Nanoparticles and Faraday Rotation Enhancement.....	83
Anisotropy Study of Out-of-Plane Garnet Films with Embedded Gold Nanoparticles	92
Development of Sub-Micron Thick Out-of-Plane Garnet Films Using LPE	101
Incorporation of Gold Nanoparticles on the Surface of LPE Grown Garnet Films and Faraday Rotation Enhancement	106
Conclusion and Future Work	123
Bibliography	126

List of Tables

Table 5.1: Cation ratios of the melt designs used to produce films with in-plane magnetization orientation with a film composition of $(\text{Bi, Pr, Y, Gd})_3(\text{Fe, Ga})_5\text{O}_{12}$	88
Table 5.2: Faraday rotation enhancement measurements for sample with in-plane magnetization orientation.....	92
Table 5.3: Cation ratios of the melt designs used to produce films with out-of-plane magnetization orientation with a film composition of $(\text{Bi, Gd, Lu})_3(\text{Fe, Ga})_5\text{O}_{12}$	92
Table 5.4: Growth conditions and film thickness values for the four samples grown from melt UMD302 with out-of-plane magnetization orientation.	94
Table 5.5: Faraday rotation enhancement measurements for sample with out-of-plane magnetization orientation measured with a red laser with wavelength of 633 nm.....	100
Table 5.6: Cation ratios of the melt designs used to produce sub-micron thick films with out-of-plane magnetization orientation with a film composition of $(\text{Bi, Gd, Lu})_3(\text{Fe, Ga})_5\text{O}_{12}$	103
Table 5.7: Summary of nanoparticle dimensions and separations as well as garnet film characterization for the twelve samples with different gold nanolayer thicknesses and annealing temperatures. R/H is the nanoparticle radius-to-height ratio, R/S is the nanoparticle radius-to-separation ratio, and H/F is the nanoparticle height to garnet film thickness ratio.	114
Table 5.8: Maximum Faraday rotation enhancement for each of the twelve samples and the wavelengths at which the maximum Faraday rotation enhancement has occurred. Each column in the table is for a different annealing temperature and each row in the table is for a different gold nanolayer thickness prior to annealing.....	121

List of Figures

Figure 1.1: Crystal structure of magnetic garnet, specifically Yttrium Iron Garnet (YIG) [GiGe58].	5
Figure 1.2: Sublattice magnetizations and total magnetization vs. temperature [STka11].	8
Figure 1.3: Schematic of the coordinate system used to describe the Faraday rotation. ..	12
Figure 1.4: The spherical coordinate system used to express the free energy density [Esch81].	23
Figure 2.1: (a) Schematic drawing of the liquid phase epitaxy growth system. (b) Image of the actual LPE growth system used at the Laboratory for Physical Sciences.	32
Figure 2.2: Pseudo-ternary PbO-Y ₂ O ₃ -Fe ₂ O ₃ phase equilibrium diagram showing four primary phase fields: hematite, magnetoplumbite, garnet, and orthoferrite [Blan72].	37
Figure 3.1: The dielectric region V^+ bounded by the surface S [FrMa03].	41
Figure 3.2: Schematic image of nanoparticles (a) placed on the surface of the garnet film and (b) embedded in the garnet film surface [Maye10].	45
Figure 3.3: The dependence of resonance wavelength on the height-to-radius ratio of a single hemispherical gold nanoparticle [Maye10].	48
Figure 3.4: The dependence of the resonance wavelength on the spacing between (a) two and (b) four adjacent gold hemispherical nanoparticles. The ratio of the height to the radius is denoted by h/t [Maye10].	49
Figure 3.5: Resonance wavelength as a function of particle geometry and spacing for two cylindrical gold nanoparticles [Maye10].	50
Figure 3.6: Distribution of the plasmon electric field in the midplane between two embedded cylindrical gold nanoparticles [Maye10].	50
Figure 4.1: Lattice mismatch between the epitaxially grown garnet film and the substrate: (a) no mismatch, (b) film under compression, (c) film is under tension.	53
Figure 4.2: Typical optical reflectance signal measured using the ellipsometer being analyzed in the FTG Film Thickness Module to calculate the film thickness.	56
Figure 4.3: (a) Transmittance measurements for adjacent regions of a SGGG (100)-oriented substrate with gold nanoparticles populated on the surface (solid) and without	

gold nanoparticles (dashed). (b) Absorption due to plasmon resonances in the gold nanoparticles calculated from the two curves in (a).	58
Figure 4.4: Typical atomic force microscopy measurement of the gold nanoparticles on a substrate surface. The vertical bar on the right is the scale for the height of the nanoparticles.	59
Figure 4.5: Optical hysteresis loop measurement experimental setup. The light from the laser (L) is linearly polarized by the polarizer (P) and then propagates through the sample (S) which is magnetized normal to the sample surface by the magnet (M). The transmitted beam then passed through the analyzer (A) which is another linear polarizer and finally reaches the detector (D) which is hooked up to the computer that measures the results.	60
Figure 4.6: Typical optical hysteresis loop measurements obtained for samples with out-of-plane magnetization.....	62
Figure 4.7: Schematic of the FMR system [STka11].	68
Figure 4.8: Input and Output Signals of the Lock-In Amplifier.	70
Figure 4.9: Typical signal measured in the FMR experiment. The x axis is the magnitude of the magnetic field in kOe [STka11].	71
Figure 4.10: Dependence of the ferromagnetic resonance field on the orientation of the sample [STka11].	71
Figure 4.11: Optical domain image obtained for a sample with out-of-plane magnetization orientation.....	72
Figure 4.12: Experimental setup for modified optical hysteresis loop and Faraday rotation measurements.....	73
Figure 4.13: Configurations of modified optical hysteresis loop setup for externally applied magnetic field (a) $\mathbf{H} +$ and (b) $\mathbf{H} -$	76
Figure 4.14: The detector signal for an arbitrarily elliptically polarized beam entering the rotating analyzer polarization detector [JAWo10].....	77
Figure 4.15: Schematic of the J. A. Woollam variable angle spectroscopic ellipsometer (VASE). The components of the system include: (1) monochromator, (2) fiber optic cable, (3) input unit with polarizer, (4) alignment detector, (5) sample stage, (6)	

goniometer base for automated angle control, (7) detector unit with rotating analyzer and solid state detectors, and (8) motor control box [JAWo10].	80
Figure 4.16: Actual experimental setup for ellipsometry-based Faraday rotation measurements. Additional components of the setup include: (1) mount for permanent magnets with slit in the center for light to pass through between the two permanent magnets, (2) gaussmeter probe, and (3) gaussmeter.	81
Figure 4.17: Permanent magnet holder with slit in between the two permanent magnets for the light to pass through the gap between the two magnets.	81
Figure 5.1: Schematic of substrates with gold deposited on them.	85
Figure 5.2: Atomic Force Microscopy image of gold nanoparticles formed on garnet substrate.	86
Figure 5.3: Transmission coefficients of the garnet substrates with and without gold nanoparticles [Tkac11].	87
Figure 5.4: X-ray Diffraction Peaks for the gold (111) reflection seen both before and after LPE film growth over substrates populated with gold nanoparticles.	88
Figure 5.5: The results of the transmission coefficient measurement for two adjacent points on either side of the boundary between garnet with and without embedded gold nanoparticles. The inset shows the difference between the two transmission measurements which reveals the absorption due to the plasmon resonances in gold nanoparticles [Tkac11].	89
Figure 5.6: Diagram of the checkerboard pattern of a sample with three sets of adjacent points at which measurements have been taken for comparison purposes.	90
Figure 5.7: Optical hysteresis loop comparison for two adjacent points on either side of the gold/no gold boundary.	91
Figure 5.8: Atomic Force Micrograph of gold nanoparticles formed on SGGG substrate by annealing at 900°C [Lang12].	93
Figure 5.9: Transmission coefficient measurements of SGGG substrates with gold (unannealed, and annealed at 700°C, 800°C, and 900°C) and without gold [Lang12].	94
Figure 5.10: Optical domain images for (BiGdLu) garnet film in regions (a) without and (b) with embedded gold nanoparticles [Lang12].	96

Figure 5.11: Ferromagnetic resonance frequency vs resonance field for (BiPrYGd) in-plane garnet sample regions with and without embedded gold nanoparticles [Lang12].	97
Figure 5.12: Ferromagnetic resonance spectra at 7 GHz for (BiGdLu) garnet showing response for regions with gold (dashed) and without gold (solid) embedded nanoparticles [Lang12].	98
Figure 5.13: Optical hysteresis loops for (a) 900°C annealed out-of-plane garnet with and without embedded gold nanoparticles and (b) unannealed out-of-plane garnet with and without embedded gold nanoparticles [Lang12].	98
Figure 5.14: (a) Optical hysteresis loop measurements for a sample with out-of-plane magnetization orientation. (b) An enlarged image of the upper saturation region of the loops shown in (a).	100
Figure 5.15: Along the left axis are the data points for the growth rate versus growth temperature (squares) and lattice mismatch versus growth temperature (diamonds), and along the right axis are the data points for the Faraday rotation per unit length versus growth temperature (triangles) for the samples produced from the new melt design. ...	104
Figure 5.16: Along the left axis are the data points for the Faraday rotation per unit length as a function of the growth rate (diamonds) and along the right axis are the data points for the bismuth concentration as a function of the growth rate (squares) for the new melt design.	105
Figure 5.17: Atomic Force Microscopy images of the nanoparticles formed on the surfaces of the samples annealed at 700°C. The thickness of the gold nanolayer prior to annealing is (a) 5nm, (b) 7.5nm, (c) 10nm, and (d) 15nm.	108
Figure 5.18: Ratios of the different dimensions and separations for the nanoparticles formed on the film surfaces of the samples annealed at 700°C. R/H is the nanoparticle radius-to-height ratio, R/S is the nanoparticle radius-to-separation ratio, and H/F is the nanoparticle height to sample film thickness ratio for each of the four samples annealed at 700°C.	109
Figure 5.19: Atomic Force Microscopy images of the nanoparticles formed on the surfaces of the samples annealed at 800°C. The thickness of the gold nanolayer prior to annealing is (a) 5nm, (b) 7.5nm, (c) 10nm, and (d) 15nm.	110
Figure 5.20: Ratios of the different dimensions and separations for the nanoparticles formed on the film surfaces of the samples annealed at 800°C. R/H is the nanoparticle radius-to-height ratio, R/S is the nanoparticle radius-to-separation ratio, and H/F is the	

nanoparticle height to sample film thickness ratio for each of the four samples annealed at 800°C.	111
Figure 5.21: Atomic Force Microscopy images of the nanoparticles formed on the surfaces of the samples annealed at 1000°C. The thickness of the gold nanolayer prior to annealing is (a) 5nm, (b) 7.5nm, (c) 10nm, and (d) 15nm.	112
Figure 5.22: Ratios of the different dimensions and separations for the nanoparticles formed on the film surfaces of the samples annealed at 1000°C. R/H is the nanoparticle radius-to-height ratio, R/S is the nanoparticle radius-to-separation ratio, and H/F is the nanoparticle height to sample film thickness ratio for each of the four samples annealed at 1000°C.	113
Figure 5.23: Transmission coefficient difference curves (extinction cross-sections) for the samples annealed at 700°C.	115
Figure 5.24: Transmission coefficient difference curves (extinction cross-sections) for the samples annealed at 800°C.	116
Figure 5.25: Transmission coefficient difference curves (extinction cross-sections) for the samples annealed at 1000°C.	116
Figure 5.26: Outline of gold deposition pattern on garnet film surface. Marks m1-m9 correspond to the measurement locations. The size of the samples is 11mm x 11mm [Lang13].	118
Figure 5.27: (a) Faraday rotation per unit length as a function of wavelength for one of the measurements for the sample that had 5nm of gold annealed at 800°C. (b) Faraday rotation enhancement as a function of wavelength for the same sample.	118
Figure 5.28: Faraday rotation enhancement plots for the four samples annealed at 700°C. The blue curves are the raw data curves and the green curves are the processed data curves after smoothing.	119
Figure 5.29: Faraday rotation enhancement plots for the four samples annealed at 800°C. The blue curves are the raw data curves and the green curves are the processed data curves after smoothing.	120
Figure 5.30: Faraday rotation enhancement plots for the four samples annealed at 1000°C. The blue curves are the raw data curves and the green curves are the processed data curves after smoothing.	120

List of Publications

- 1) I. Mayergoyz, P. McAvoy, **G. Lang**, D. Bowen, and C. Krafft, “Excitation and dephasing of circularly polarized plasmon modes in spherical nanoshells for application in all-optical magnetic recording”, *Journal of Applied Physics*, **105**, 07B904 (2009).
- 2) S. Tkachuk, V.J. Fratello, C. Krafft, **G. Lang**, and I.D. Mayergoyz, “Imaging Capabilities of Bismuth Iron Garnet Films With Low Growth-Induced Uniaxial Anisotropy”, *IEEE Transactions on Magnetics*, **45**(10), 4238 (2009).
- 3) I.D. Mayergoyz, **G. Lang**, L. Hung, S. Tkachuk, C. Krafft, and O. Rabin, “Plasmon resonance enhancement of magneto-optic effects in garnets”, *Journal of Applied Physics*, **107**, 09A925 (2010).
- 4) S. Y. Lee, L. Hung, **G. S. Lang**, J. E. Cornett, I. D. Mayergoyz, and O. Rabin, “Dispersion in the SERS Enhancement with Silver Nanocube Dimers”, *ACS Nano*, **4**(10), 5763-5772 (2010).
- 5) S. Tkachuk, **G. Lang**, C. Krafft, O. Rabin, and I. Mayergoyz, “Plasmon Resonance Enhancement of Faraday Rotation in Thin Garnet Films”, *Journal of Applied Physics*, **109**, 07B717 (2011).
- 6) C. Krafft, S. Tkachuk, **G. Lang**, D. Bowen, and I. D. Mayergoyz, “Magneto-Optic Indicator Films for Forensics”, *MRS Proceedings*, **1291**, published online only (2011).
- 7) **G. Lang**, D. Bowen, L. Hung, C. Krafft, and I. Mayergoyz, “Anisotropy study of garnet films grown over substrates populated with gold nanoparticles”, *Journal of Applied Physics*, **111**, 07A505 (2012).
- 8) L. Hung, **G. Lang**, P. McAvoy, C. Krafft, and I. Mayergoyz, “Circularly polarized plasmon modes in spheroidal nanoshells for applications to all-optical magnetic recording”, *Journal of Applied Physics*, **111**, 07A915 (2012).
- 9) **G. S. Lang**, D. Bowen, C. Krafft, and I. D. Mayergoyz, “Deposition of gold nanoparticles on liquid phase epitaxy grown garnet films and Faraday rotation enhancement”, *Journal of Applied Physics*, **113**, 17A929 (2013).

Introduction

Magneto-optic imaging devices and Faraday rotators are two devices that have been developed using rare-earth iron garnet thin films. Magneto-optic imagers help visualize the spatial distribution of a magnetic field and can be used for the visualization of magnetic tracks on audio and video tapes for forensics, and visualization of security features on banknotes. Faraday rotators are optical devices that rotate the plane of polarization of light due to the Faraday Effect. Faraday rotators are very useful in optical systems because they have non-reciprocal properties meaning that if the polarized beam transmitted through the device were to reflect back through the same device, the device would not undo the polarization change the beam underwent in its forward pass through the device. The rotation of the beam would instead be doubled due to the non-reciprocal property of such devices. There are many uses for this type of device in optical systems as standalone Faraday rotators or as components in optical isolators that prevent undesired back propagation of light from disrupting or damaging an optical system.

Bismuth-substituted iron garnet films are commonly used as magneto-optic imaging devices and Faraday rotators because of their large Faraday rotation and low absorption in the visible and near infrared regions. Faraday rotation is proportional to the thickness of the magneto-optic medium: the thicker the medium, the larger the Faraday rotation. There is a need for more compact devices without sacrificing performance. Developing thinner films with the same methods that previously exist would compromise on the amount of Faraday rotation the films exhibit. Enhancement of the Faraday rotation by other means that would allow for thinner films to be used while achieving the same or greater rotation of thicker films is of interest.

The motivation behind the research presented in this dissertation originates from the need to enhance the Faraday rotation of rare-earth iron garnet thin films. With the enhancement of the Faraday rotation, devices such as magneto-optic imagers could be produced with higher dynamic range, higher sensitivity, and even allow for imaging of small stray magnetic fields close to the surface of the specimen if the film thickness could be reduced.

It has been previously demonstrated that it is possible to enhance the Faraday rotation of iron garnet thin films by utilizing plasmon resonances in metallic nanoparticles [Maye10, Tkac11]. The research presented in this dissertation focuses on the development of thin iron garnet films utilizing plasmon resonances in metallic nanoparticles to enhance the Faraday rotation of the films. The excitation of plasmon resonances in the metallic nanoparticles induces strong localized electric fields that penetrate across the thickness of the garnet films and results in enhancement of magneto-optic effects in the garnet films. Optimization of the garnet film growth and nanoparticle assembly formation will allow the plasmon resonances of the metallic nanoparticles to induce electric fields that uniformly spread over the thickness of the films to maximize the potential enhancement of the Faraday rotation. This can be achieved through continued improvements of the growth process of sub-micron thick garnet films, better control of the nanoparticle arrays, and extensive development of characterization techniques. This dissertation will focus on the development of sub-micron thick garnet films that utilize plasmon resonances excited in metallic nanoparticles on the surface or embedded in the garnet films to enhance the magneto-optic effects of the films.

The structure of this dissertation is as follows. The first chapter will provide background information on the crystallographic structure of garnets and their properties. The second chapter will focus on the growth process and design of rare-earth iron garnet thin films. In the third chapter, a theoretical introduction to plasmon resonances and numerical modeling of plasmon resonances in metallic nanoparticles will be presented. A description of the techniques used to characterize the garnet films and nanoparticles assemblies will be presented in chapter four. The last chapter will provide a detailed account of the research efforts to develop sub-micron thick garnet films that exhibit strong enhancement of Faraday rotation due to the utilization of plasmon resonances in gold nanoparticles.

Chapter 1: Garnets and their Magnetic Properties

Garnets are complex structures that can be engineered to exhibit many desirable magnetic properties. The design of garnet films requires a strong understanding of their material properties. This chapter will begin with a discussion of the crystallographic structure of garnets followed by an explanation of the magnetization of garnets, which is the most important of their magnetic properties. Next, the origin of the magneto-optic effects of garnets will be described in detail. The chapter will conclude with a description of the magnetic interactions of garnets.

Crystal Structure

Naturally occurring garnets belong to a larger class of minerals called neosilicates which are generally non-magnetic and have the general formula $\{M^{2+}\}_3[M^{3+}]_2(Si^{4+})_3O_{12}$. The $\{M^{2+}\}$ site is usually occupied by divalent (Ca, Mg, Fe, Mn) cations and the $[M^{3+}]$ site by trivalent (Al, Fe, Cr) cations. Garnets have a cubic body centered unit cell containing 8 formula units resulting in 160 ions per cubic unit cell.

Synthetic growth of garnets has expanded the crystallographic structure to include chemicals with the general formula $\{c^{3+}\}_3[a^{3+}]_2(d^{3+})_3O_{12}$. Interesting magnetic properties arise in garnets when the appropriate elements are used which has led to the synthetic growth of rare-earth iron garnets. For these magnetic garnets, the dodecahedral {c} sites are occupied by rare-earth cations and/or by Y^{3+} , La^{3+} and Bi^{3+} , while the octahedral [a] and tetrahedral (d) sites are occupied by iron and/or iron substituents. The {c} site has 8 oxygen ions as its nearest neighbors that are located in the corners of a

dodecahedron and is referred to as the dodecahedral site. The [a] site forms an octahedron with 6 oxygen ions as nearest neighbors in its corners and is called the octahedral site. The (d) site is the tetrahedral site and consists of 4 oxygen ions as nearest neighbors forming a tetrahedron. The structure of yttrium iron garnet is depicted in Figure 1.1.

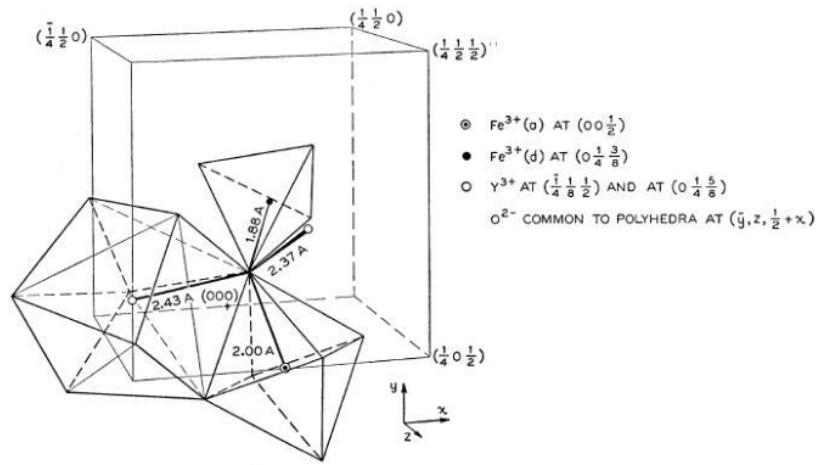


Figure 1.1: Crystal structure of magnetic garnet, specifically Yttrium Iron Garnet (YIG) [GiGe58].

The relative cation coordinates are fixed and have no positional degrees of freedom while the positions of the oxygen ions depend upon the ionic radii of the neighboring cations. This allows for variation in the size of the cations so that the three sites can be occupied by a variety of ions depending on what physical properties are desired. Various magnetic properties can be obtained by substituting specific sites with different rare-earth and diamagnetic elements.

Magnetization

The most important magnetic property is the magnetization, \vec{M} , which is the density of the magnetic dipole moments of the ions

$$\vec{M} = \frac{1}{V} \sum_i \vec{m}_i. \quad (1.1)$$

where \vec{m}_i are the magnetic dipole moments and V is the volume. The dipole moments of neighboring magnetic ions are coupled through the oxygen ions between them by means of an interaction called the super-exchange interaction where there is an overlap of the 2p-electrons of an oxygen ion with the electronic distribution of the magnetic ions. The interaction increases with an increase in the overlap. Therefore, the interaction is greatest for short distances between the magnetic ions and the oxygen ion, and for an oxygen ion which is nearest neighbor to two magnetic ions with angles near 180° .

Each oxygen ion in the crystallographic structure has two nearest neighbor cations on the dodecahedral sites and one nearest neighbor cation on the octahedral and tetrahedral sites, respectively. The sites are arranged in such a way that the strongest interaction occurs between the tetrahedral and octahedral sites. These two sites are coupled anti-ferromagnetically.

For iron garnets, there are 3 Fe^{3+} in the tetrahedral site and only 2 Fe^{3+} in the octahedral site per formula unit resulting in a net magnetic moment corresponding to that of one Fe^{3+} . The iron sublattices can be substituted with diamagnetic ions such as Ga^{3+} and Al^{3+} to alter the net magnetization. The net magnetization will increase with substitution of these diamagnetic ions on the octahedral sites and decrease with substitution on the tetrahedral sites. The site preferences for Ga^{3+} are 10% octahedral and 90% tetrahedral and the site preferences for Al^{3+} are 15% octahedral and 85% tetrahedral [Niel76].

The dodecahedral sites can be occupied by paramagnetic ions, in which case the respective magnetic sublattices have to be taken into account as well. In this case, there are two weaker anti-ferromagnetic interactions, one between the dodecahedral and octahedral sites and one between the dodecahedral and tetrahedral sites. The interaction between the dodecahedral ions and the tetrahedral ions is larger than the interaction between the dodecahedral ions and the octahedral ions [GeGi57].

The total magnetization is an algebraic sum of the magnetizations of the three sublattices with components denoted as $M_c(T)$, $M_a(T)$, and $M_d(T)$ for the contributions from the dodecahedral, octahedral, and tetrahedral sites, respectively. The temperature dependent saturation magnetization is therefore given by

$$M_s(T) = |\pm M_c(T) + M_a(T) - M_d(T)|. \quad (1.2)$$

The sublattice contributions are shown graphically in Figure 1.2. When the rare-earth moment is equal to the net moment of the octahedral and tetrahedral sublattices but of opposite sign, the total magnetization goes through zero at a point called the compensation temperature, T_{comp} . The Curie temperature, T_C , on the other hand, has a minimal dependence on the rare-earth contributions and is instead primarily controlled by the strong octahedral and tetrahedral iron interactions. The net magnetization can therefore be positive or negative at room temperature depending on the compensation temperature.

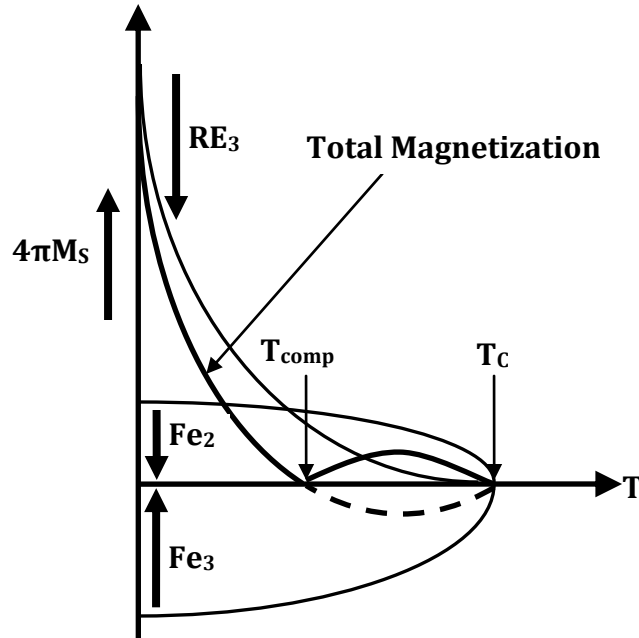


Figure 1.2: Sublattice magnetizations and total magnetization vs. temperature [STka11].

Macroscopic Origin of Magneto-Optical Effects

Rare-earth iron garnets are a good example of crystal systems that strongly exhibit magneto-optic effects due to their strong magnetic properties and optical transparency in the visible and near-infrared light ranges. At the macroscopic level, magneto-optic effects result from the interaction of an electromagnetic wave with a magnetization in a material or an external magnetic field.

Magneto-optic materials are gyrotropic in nature which means that they can discriminate between right- and left-circularly polarized light. As a result, when electromagnetic waves propagate through an active magneto-optic material, the elliptically polarized light is decomposed into right- and left-circularly polarized light and each component travels at a different speed through the medium. The difference in the

speed of the two components results in a rotation of the plane of polarization as the two components are superposed upon exiting the material.

The material properties of garnets can be described by a magnetic permeability tensor, μ_{ij} , and a dielectric permittivity tensor, ϵ_{ij} . Iron garnets are insulators so Maxwell's equations can be simplified using the properties of insulators that $\vec{J} = 0$ and $\rho = 0$. Since the ferromagnetic resonance absorption peak for these materials is located in the gigahertz range, the permeability tensor $\hat{\mu}$ can be considered equal to unity at frequencies corresponding to visible and near IR electromagnetic waves [LaLi84]. This forces all the magneto-optic effects to be incorporated into the permittivity tensor.

Maxwell's equations can consequently be reduced to the simple wave equation for \vec{E} as

$$\vec{\nabla} \times (\vec{\nabla} \times \vec{E}) = -\vec{\nabla} \times \frac{\partial \vec{B}}{\partial t} = -\mu_0 \frac{\partial}{\partial t} (\vec{\nabla} \times \vec{H}) = -\mu_0 \epsilon_0 \hat{\epsilon} \frac{\partial^2 \vec{E}}{\partial t^2}. \quad (1.3)$$

The wave propagation equation is then

$$\vec{\nabla}(\vec{\nabla} \cdot \vec{E}) - (\nabla^2) \vec{E} + \mu_0 \epsilon_0 \hat{\epsilon} \frac{\partial^2 \vec{E}}{\partial t^2} = 0. \quad (1.4)$$

Assuming a plane wave solution, $\vec{E} = E_0 e^{j(\omega t - \vec{k} \cdot \vec{r})} \hat{j}$, Eq. 1.4 can be simplified to

$$\vec{k}(\vec{k} \cdot \vec{E}) - (k^2) \vec{E} + k_0^2 \hat{\epsilon} \vec{E} = 0 \quad (1.5)$$

where $k_0 = \frac{2\pi}{\lambda}$, $\vec{r} = (x, y, z)$ is the position vector, \vec{k} is the propagation vector of light, ω is the angular frequency, λ is the wavelength of free space, and $E_0\hat{j}$ is the amplitude vector of the light wave.

The permittivity tensor, $\hat{\epsilon}$, seen in Eq. 1.5 characterizes the optical properties of garnets and combines the different optical effects as follows:

$$\hat{\epsilon} = \hat{\epsilon}^{\text{iso}} + \Delta\hat{\epsilon}^{\text{S}} + \Delta\hat{\epsilon}^{\text{G}} + \Delta\hat{\epsilon}(\vec{M}) \quad (1.6)$$

where $\hat{\epsilon}^{\text{iso}} = N_0^2\delta_{ij}$ is the isotropic component with $N_0 = n_0 - j\frac{\alpha_0}{2k_0}$, n_0 is the isotropic index of refraction, and α_0 is the isotropic absorption coefficient. $\Delta\hat{\epsilon}^{\text{S}}$ is the stress induced optical anisotropy, $\Delta\hat{\epsilon}^{\text{G}}$ is the growth induced optical anisotropy, and $\Delta\hat{\epsilon}(\vec{M})$ is the magnetization dependent component of the permittivity tensor.

Assuming that the medium is an unbounded isotropic dielectric material, the stress and growth induced optical anisotropies can be neglected when considering small perturbations [Nist06]. Therefore, $\hat{\epsilon}$ can be simplified to

$$\hat{\epsilon} = \hat{\epsilon}^{\text{iso}} + \Delta\hat{\epsilon}(\vec{M}) \quad (1.7)$$

where the magnetization dependent component is much smaller than the isotropic component.

If a magnetic field of sufficient strength is applied to an iron garnet, the magnetic moments of the magnetic domains are aligned parallel to the applied field and the magnetization is saturated. The magneto-optic properties therefore depend on the

magnetization, \vec{M} , rather than the magnetic field [Pers67]. For all practical cases, the magnetization dependent component can be written as a power series:

$$\Delta\varepsilon_{ij}(\vec{M}) = \sum_{k=1}^3 K_{ijk}M_k + \sum_{k=1}^3 \sum_{l=1}^3 G_{ijkl}M_kM_l + \dots \quad (1.8)$$

where K_{ijk} and G_{ijkl} are the components of the linear and quadratic magneto-optical tensor, respectively [Wett76]. The dependence of ε_{ij} on \vec{M} is governed by the Onsager relation

$$\Delta\varepsilon_{ij}(\vec{M}) = \Delta\varepsilon_{ji}(-\vec{M}) \quad (1.9)$$

that helps further simplify the magnetization dependent component of the permittivity tensor [LaLi84].

Taking symmetry into consideration, the magnetization dependent component of the permittivity tensor can be simplified by determining which of its components are non-zero. For a cubic symmetry, for example,

$$K_{123} = K_{231} = K_{312} = -K_{213} = -K_{321} = -K_{132} = K, \quad (1.10)$$

and all other $K_{ijk} = 0$ [Wett76]. The quadratic components, G_{ijkl} , give rise to the reciprocal effect called the Cotton-Mouton effect which is usually much smaller than the linear effects [Nist06]. Therefore, the quadratic tensor will be neglected. The magnetization dependent part of the permittivity tensor for a homogeneously magnetized cubic crystal is

$$\Delta\hat{\epsilon}(\vec{M}) = \begin{pmatrix} 0 & KM_3 & -KM_2 \\ -KM_3 & 0 & KM_1 \\ KM_2 & -KM_1 & 0 \end{pmatrix} \quad (1.11)$$

which is invariant against rotations of the coordinate system, and the isotropic part of the permittivity tensor is

$$\hat{\epsilon}^{iso} = \begin{pmatrix} N_0^2 & 0 & 0 \\ 0 & N_0^2 & 0 \\ 0 & 0 & N_0^2 \end{pmatrix}. \quad (1.12)$$

The overall permittivity tensor is therefore

$$\hat{\epsilon} = \begin{pmatrix} N_0^2 & KM_3 & -KM_2 \\ -KM_3 & N_0^2 & KM_1 \\ KM_2 & -KM_1 & N_0^2 \end{pmatrix} = \begin{pmatrix} \epsilon_{11} & \epsilon_{12} & -\epsilon_{31} \\ -\epsilon_{12} & \epsilon_{22} & \epsilon_{23} \\ \epsilon_{31} & -\epsilon_{23} & \epsilon_{33} \end{pmatrix}. \quad (1.13)$$

The Faraday rotation can be derived using the permittivity tensor that describes the gyrotropic media. The off-diagonal terms of the permittivity tensor lead to non-reciprocal mode conversion and non-reciprocal phase shifts [Nist06].

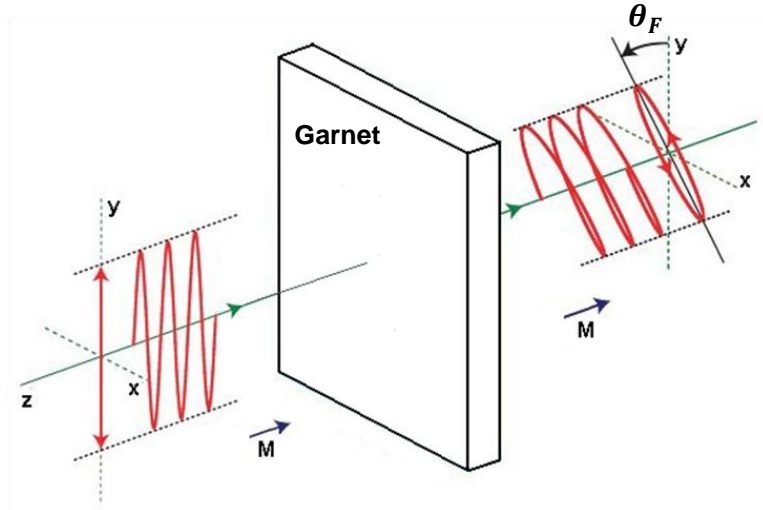


Figure 1.3: Schematic of the coordinate system used to describe the Faraday rotation.

To demonstrate the origin of the magneto-optic effects from the permittivity tensor, consider a plane wave $\vec{E} = E_0 e^{j(\omega t - kz)} \hat{j}$ propagating perpendicular to the film plane with wave vector $\vec{k} = (0, 0, k)$ (see Figure 1.3). Assuming a more general magnetization parallel to the xz-plane with $\vec{M} = M_s(\sin \theta, 0, \cos \theta)$, Eq. 1.13 becomes

$$\hat{\epsilon} = \begin{pmatrix} N_0^2 & KM_s \cos \theta & 0 \\ -KM_s \cos \theta & N_0^2 & KM_s \sin \theta \\ 0 & -KM_s \sin \theta & N_0^2 \end{pmatrix}. \quad (1.14)$$

Plugging Eq. 1.14 into the wave equation, Eq. 1.5, two solutions are obtained for k. This can be formulated as an eigenvalue problem. The eigenvalues are obtained so that there will be non-trivial solutions for the electric field which is when the determinant of the coefficients vanishes:

$$\det |k^2 \delta_{ij} - k_i k_j - k_0^2 \epsilon_{ij}(\omega, \vec{M})| = 0. \quad (1.15)$$

For simplicity, it is assumed that the wave vector of the propagating plane wave is $\vec{k} = (0, 0, k)$, which yields

$$\begin{vmatrix} \epsilon_{11} - (k/k_0)^2 & \epsilon_{12} & -\epsilon_{31} \\ -\epsilon_{12} & \epsilon_{22} - (k/k_0)^2 & \epsilon_{23} \\ \epsilon_{31} & -\epsilon_{23} & \epsilon_{33} \end{vmatrix} = 0. \quad (1.16)$$

Solving Eq. 1.16 for k, the two solutions for k are found to be

$$k_{1,2} = k_0 \sqrt{\frac{\epsilon_{33} \epsilon_{22} + \epsilon_{33} \epsilon_{11} + \epsilon_{23}^2 \pm \sqrt{\epsilon_{33}^2 \epsilon_{22}^2 - 2\epsilon_{33}^2 \epsilon_{22} \epsilon_{11} + 2\epsilon_{23}^2 \epsilon_{22} \epsilon_{33} + \epsilon_{11}^2 \epsilon_{33}^2 - 2\epsilon_{23}^2 \epsilon_{11} \epsilon_{33} + \epsilon_{23}^4 - 4\epsilon_{33}^2 \epsilon_{12}^2}}{2\epsilon_{33}}}}. \quad (1.17)$$

For the magnetization, $\vec{M} = M_s(\sin \theta, 0, \cos \theta)$, Eq. 1.17 becomes

$$k_{1,2} = k_0 \sqrt{N_0^2 + \frac{(KM_s)^2 \sin^2 \theta}{2N_0^2} \pm j(KM_s) \sqrt{\cos^2 \theta - \frac{(KM_s)^2 \sin^4 \theta}{4N_0^4}}} = k_0 N_{1,2}. \quad (1.18)$$

For the wave equation shown in Eq. 1.5, the respective eigenmodes are

$$\vec{E}^{(1)} = E_0 \begin{pmatrix} 1 \\ \frac{(N_0^2 - N_1^2)}{KM_s \cos \theta} \\ \frac{(N_0^2 - N_1^2) \tan \theta}{N_0^2} \end{pmatrix} e^{j(\omega t - k_1 z)} = E_0 \begin{pmatrix} E_x^{(1)} \\ E_y^{(1)} \\ E_z^{(1)} \end{pmatrix} e^{j(\omega t - k_1 z)} \quad (1.19)$$

$$\vec{E}^{(2)} = E_0 \begin{pmatrix} \frac{KM_s \cos \theta}{(N_2^2 - N_0^2)} \\ 1 \\ \frac{KM_s \sin \theta}{N_0^2} \end{pmatrix} e^{j(\omega t - k_2 z)} = E_0 \begin{pmatrix} E_x^{(2)} \\ E_y^{(2)} \\ E_z^{(2)} \end{pmatrix} e^{j(\omega t - k_2 z)}.$$

The incoming wave is usually linearly polarized and is analyzed at the output by a polarizer referred to as an analyzer. For the case where \vec{k} is along the z-direction, the eigenmodes can be used to express the incoming wave that is linearly polarized under an angle β at $z=0$ as the linear combination:

$$\vec{E}_{in} = E_0 (A\vec{E}^{(1)} + B\vec{E}^{(2)}) e^{j\omega t} \quad (1.20)$$

where

$$A = \frac{\cos \beta - \sin \beta \cdot E_x^{(2)}}{1 - E_y^{(1)} E_x^{(2)}}, B = \frac{\sin \beta - \cos \beta \cdot E_y^{(1)}}{1 - E_y^{(1)} E_x^{(2)}}. \quad (1.21)$$

After the wave is transmitted through a magneto-optic medium of thickness d , the output at $z=d$ is

$$\vec{E}_{out} = E_0 \left(A \vec{E}^{(1)} e^{j(\omega t - k_1 d)} + B \vec{E}^{(2)} e^{j(\omega t - k_2 d)} \right). \quad (1.22)$$

In order to obtain useful analytical solutions, some approximations are made. For a wide range of angles, usually $0 \leq \theta \leq 45^\circ$, the approximation $|KM_s| \sin^2 \theta \ll 2N_0^2 |\cos \theta|$ can be made [Nist06]. The terms with $\sin^2 \theta$ and $\sin^4 \theta$ can therefore be neglected and the solutions for k is simplified to

$$k_{1,2} = k_0 N_0 \pm j k_0 \frac{(KM_s) \bar{N}_0}{2N_0^2} \cos \theta. \quad (1.23)$$

The two propagating modes have different indices of refraction as shown in Eq. 1.23. Equation 1.23 can therefore be further simplified to

$$k_{1,2} = k_0 n^\pm - j \frac{\alpha^\pm}{2} \quad (1.24)$$

where α is the absorption coefficient defined as

$$\alpha^\pm = k_0 \left(\frac{\alpha_0}{k_0} \mp \frac{n_0 K' M_s - \frac{\alpha_0}{2k_0} K'' M_s}{|N_0|^2} \cos \theta \right) \quad (1.25)$$

and n is the index of refraction defined as

$$n^\pm = n_0 \mp \frac{n_0 K'' M_s + \frac{\alpha_0}{2k_0} K' M_s}{2|N_0|^2} \cos \theta. \quad (1.26)$$

The real part of K is denoted K' and the imaginary part of K is denoted K'' . Using Eq. 1.24, the modes corresponding to the right- (\vec{E}^+) and left-circularly (\vec{E}^-) polarized plane waves can be expressed as

$$\vec{E}^+ = E_0 \begin{pmatrix} 1 \\ j \\ 0 \end{pmatrix} e^{j(\omega t - k_0 n^+ z) - \alpha^+ z/2}$$

$$\vec{E}^- = E_0 \begin{pmatrix} j \\ 1 \\ \frac{KM_s}{N_0^2} \sin \theta \end{pmatrix} e^{j(\omega t - k_0 n^- z) - \alpha^- z/2}. \quad (1.27)$$

The right- and left-circularly polarized plane waves with small longitudinal components, propagate along the z -direction with different indices of refraction

$$N^\pm = n^\pm - j \frac{\alpha^\pm}{2k_0} \quad (1.28)$$

The propagating wave can be represented as the superposition of the right- and left-circularly polarized components with the polarization plane at an angle β with respect to the x -axis:

$$\vec{E} = (\cos \beta - j \sin \beta) \vec{E}^+ + (\sin \beta - j \cos \beta) \vec{E}^-. \quad (1.29)$$

If there is no difference in the absorption coefficient for the two eigenmodes,

$$\begin{aligned}\vec{E}_{out} &= \frac{1}{2}(\cos \beta - j \sin \beta)\vec{E}^+(d) + \frac{1}{2}(\sin \beta - j \cos \beta)\vec{E}^-(d) \\ &= E_0 e^{j(\omega t - k_0 n_0 d)} e^{-\frac{\alpha_0}{2}d} \begin{pmatrix} \cos\left(\beta + k_0 \frac{n^+ - n^-}{2} d\right) \\ \sin\left(\beta + k_0 \frac{n^+ - n^-}{2} d\right) \end{pmatrix}\end{aligned}\quad (1.30)$$

which describes a linearly polarized wave with the polarization plane rotated by an angle

$$\theta_F = k_0 \frac{n^+ - n^-}{2} d = \frac{\pi}{\lambda} \text{Re}(n^+ - n^-) \cos \theta \cdot d \equiv \theta_{max} \cos \theta \cdot d \quad (1.31)$$

known as the magnetic circular birefringence (MCB) or Faraday rotation.

In general, the two eigenmodes have different absorption coefficients so even if the incident wave is linearly polarized, the emerging wave is elliptically polarized with the main axis rotated by the Faraday rotation angle and ellipticity related to:

$$\phi = \frac{\alpha^+ - \alpha^-}{4} d = \frac{\pi}{\lambda} \text{Im}(n^+ - n^-) \cos \theta \cdot d \equiv \phi_{max} \cos \theta \cdot d. \quad (1.32)$$

This effect is called the magnetic circular dichroism (MCD). The angle Ψ is the Faraday ellipticity and can be calculated from the angle ϕ as

$$\tan \Psi = \tanh(\phi_{max} \cos \theta \cdot d). \quad (1.33)$$

In summary, a linearly polarized wave incident on the gyrotropic medium is split under the influence of magnetization into two eigenmodes, one right-circularly polarized and the other left-circularly polarized. Due to the different refractive indices, the right- and left-circularly polarized waves have different propagation velocities [Wett76]. This causes a rotation of the polarization vector.

For iron garnets, the Faraday rotation is a superposition of the sublattice contributions with temperature and wavelength dependence according to:

$$\theta_F(\lambda, T) = A(\lambda)M_a(T) + D(\lambda)M_d(T) + C(\lambda)M_c(T) \quad (1.34)$$

where $A(\lambda)$, $D(\lambda)$ and $C(\lambda)$ are the temperature independent magneto-optic coefficients for the octahedral, tetrahedral and dodecahedral sites, respectively, and $M_a(T)$, $M_d(T)$ and $M_c(T)$ are the sublattice magnetizations defined in the previous section [Cros68].

Microscopic Origin of Magneto-Optical Effects

The primary goal of the research presented in this dissertation has been to enhance the Faraday rotation of iron garnet thin films. Therefore, the microscopic origin of magneto-optic effects is important to understand in order to engineer and design garnets with particular desired properties. It is important to know what causes the magneto-optic effects and how to manipulate those effects. This section focuses on the microscopic origin of these effects.

Spin-Orbit Interaction

The dominant contribution to the magneto-optic effects is from the spin-orbit splitting of the excited states. While the exchange splitting is much larger than the spin-orbit splitting, the exchange interaction only acts on the spin levels, not on the orbitals, and therefore cannot give rise to magneto-optic effects [Wett76]. The weaker spin-orbit interaction allows the orbitals to sense the polarization of the right- and left-circularly polarized components of the light, resulting in the magneto-optic effects. The spin-orbit interaction is described by the following Hamiltonian:

$$\hat{H}_{so} = \frac{\hbar}{4m^2c^2} (\nabla V \times \hat{p}) \cdot \hat{\sigma} \quad (1.35)$$

where \hbar is Planck's constant, m is the mass of a free electron, c is the speed of light, \hat{p} is the momentum operator, V is the Coulomb potential of the atomic core, and $\hat{\sigma}$ is the vector of Pauli spin matrices.

The spin-orbit interaction is the dipole interaction between an electron's spin and the magnetic field created by the electron's own orbital motion. This interaction creates orbital magnetism and couples the spin system to the lattice, allowing energy and angular momentum exchange and giving rise to magneto-crystalline anisotropy. It is fully responsible for the overall magnetic anisotropy since the exchange interaction itself is isotropic and only the coupling of the spin to the lattice can "lock-in" a macroscopic magnetization [StSi06].

Light-Matter Interactions

When light travels through a magneto-optic medium, it interacts with the particles within the medium. As the light wave approaches a particle of matter, energy is absorbed and sets electrons within the atom into vibrational motion. If the frequency of the light wave does not match the resonant frequency of the vibration of the electron, energy is emitted in the form of a new light wave with the same frequency as the original wave. This cycle of absorption and emission continues as the energy is transported from particle to particle through the bulk of the medium.

Every photon travels between the interatomic void at the speed of light, c , but there is a time delay involved due to the interactions with the particles, lowering the net speed of transport from one end of the medium to the other. The index of refraction can

therefore be defined as the ratio of the speed of light in a vacuum, c , to the speed the light travels through the medium, v_{matter} :

$$n = \frac{c}{v_{matter}}. \quad (1.36)$$

Linearly polarized light is the superposition of right- and left-circularly polarized light. Right- and left-circularly polarized light travel at different speeds due to selection rules that govern energy transitions for absorption and emission. The difference in the speeds causes a phase shift between the two circularly polarized components upon exiting the medium. The superposition of the two components at the output results in linearly polarized light at a different angle from the incident light. The angle by which the linearly polarized light has rotated as it propagates through the medium is the Faraday rotation angle.

Connection between Microscopic Phenomena and Macroscopic Values

The macroscopic origin of the magneto-optic effects discussed in the previous section can be decomposed into microscopic values.

The macroscopic polarizability tensor of an ion is defined as

$$\alpha_{ij} = -\frac{1}{\hbar} \sum_{ab} p_a \left\{ \frac{d_{ab}^i d_{ba}^j}{\omega_{ab} + \omega - i\Gamma_{ab}} + \frac{d_{ab}^j d_{ba}^i}{\omega_{ab} - \omega + i\Gamma_{ab}} \right\} \quad (1.37)$$

where a is the ground state of the ion, b is the excited state of the ion, p_a is the probability of an electron being located at the ground state (energy level E_a), d_{ab}^i is the matrix element of the i^{th} ($i=x,y,z$) component of the dipole moment connecting states a and b , $\hbar\omega_{ab} = E_a - E_b$, and Γ_{ab} is the half-width of the spectral band of the a to b

transition. The off-diagonal elements of the polarizability tensor are defined by the difference between contributions of right- and left-circularly polarized transitions [Zvez97].

The material's dielectric permittivity tensor is defined as

$$\varepsilon_{ij} = 4\pi N \left(\frac{n^2 + 2}{3} \right)^2 \alpha_{ij} \quad (1.38)$$

where N is the concentration of magnetic ions, n is the average refractive index of the material, and L is the Lorentz-Lorenz factor defined as $L = \left(\frac{n^2 + 2}{3} \right)^2$. The off-diagonal components of the permittivity tensor govern the magneto-optic effects. In a magnetic field and in magnetically ordered materials, the balance between the total contributions of the right- and left-circularly polarized light to the permittivity is broken which results in a rotation of the plane of polarization of light [Zvez97].

The Faraday rotation is defined as

$$\theta_F = \frac{\pi N e^2 L}{m c n} \sum_{ab} p_a \left\{ \frac{f_{ab}^+ - f_{ab}^-}{\omega_{ab}} \varphi(\omega, \omega_{ab}) \right\} \quad (1.39)$$

where the oscillator strengths for the right- and left-circularly polarized light is

$$f^\pm = (\hbar e^2)^{-1} m \omega_{ab} |d_{ab}^x \pm i d_{ab}^y|^2 = (\hbar e^2)^{-1} m \omega_{ab} |d_{ab}^\pm|^2 \quad (1.40)$$

and $\varphi(\omega, \omega_{ab})$ is the shape of the dispersion curve of the Faraday Effect for the a to b transition characterized by

$$\varphi(\omega, \omega_{ab}) = \frac{\omega_{ab}\omega(\omega_{ab}^2 - \omega^2 - \Gamma_{ab}^2)}{(\omega_{ab}^2 - \omega^2 + \Gamma_{ab}^2)^2 + 4\omega^2\Gamma_{ab}^2}. \quad (1.41)$$

The difference between the polarizabilities of the quantum system for right- and left-circularly polarized waves is due to the difference between the frequencies of the right- and left- transitions (due to the Zeeman effect and selection rules), the differences between their oscillator strengths f^\pm (probability of energy level transitions), and the differences between the populations of their initial ground state levels p_a . The difference in the polarizabilities results in different amounts of transitions for the right- and left-circularly polarized components of light which in turn results in different speeds of propagation for the two components. The difference in the speeds for the two components is the cause of the magneto-optic effects.

Magnetic Interactions

The static magnetic properties of garnets will be discussed in this section. There are five main magnetic interactions that specify the magnetic characteristics of garnets. It will be shown that these magnetic properties are influenced by the structural characteristics of the films and will include both magnetic and structural parameters. The garnet film can be thought of as a network of ions having spin and magnetic moments that undergo five different interactions, each resulting in an energy [Esch81]:

1. Interaction with each other: Exchange Energy
2. Interaction with the film shape: Demagnetizing Energy
3. Interaction with any local magnetic field: Zeeman Energy
4. Interaction with film orientation: Anisotropy Energy
5. Interaction with local stress: Magneto-elastic Energy.

The coordinate system used to express the free energy density is shown in Figure 1.4:

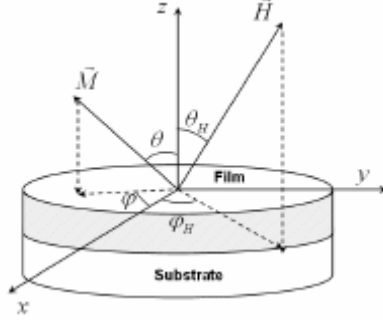


Figure 1.4: The spherical coordinate system used to express the free energy density [Esch81].

Exchange Energy

The exchange energy is due to the quantum mechanical effect of the overlapping of the electron wave functions and is responsible for the coupling of the spins of the magnetic ions. The exchange energy can be express by

$$E_{ex} = -2 \sum_{i \neq j} J_{ij} \vec{S}_i \cdot \vec{S}_j \quad (1.42)$$

where J_{ij} is the exchange integral, also known as the overlap integral, of the electron wave functions of the ions at sites i and j , and \vec{S}_i and \vec{S}_j are the spin operators. The exchange integral is a measure of the spatial overlap of two interacting wave functions ϕ_i and ϕ_j

$$J_{ij} = \int \phi_i^* \phi_j d\tau = \langle \phi_i | \phi_j \rangle. \quad (1.43)$$

If the exchange integral is positive, the interaction is ferromagnetic, and if the exchange integral is negative, the interaction is anti-ferromagnetic. The exchange integral is generally unknown since it is referring to electrons that are constantly moving.

Therefore, a macroscopic treatment of the exchange energy is formulated. Approximations have been made using the molecular field theory that allows for a simple empirical representation of the exchange energy [MaSI79]:

$$E_{ex} = \sum_{l,m,n=1}^3 A_{mn} \frac{\partial \alpha_l}{\partial x_m} \frac{\partial \alpha_l}{\partial x_n} \quad (1.44)$$

where α_i are the direction cosines of the magnetization vector \vec{M} , and A_{mn} is the exchange tensor. The direction cosines can be expressed in terms of the polar coordinate system shown in Figure 1.4 as:

$$\begin{aligned} \alpha_1 &= \sin \theta \cos \phi \\ \alpha_2 &= \sin \theta \sin \phi \\ \alpha_3 &= \cos \theta. \end{aligned} \quad (1.45)$$

In a lattice, the exchange tensor, A_{mn} , is proportional to the unit tensor $A = s^2 a^2 J_{ex} z$ called the exchange stiffness where a is the lattice spacing. Since the electrons are identical, Eq. 1.44 is simplified for a cubic array as

$$E_{ex} = A \sum_{l,m=1}^3 \left(\frac{\partial \alpha_l}{\partial x_m} \right)^2 = A [(\nabla \alpha_1)^2 + (\nabla \alpha_2)^2 + (\nabla \alpha_3)^2] \cong A \left(\frac{\nabla M}{M} \right)^2. \quad (1.46)$$

Demagnetizing Energy

If an object of finite size is magnetized, free magnetic poles are induced on both its ends, giving rise to a magnetic field in a direction opposite that of the magnetization. This field is referred to as the demagnetizing field and is given by

$$\vec{H}_{dem} = -N\vec{M} \quad (1.47)$$

where N is the demagnetizing factor. In general, for a Cartesian coordinate system,

$$N_x + N_y + N_z = 1. \quad (1.48)$$

The demagnetization energy can be expressed as

$$\begin{aligned} E_{dem} &= \frac{1}{2} \vec{M} \vec{H}_{dem} = \frac{1}{2} \vec{M} \hat{N} \vec{M} \quad (1.49) \\ &= \frac{1}{2} [M_x \quad M_y \quad M_z] \begin{bmatrix} N_x & 0 & 0 \\ 0 & N_y & 0 \\ 0 & 0 & N_z \end{bmatrix} \begin{bmatrix} M_x \\ M_y \\ M_z \end{bmatrix} \\ &= \frac{1}{2} [M_x N_x M_x + M_y N_y M_y + M_z N_z M_z]. \end{aligned}$$

More specifically, iron garnet thin films can be treated like a sheet on the xy-plane, where $N_z = 1$ and $N_x = N_y = 0$. The demagnetizing field for garnets can therefore be reduced from Eq. 1.47 to

$$H_{dem} = -N_z M_z = -N_z M \cos \theta = -M \cos \theta \quad (1.50)$$

and the demagnetization energy can be reduced from Eq. 1.49 to

$$E_{dem} = \frac{1}{2} M^2 \cos^2 \theta \quad (1.51)$$

The position of equilibrium is at $\theta = \frac{\pi}{2}$ which means that the magnetization lies in the plane of the thin film where θ is the angle between the magnetization vector and the normal of the film (see Figure 1.4).

Zeeman Energy

The Zeeman energy is the energy due to the interaction between the magnetization and an external applied field. When an external field is applied to the crystal, it is favorable for the magnetization to align parallel to the applied field. This interaction can be described by the Zeeman energy as

$$E_{Zeeman} = -\vec{M} \cdot \vec{H}. \quad (1.52)$$

Anisotropy Energy

The anisotropy energy refers to the energy related to the orientation of the magnetization with respect to some internal structure of the film [Esch81]. There are three components of the anisotropy energy: cubic, growth, and stress.

Cubic Anisotropy

The cubic anisotropy, also known as crystalline anisotropy, is based on the interaction between the electron spin and the orbital angular momentum. The energy related to this interaction is

$$E_{cub} = K_1 s + K_2 p + K_3 s^2 + K_4 s p \dots \quad (1.53)$$

where $s = \alpha_1^2 \alpha_2^2 + \alpha_2^2 \alpha_3^2 + \alpha_1^2 \alpha_3^2$ and $p = \alpha_1^2 \alpha_2^2 \alpha_3^2$. K_i are the anisotropy constants and α_i are the direction cosines of the magnetization vector. Some garnets will have rare-earths such as Pr that make $K_1 > 0$ and K_2 significant, but for most garnets $K_2 \approx 0$ and $K_1 < 0$ so the easy axes will be aligned with the $\langle 111 \rangle$ directions [Nist06]. The energy can therefore be simplified in this case to:

$$E_{cub} \approx K_1(\alpha_1^2\alpha_2^2 + \alpha_2^2\alpha_3^2 + \alpha_1^2\alpha_3^2). \quad (1.54)$$

Growth Anisotropy

The primary mechanism producing growth anisotropy in the films is the preferential distribution of rare-earth ions on certain lattice sites depending on the growth orientation, the deposition parameters, and the identity of the ions [Esch81]. Generally, for garnets which are cubic, the growth anisotropy dominates the anisotropy energy density term [Esch81]. This does, however, depend on the composition of the rare-earths in the garnet film. The growth anisotropy energy for the general case is

$$E_{gro} = A(\alpha_1^2\beta_1^2 + \alpha_2^2\beta_2^2 + \alpha_3^2\beta_3^2) \quad (1.55)$$

$$+ B(\alpha_1\alpha_2\beta_1\beta_2 + \alpha_2\alpha_3\beta_2\beta_3 + \alpha_3\alpha_1\beta_3\beta_1)$$

where β_i are the direction cosines of the film growth direction. The growth anisotropy energy for films oriented perpendicular to [100], for example, is

$$E_{gro} = A\alpha_1^2. \quad (1.56)$$

Magneto-elastic Energy (Stress-Induced Anisotropy)

Stress-induced anisotropy is due to a stress in a film caused by a mismatch in the lattice spacing of the substrate (a_0^s) to that of the film (a_0^f): $\Delta a_0 = a_0^s - a_0^f$. The energy related to the stress-induced anisotropy comes from magnetostriction, a phenomenon wherein a ferromagnetic material changes shape during the process of magnetization.

The deformation, $\frac{\delta l}{l}$, due to magnetostriction is very small (on the order of $10^{-5} - 10^{-6}$) [Esch81]. The strain due to magnetostriction increases when the magnetic field

intensity increases and will eventually reach a saturation value λ . The deformation is a result of two processes that occur at the atomic level. The first process is the spontaneous deformation of the crystal lattice inside each domain in the direction of domain magnetization. The second process is the rotation of the strain axis with a rotation of the domain magnetization. These two processes result in a deformation of the specimen as a whole [Chik78].

The energy due to the magnetostriction phenomenon for a (100)-oriented film is

$$E_{stress} = -\frac{3}{2}\lambda_{100}\sigma(\alpha_1^2\gamma_1^2 + \alpha_2^2\gamma_2^2 + \alpha_3^2\gamma_3^2) \quad (1.57)$$

where α_i are the direction cosines of domain magnetization, γ_i are the direction cosines of the tension which is normal to the film plane, and λ_{100} is the magnetostrictive coefficient of the film and represents the strain that is induced in a crystal when magnetization is saturated in the (100)-direction [Esch81]. For a (100)-oriented substrate, $\gamma_3 = 1, \gamma_1 = \gamma_2 = 0$. The local stress in the film is $\sigma = \frac{E}{1-\nu} \frac{\Delta a_0}{a_0}$ which relates the stress to the mismatch in lattice spacing Δa_0 where E is the Young's modulus and ν is Poisson's ratio.

The magnetostrictive (elongation) coefficient is defined as:

$$\lambda = \frac{\delta l}{l} = \frac{-B_1}{c_{11} - c_{12}} \left(\alpha_1^2 \beta_1^2 + \alpha_2^2 \beta_2^2 + \alpha_3^2 \beta_3^2 - \frac{1}{3} \right) \quad (1.58)$$

$$- \frac{B_2}{c_{44}} (\alpha_1 \alpha_2 \beta_1 \beta_2 + \alpha_2 \alpha_3 \beta_2 \beta_3 + \alpha_3 \alpha_1 \beta_3 \beta_1)$$

where β_i are the direction cosines of the observed elongation, and c_{11} , c_{12} , *and* c_{44} are the elastic moduli [Chik78]. Equation 1.58 can be inserted back into Eq. 1.57 to calculate the magneto-elastic energy.

Chapter 2: Film Growth and Melt Design

Many of the properties of garnet films are dependent on the growth conditions and melt composition. For this reason, the origins of the different properties have been discussed in the previous chapter prior to the discussion of how the garnet films are grown. This chapter will focus on the growth process and melt design of garnet films.

The growth process of magnetic garnet thin films is a complicated procedure with many delicate steps. The major steps include the design of the melt, the preparation of non-magnetic garnet substrates, and the deposition of magnetic garnet films on the substrates.

To prepare the substrates, non-magnetic garnet crystal boules are sliced into circular wafers and polished. The polished wafers are later diced into small substrates that must be non-magnetic, single crystal, rigid, flat and have smooth surfaces. It is important that there are no defects in the substrates and that the lattice spacing (a_0^s) and crystallographic orientation match that of the desired film to be grown. The typical substrate used in garnet growth is gadolinium gallium garnet (GGG) where Ga is substituted for Fe which makes the substrate non-magnetic with the following chemical formula: $\{\text{Gd}^{3+}\}_3[\text{Ga}^{3+}]_2(\text{Ga}^{3+})_3\text{O}_{12}$. The GGG substrate has a lattice constant of $a_0^s = 1.2384\text{nm}$ which matches up well with the lattice constant, $a_0^f = 1.2374\text{nm}$, of pure YIG. The typical thickness of the substrates is $500\mu\text{m}$.

To obtain a substrate with a larger lattice constant to match up with desired garnet films that have larger ions such as Pr or Bi, additives such as calcium, magnesium and zirconium ions can be substituted in the melt during the boule growth. With these

substitutes, substrates with lattice constants in the range of 1.2382nm to 1.2511nm can be obtained [MaRu77], but with a stoichiometric balance, 1.2497nm is the common lattice constant for the calcium magnesium zirconium substituted gadolinium gallium garnet (SGGG).

The growth process for boule growth is the Czochralski method (CZ) which is a common crystal growth process often used to obtain single crystals of semiconductors, metals, salts, and synthetic gemstones.

Liquid Phase Epitaxy Film Growth

The Czochralski method cannot be used for growth of rare-earth iron garnets because they are not congruently melting compounds. Alternative growth methods have been developed such as liquid phase epitaxy (LPE), chemical vapor deposition (CVD), pulsed laser deposition (PLD), and rf-sputtering. The preferred method for film growth is the LPE method because it produces single crystal films with high crystalline quality. The LPE process for the deposition of garnet films is relatively well characterized, easy to handle, low cost and ready for mass production. The downsides of this method are that the growth conditions are difficult to control which makes consistency a challenge and that the growth rate is on the order of microns per minute. The high growth rate has been ideal for previous development of magneto-optical imagers but is considered a drawback for the growth of sub-micron thick films.

The LPE process involves dipping a garnet substrate into a supersaturated flux solution containing garnet constituents and uses lead-oxide (PbO) as a solvent. A schematic representation of the furnace used for LPE growth is shown in Figure 2.1(a)

while an image of the actual LPE growth system used at the Laboratory for Physical Sciences is presented in Figure 2.1(b).

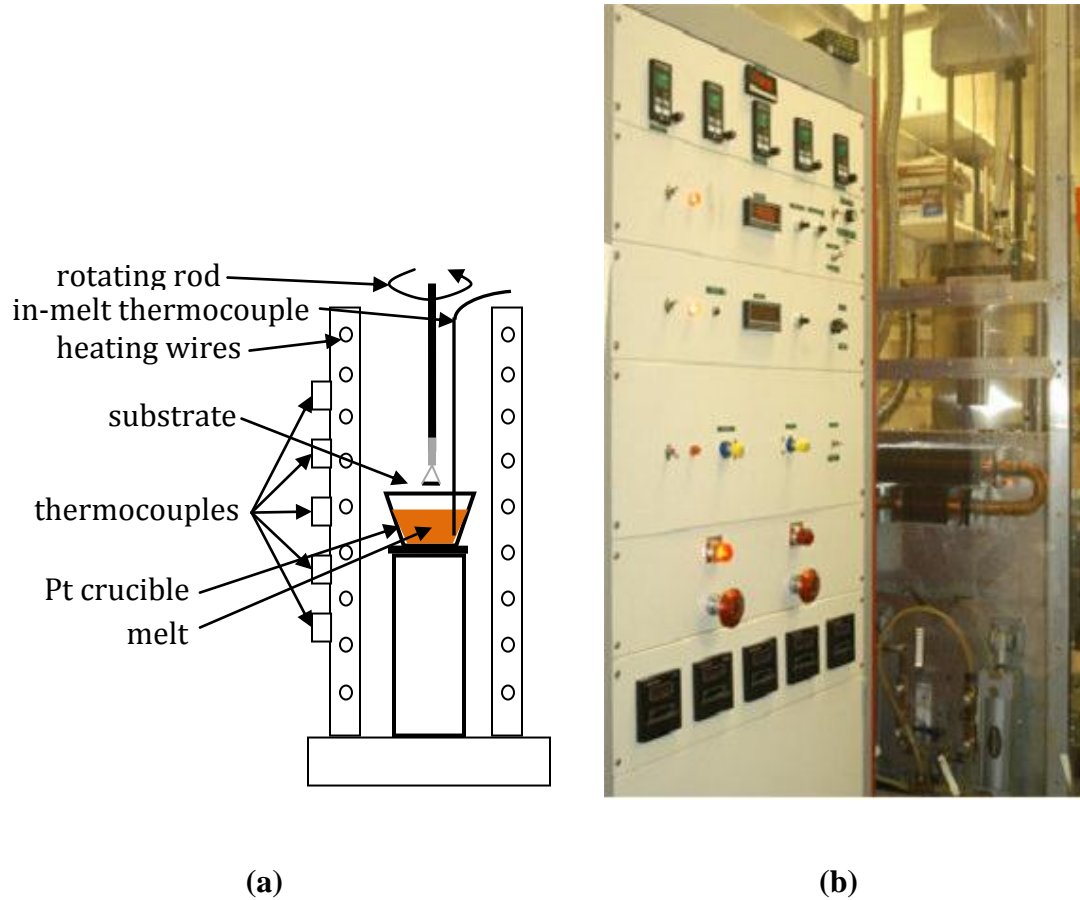


Figure 2.1: (a) Schematic drawing of the liquid phase epitaxy growth system. (b) Image of the actual LPE growth system used at the Laboratory for Physical Sciences.

The first step in the LPE growth process is the preparation of the melt. After careful melt design, the oxides are measured out to the appropriate amounts and pre-mixed inside a platinum crucible. Platinum is used because of its high melting point and its resistivity against the corrosive nature of the melt. The crucible is then placed inside the resistive heated five-zone furnace where the melt is homogenized by heating the

furnace at a temperature well above the melting point of the oxide mixture (900-950°C) for several hours and then stirring the melt with a platinum paddle.

After stirring the melt for 30 minutes, a temperature gradient is set for the five zones of the furnace to cool down the furnace in order to obtain a desired growth temperature. While the furnace is cooled down, the substrate is cleaned and prepared for growth. The substrate is horizontally placed into a platinum substrate holder and then carefully cleaned with acetone and ethyl alcohol, rinsed in distilled water, and etched in hot phosphoric acid to remove any impurities from its surface.

Once the desired undercooling (temperature below the saturation temperature of the melt) is reached, the solution is allowed to establish isothermal conditions. After inspecting the surface of the melt to insure that no surface nucleation has occurred, the platinum substrate holder is attached to the end of a long rod and slowly lowered into the furnace. The substrate must be lowered slowly into the furnace to allow equilibrium and avoid thermal shock. The substrate is lowered to a point just above the surface of the melt to allow for matching of the temperatures of the substrate and melt. This is done because growing the film on a cold substrate induces transition layers in the sample caused by different growth conditions at the substrate. Such transition layers causes non-uniformity of the film which is undesired.

After a waiting period to allow for the temperature matching, the substrate is lowered into the undercooled solution. Just as the substrate touches the melt surface, it is pulled up from the surface, keeping contact with the melt through the meniscus which is formed. As a result, film growth is on only one side of the substrate which helps simplify

characterization of the sample. The sample is rotated axially at a constant rate typically between 49 and 169 rpm. The speed of rotation affects the growth rate which has an effect on the material properties of the grown samples. Typical growth rates for the melt compositions and growth conditions described throughout this dissertation have ranged from 0.3 to 1.0 $\mu\text{m}/\text{min}$.

In order to grow high quality films using LPE, it is important to understand the chemistry and physics of the melt. Besides phase equilibrium and melt stability, phenomena such as boundary layer depletion and replenishment, and film/melt segregation must be understood and controlled. Since the crystallization of the sample occurs at the surface of the melt, the garnet constituents near the surface of the melt begin to decrease during growth. This creates a gradient in the garnet concentration in the melt near the surface. However, diffusion at the melt surface caused by the concentration gradient replenishes the melt surface to allow for further crystal growth. The balance between melt depletion and replenishment determines the growth rate of the melt. The growth rate can be increased by rotating the substrate which introduces a convective flow. Experimental data shows that the growth rate has a square root dependence on the rotation rate, ω , and has linear dependences on the undercooling, ΔT , and the concentration of garnet constituents, C [Esch81]:

$$\text{growth rate} \propto C \Delta T \omega^{1/2} \quad (1.59)$$

The growth time depends on the desired thickness of the sample. For a well characterized melt with a known growth profile based on growth conditions and melt composition, it is easy to estimate the growth time needed to obtain a sample with a

desired thickness. After the growth time has elapsed, the meniscus is broken and the sample is slowly removed from the furnace to avoid cracking of the film due to thermal shock.

Surface uniformity is important so removal of flux remnants from the surface is critical. The first method for removal of flux remnants is tilting. Tilting involves tilting of the entire furnace during growth so that when the sample is slowly removed from the melt, the flux on the surface won't form small droplets and instead, the adhesion forces from the melt surface will retain the flux remains thus yielding a cleaner surface. The tilting method is not perfect, however, and often results in a flux remain in one corner of the sample. The other method is called spin-off. Spin-off takes place as soon as the sample is removed from the melt, in which case the speed of rotation is increased to 400 rpm to utilize centripetal force to spin off the remnants of the flux. A combination of tilting followed by spin-off has also been used and in some cases has yielded better results than either method separately.

Once the sample is removed from the furnace, the sample is cooled down for a few minutes until it reaches room temperature. The sample is then cleaned in a hot solution of nitric acid (10%), acetic acid (10%), and distilled water (80%) for 30 minutes. The sample is rinsed with distilled water and then placed in a solution of hydrochloric acid (50%) and distilled water (50%) at room temperature for an additional 30 minutes. This cleaning process is used to remove any left-over flux that remains on the sample surface.

After a film has been grown from the melt, the conditions of the melt have been changed. This makes it undesirable to grow another sample right away because the film reproducibility would suffer. Therefore, if it is desired to grow another film, the furnace is heated back up above the saturation temperature and the solution is homogenized again for several hours before the next film can be grown.

Melt Engineering

In order to obtain a sample with desired film composition and properties, a melt must be designed to yield such results. Characterization of the film composition of rare-earth iron garnet films is difficult without using destructive means. Segregation coefficients and other parameters calculated for similar films can, however, be used to help estimate the expected results. The melt contains a mixture of oxides of the rare-earths, iron and iron substitutes such as Ga, along with lead oxide (PbO) and boron oxide (B₂O₃) flux. The bismuth oxide (Bi₂O₃) is part of both the flux and garnet phases. The design of a melt is a very delicate process. Not only do the material properties of a grown film depend on the carefully selected melt composition, but the growth of garnet itself is dependent on the composition of the melt. To demonstrate the point, consider the pseudo-ternary mixture PbO-Y₂O₃-Fe₂O₃, illustrated in Figure 2.2 [Niel58]. Depending on where the overall composition of the film is, one of four crystallization phases is possible: hematite (Fe₂O₃), magnetoplumbite (PbFe₁₂O₁₉), garnet (RE₃Fe₅O₁₂) and orthoferrite (REFeO₃). While this example is elementary compared to the usual garnet constituents, the more complex garnet pseudo-ternary mixture can be thought of as flux- Σ RE₂O₃- Σ Fe₂O₃, Ga₂O₃.

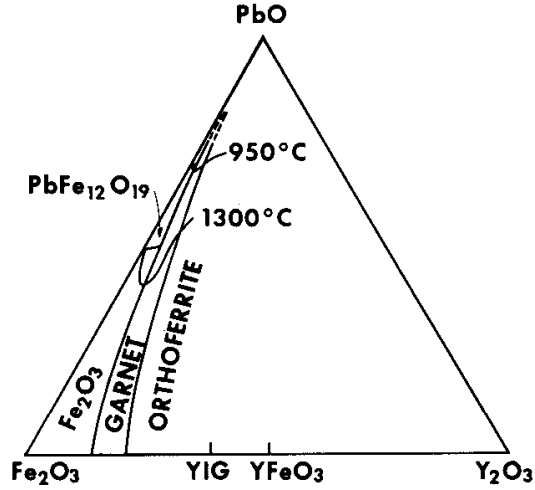


Figure 2.2: Pseudo-ternary PbO-Y₂O₃-Fe₂O₃ phase equilibrium diagram showing four primary phase fields: hematite, magnetoplumbite, garnet, and orthoferrite [Blan72].

The melt design is governed by a set of cation ratios that determine the characteristics of the melt and composition and properties of the grown film. These ratios are [Blan72]:

$$\frac{G}{F} = \frac{\sum RE + [Fe] + [Ga] + [Al]}{[Pb] + [Bi] + [B]} \quad (1.60)$$

$$C_{Bi} = \frac{[Bi]}{[Pb] + [Bi]} \quad (1.61)$$

$$C_B = \frac{[B]}{[Pb] + [Bi]} \quad (1.62)$$

$$R_1 = \frac{[Fe] + [Ga] + [Al]}{\sum RE} \quad (1.63)$$

$$R_2 = \frac{[Fe]}{[Ga] + [Al]} \quad (1.64)$$

The square bracket notations denote the corresponding cation concentrations. G/F is the garnet to flux ratio which is the ratio of the sum of the garnet-forming oxides to the sum of the flux oxides in the melt. G/F typically ranges from 0.12 to 0.2 and controls the saturation temperature of the melt and the growth rate of the sample. C_{Bi} denotes the bismuth concentration in the melt and is given by the ratio of bismuth to the sum of lead and bismuth. It controls the bismuth incorporation in the epitaxial film and usually ranges from 0.2 to 0.8. C_B is the boron concentration in the melt and is the ratio of boron to the sum of lead and bismuth. Boron has a strong effect on the saturation temperature of the melt. Boron stabilizes the melt allowing for large undercooling and also controls the melt viscosity. Increasing C_B increases the viscosity of the melt. Typical values for C_B range from 0 to 0.25. R_1 is the ratio of iron oxide and its substituents to the rare-earth oxides in the melt. It is generally much higher than the stoichiometric value $5/3$ and typically ranges anywhere from 7.5 to 19. Increasing R_1 decreases the saturation temperature of the melt and increases the bismuth incorporation in the epitaxial film. R_2 is the ratio of iron to its substituents. It controls the diamagnetic substitutions and affects the saturation magnetization. Increasing the iron substituents in the octahedral and tetrahedral sites decreases the saturation magnetization, $4\pi M_S$.

In order to calculate how much of each oxide goes into the melt, some conversions need to be made. First, the cation percentages of each element need to be calculated from the cation ratios:

$$F = \frac{100}{\frac{G}{F} + 1} \quad (1.65)$$

$$G = 100 - F \quad (1.66)$$

$$[B] = \frac{C_B}{1 + C_B} F = \frac{[B]/([Bi] + [Pb])}{1 + [B]/([Bi] + [Pb])} F = \frac{[B]}{F} F \quad (1.67)$$

$$[Bi] = C_{Bi}(F - [B]) = \frac{[Bi]}{[Bi] + [Pb]} ([B] + [Bi] + [Pb] - [B]) \quad (1.68)$$

$$[Pb] = F - [Bi] - [B]$$

$$[Ga] + [Al] = \frac{G}{R_2 + 1 + \frac{R_2 + 1}{R_1}} = \frac{\sum RE + [Fe] + [Ga] + [Al]}{\frac{[Fe] + [Ga] + [Al]}{[Ga] + [Al]} + \frac{\sum RE}{[Ga] + [Al]}} \quad (1.69)$$

$$[Fe] = R_2([Ga] + [Al]) = \frac{[Fe]}{[Ga] + [Al]} ([Ga] + [Al]) \quad (1.70)$$

$$\sum RE = G - [Fe] - ([Ga] + [Al]) \quad (1.71)$$

Next, the molar percentages can be calculated using the cation ratios and the stoichiometric formulas for each oxide. Finally, based on the molar percentages and the molar mass of each oxide, the amount of each oxide in grams can be determined. Depending on the desired weight of the melt, the amount of each oxide can be scaled accordingly.

Chapter 3: Plasmon Resonances and Numerical Modeling

It has been shown in Chapter 1 that the magneto-optic effects are controlled by the spin-orbit interaction. The Hamiltonian for the spin-orbit interaction, Eq. 1.35, suggests that the spin-orbit interaction depends on local electric fields ($-\nabla V$). This implies that the enhancement of the local electric fields could potentially enhance the magneto-optic effects. Local electric fields can be enhanced by exciting plasmon resonances in metallic nanoparticles in the vicinity of magnetic garnet thin films. This chapter will focus on the theory of plasmon resonances and numerical modeling of plasmon resonances in metallic nanoparticles.

Plasmon Resonances as an Eigenvalue Problem

It is known that small dielectric objects can exhibit resonance behavior at certain frequencies for which their dielectric permittivities are negative and their dimensions are small in comparison to the free-space wavelength. These resonances can therefore be considered electrostatic in nature since the dimensions of the dielectric objects are smaller than the free-space wavelength. The physical mechanism of these resonances originates at specific negative values of dielectric permittivity for which source-free electrostatic fields may exist.

By treating this complicated electrostatic problem as an eigenvalue problem for a specific boundary integral equation, the calculations have been simplified [FrMa03]. The negative dielectric permittivity and corresponding values of resonance frequency can be directly calculated from the eigenvalue problem. The treatment of the electrostatic problem as an eigenvalue problem also reveals a unique physical property of electrostatic

resonances: the resonance frequencies depend on the shape of the dielectric objects but are scale invariant with respect to geometric dimensions, provided that they remain appreciably smaller than the free-space wavelength.

The eigenmodes of this eigenvalue problem are the resonance modes of the dielectric objects. Strong orthogonality properties of these modes are usually obtained and have physical importance for selection of resonance modes that can couple with the incident electromagnetic radiation.

Electrostatic Model of Small Dielectric Objects

Consider a dielectric object of arbitrary shape and permittivity ϵ (see Figure 3.1).

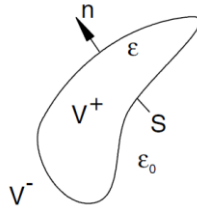


Figure 3.1: The dielectric region V^+ bounded by the surface S [FrMa03].

From the conditions presented in the previous section, only negative values of ϵ for which a source-free electrostatic field may exist are of interest. The source-free field is curl and divergence free both inside (V^+) and outside (V^-) the dielectric object [FrMa03]. As a result, the electric potential is continuous across the boundary, S , of the object while the normal components of the electric field satisfy the boundary condition:

$$\epsilon E_n^+ = \epsilon_0 E_n^- \text{ on } S. \quad (3.1)$$

The electric potential of this source-free field can be represented as an electric potential of a single layer of electric charges, σ , distributed over the surface of the object, S :

$$\varphi(Q) = \frac{1}{4\pi\epsilon_0} \int_S \frac{\sigma(M)}{r_{MQ}} dS_M \quad (3.2)$$

where Q is the point of observation and M is the point of interest on the surface of the object. In essence, the single layer of charges (σ) on S creates the same electric field in the free-space as the source-free electric field that may exist in the presence of the dielectric object. In order to satisfy the boundary condition in Eq. 3.1, the normal components of the electric field of a single layer potential can be given by the formula

$$E_n^\pm(Q) = \mp \frac{\sigma(Q)}{2\epsilon_0} + \frac{1}{4\pi\epsilon_0} \int_S \sigma(M) \frac{r_{MQ} \cdot n_Q}{r_{MQ}^3} dS_M. \quad (3.3)$$

The homogeneous boundary integral equation is derived by substituting Eq. 3.3 into the boundary condition Eq. 3.1:

$$\sigma(Q) = \frac{\lambda}{2\pi} \int_S \sigma(M) \frac{r_{MQ} \cdot n_Q}{r_{MQ}^3} dS_M, \quad (3.4)$$

where

$$\lambda = \frac{\epsilon - \epsilon_0}{\epsilon + \epsilon_0}. \quad (3.5)$$

This means that the source-free electric fields may only exist for such values of permittivity, ϵ , that Eq. 3.4 has nonzero solutions. In other words, the eigenvalues and

eigenfunctions of the integral equation, Eq. 3.4, must be found in order to find the resonance values of ϵ as well as the resonance modes [FrMa03].

Numerical Modeling of Plasmon Resonance Enhancement of Magneto-Optical Effects in Garnets

On a microscopic level, magneto-optic effects are controlled by spin-orbit coupling, as explained in Chapter 1. The spin-orbit coupling Hamiltonian given in Eq. 1.35 suggests that spin-orbit coupling depends on local electric fields ($-\nabla V$). These electric fields can be optically induced by exciting plasmon resonances in metallic nanoparticles incorporated on the surface or embedded in magneto-optic media. Therefore, plasmon resonances in the metallic nanoparticles can be utilized for the enhancement of magneto-optic effects.

Proper control of the plasmon resonances in metallic nanoparticles is critical to the efficient plasmon resonance enhancement of magneto-optic effects. The nanoparticles must be designed in such a way that they resonate in the wavelength range where the plasmon resonances are most strongly pronounced, provide uniform spreading of the electric fields induced by the plasmon resonances over the thickness of the sample, and efficiently couple the incident optical radiation with the desired plasmon resonance modes [Maye10].

In order to design the nanoparticles so that they will resonate in the desired optical frequency range, simulations have been performed. These simulations have been performed using Matlab programs based on the eigenvalue problem formulated in the previous section. The simulation software inputs a geometric array of wireframe

nanoparticles and calculates the resonance modes and corresponding resonance frequencies. Equation 3.4 is transformed into

$$\sigma_k(Q) = \frac{\lambda_k}{2\pi} \int_S \sigma_k(M) \frac{r_{MQ} \cdot n_Q}{r_{MQ}^3} dS_M, \quad (3.6)$$

where the negative resonance values, ε_k , are related to the eigenvalues, λ_k , by the formula

$$\lambda_k = \frac{\varepsilon_k - \varepsilon_0}{\varepsilon_k + \varepsilon_0} \quad (3.7)$$

while $\sigma_k(M)$ has the physical meaning of surface electric charges on the particle boundary S that produce electric field \vec{E}_k of the k-th plasmon mode.

Equation 3.6 can be re-written as

$$\sigma_k(Q) = \frac{\lambda_k}{2\pi} \int_S \sigma_k(M) \frac{\partial G(M, Q)}{\partial n_Q} dS_M \quad (3.8)$$

where G(M, Q) is the Green's function which accounts for the garnet plane boundary. For the case where the nanoparticles are placed on the garnet surface (see Figure 3.2(a)), G(M, Q) is given by

$$G(M, Q) = \frac{1}{r_{MQ}} - \frac{\varepsilon_g - \varepsilon_0}{\varepsilon_g + \varepsilon_0} \frac{1}{r_{M'Q}} \quad (3.9)$$

where M' is the mirror-image point of M with respect to the garnet plane boundary and ε_g is the dielectric permittivity of the garnet film. For the case where the nanoparticles are embedded in the garnet film (see Figure 3.2(b)), Eq. 3.9 is modified as follows

$$G(M, Q) = \frac{1}{r_{MQ}} - \frac{\varepsilon_0 - \varepsilon_g}{\varepsilon_0 + \varepsilon_g} \frac{1}{r_{M'Q}}. \quad (3.10)$$

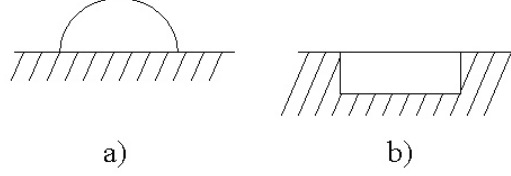


Figure 3.2: Schematic image of nanoparticles (a) placed on the surface of the garnet film and (b) embedded in the garnet film surface [Maye10].

Once the eigenvalues, λ_k , are computed through the solution of Eq. 3.8 and resonance values, ε_k , of permittivity are found by using Eq. 3.7, the resonance frequencies, ω_k , are determined from the dispersion relation

$$\varepsilon_k = \varepsilon'(\omega_k), \quad (3.11)$$

where $\varepsilon'(\omega)$ is the real part of the dielectric permittivity, $\varepsilon(\omega)$, of the metallic nanoparticles. From known dispersive information for gold or silver, the calculated resonance value, ε_k , is matched to the real part of the dielectric permittivity of gold or silver in a look-up table and the corresponding resonance frequency is obtained.

It is important to notice that Eq. 3.9 is invariant with respect to the scaling of the dimensions of the nanoparticles which implies that plasmon resonance frequencies and resonance wavelengths are scale invariant and only depend on the shape of the nanoparticles but not their dimensions provided that the resonance wavelengths are much larger than the dimensions of the nanoparticles. This is a beneficial property for plasmon resonance enhancement of magneto-optic effects because when the nanoparticles are

formed, their shapes are the same but their dimensions vary which means that all of the nanoparticles can simultaneously resonate at the same wavelength of incident optical radiation and collectively contribute to the enhancement of magneto-optic effects.

In order to understand how the incident optical radiation is coupled to specific plasmon modes, the boundary charges, $\sigma(M, t)$, induced on the particle boundaries during the excitation process are expanded in terms of plasmon modes, $\sigma_k(M)$, as follows

$$\sigma(M, t) = \sum_{k=1}^{\infty} a_k(t) \sigma_k(M). \quad (3.12)$$

When the incident optical radiation has the same frequency as the resonance frequency, ω_k , of the k-th plasmon mode, the coefficient, $a_k(t)$, in Eq. 3.12 is strongly dominant and under steady state conditions, $a_k^{SS}(t)$ is given by the formula

$$a_k^{SS}(t) = -(E_0 \cdot p_k) \frac{\varepsilon'(\omega_k) - \varepsilon_0}{\varepsilon''(\omega_k)} \cos \omega_k t, \quad (3.13)$$

where E_0 is the electric field of the incident radiation, p_k is the dipole moment of the k-th plasmon mode, and $\varepsilon''(\omega_k)$ is the imaginary part of $\varepsilon(\omega)$ [MaZM07].

From Eq. 3.13, it is clear that the coupling of the incident optical radiation to the desired plasmon modes originates from the dot product of the electric field with the dipole moment. From the nature of the dot product, the desired plasmon modes are most efficiently excited when the direction of the polarization of the incident radiation coincides with the direction of the dipole moment, p_k , of the plasmon modes.

Equation 3.13 contains the ratio of the real to imaginary parts of the dielectric permittivity of metallic nanoparticles at the resonances frequency which suggests that the resonance electric field, and consequently the enhancement of the magneto-optic effects, is controlled by the magnitude of this ratio.

For gold and silver, this ratio of the real to imaginary components of the dielectric permittivity is largest when the free-space wavelength is within the respective ranges of 700-900nm and 800-1100nm with ratio values of about 16 and 85, respectively [JoCh72]. Therefore, it is ideal to tune the shape and configuration of the nanoparticles in such a way that the plasmon resonance frequency is within the above frequency ranges since the plasmon resonances can be most efficiently excited in these ranges.

For off-resonance excitation, $f(t) = \sin \omega_0 t$, similar calculations lead to the expansion of $a_k^{SS}(t)$ for off-resonance frequency, ω_0 , as follows [MaZM07]

$$a_k^{SS}(t) = (E_0 \cdot p_k)C(\omega_0) \cos(\omega_0 t + \varphi), \quad (3.14)$$

where

$$C(\omega_0) = \sqrt{\frac{[\varepsilon'(\omega_0) - \varepsilon_0]^2 + [\varepsilon''(\omega_0)]^2}{[\varepsilon_k - \varepsilon'(\omega_0)]^2 + [\varepsilon''(\omega_0)]^2}} \quad (3.15)$$

Equation 3.15 reveals the sharpness of the plasmon resonances and the optical frequency range where these resonances may enhance magneto-optic effects.

While the ratio of the real to imaginary components of the dielectric permittivity of silver (85) is larger than that of gold (16), silver oxidizes which makes it difficult to

use in experiments. Therefore, gold has been used for both the simulations and experiments described throughout this dissertation.

Numerical simulations have been performed for various geometries and spatial arrangements of hemispherical gold nanoparticles. A single hemispherical gold nanoparticle on the surface of a garnet film has first been modeled (see Figure 3.3) to calculate the dependence of the resonance wavelength on the height-to-radius ratio of the single nanoparticle.

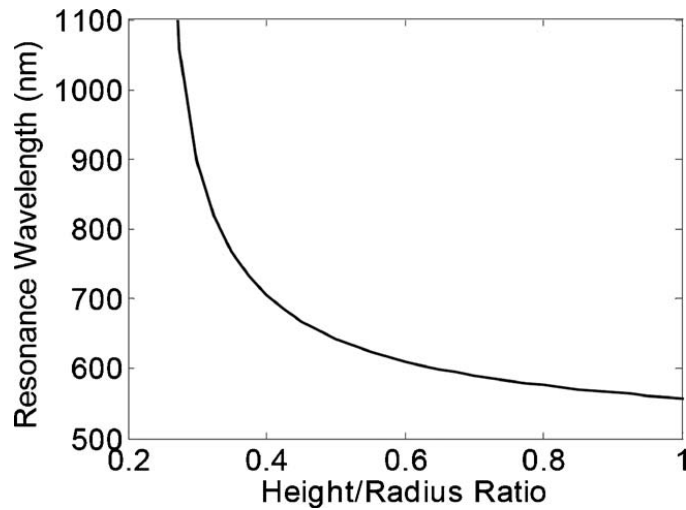


Figure 3.3: The dependence of resonance wavelength on the height-to-radius ratio of a single hemispherical gold nanoparticle [Maye10].

It is apparent from Figure 3.3 that the resonance wavelength varies from around 550 nm to 620 nm when the height-to-radius ratio varies between 1 and 0.5, respectively. The results shown in Figure 3.3 further suggest that by reducing the height-to-radius aspect ratio, the resonance wavelength could be shifted into the 700-900nm range where the plasmon resonances are most pronounced due to the larger ratio of the real to imaginary components of the dielectric permittivity of gold.

Simulations have also been performed for two and four hemispherical gold nanoparticles with varied geometries and spacing (see Figure 3.4).

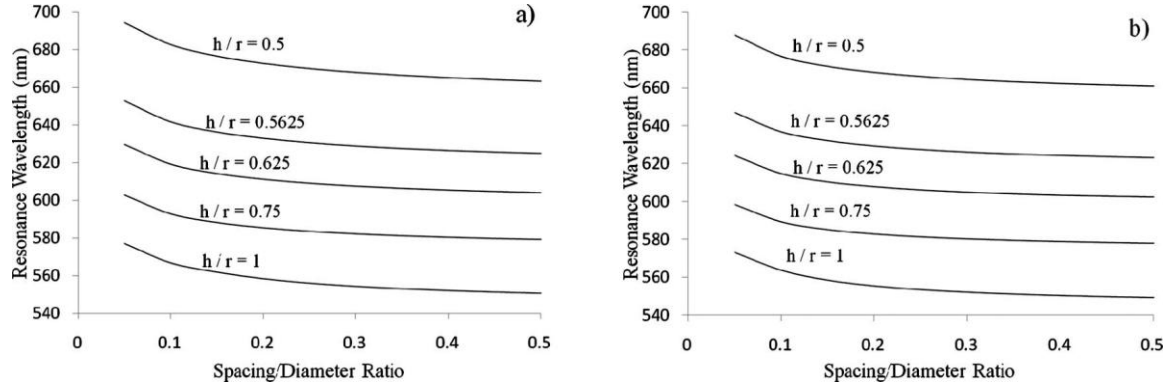


Figure 3.4: The dependence of the resonance wavelength on the spacing between (a) two and (b) four adjacent gold hemispherical nanoparticles. The ratio of the height to the radius is denoted by h/t [Maye10].

The results from the two and four nanoparticle simulations show that if the spacing-to-diameter ratio is above 0.3, the resonance wavelength is practically the same as for a single hemispherical nanoparticle, and therefore act as single particles. Furthermore, it is evident that there is not much of a noticeable difference between the results for two adjacent nanoparticles and four adjacent nanoparticles. This suggests that similar results could be expected for more than four nanoparticles in close proximity.

When modeling a single nanoparticle, it has been found that the induced electric field is more uniformly spread over the thickness of the garnet film when the nanoparticle is embedded in the garnet film. When conceptualizing how the nanoparticles could be embedded in the garnet films, methods such as ion beam milling had been investigated to create holes in the garnet surface that could then be filled with gold using the evaporation technique. For this reason, the embedded particles have been modeled as cylinders and

not hemispheres as is the case for the nanoparticles modeled on the surface of the garnet films. Numerical simulations have been performed for two cylindrical nanoparticles with various geometries and spacing (see Figure 3.5) and the distribution of the plasmon electric field induced by the excitation of the plasmon resonances in the particles has been calculated (see Figure 3.6).

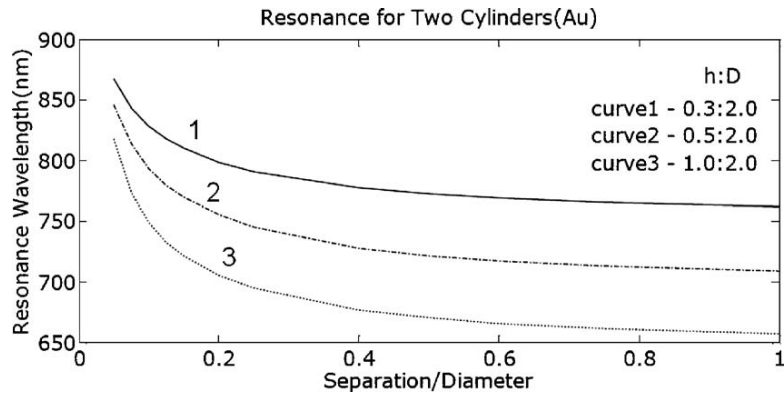


Figure 3.5: Resonance wavelength as a function of particle geometry and spacing for two cylindrical gold nanoparticles [Maye10].

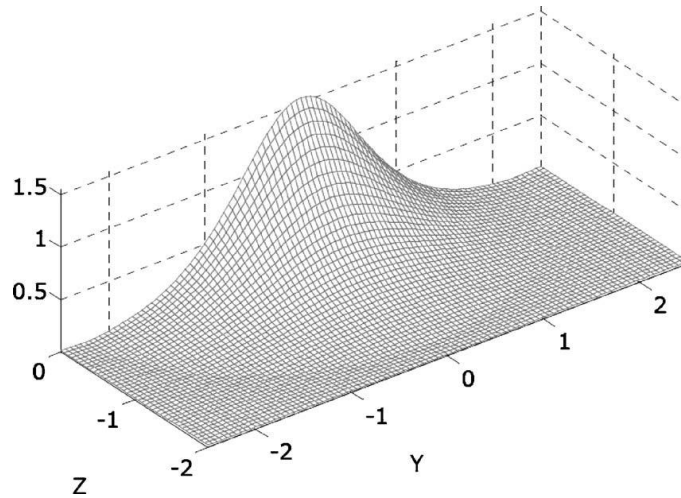


Figure 3.6: Distribution of the plasmon electric field in the midplane between two embedded cylindrical gold nanoparticles [Maye10].

By controlling the spacing between particles, the strength and distribution of the induced electric field could be controlled. The z-axis in Figure 3.6 shows the depth of penetration of the field into the magneto-optic media scaled to the nanoparticle dimensions. According to Figure 3.6, if the height of the nanoparticles is 50nm, the electric field will penetrate a maximum of about 80nm into the magneto-optic media, almost 2 times the height. The limitation of the extent of penetration of the plasmon resonance induced electric fields into the magneto-optic media suggests that sub-micron thick films are necessary to obtain a uniform spread of the induced electric fields over the thickness of the sample.

Chapter 4: Characterization of the Garnet Films

Lattice Mismatch Measurement

With the liquid phase epitaxy film growth technique, garnet films are grown on non-magnetic substrates. Depending on the growth conditions and the composition of the melt, the epitaxially grown film is supposed to follow the same crystallographic structure as the substrate but often times, there is a mismatch between the lattice constant of the film (a_0^f) and the lattice constant of the substrate (a_0^s). Since the substrate's thickness is very large in comparison to the thickness of the grown film, the substrate's lattice constant will not change under strain. The film will elastically deform in such a way that its lattice will match that of the substrate in the horizontal direction along the interface. This deformation has to be compensated for in the direction perpendicular to the interface, causing the lattice structure of the film to become irregular.

The mismatch in the perpendicular lattice spacing of the film and the substrate is called the lattice mismatch and can be measured using x-ray diffraction (XRD). The perpendicular lattice mismatch is given by the following formula:

$$\Delta a_{\perp} = a_0^s - a_0^f. \quad (4.1)$$

The lattice mismatch value must be sufficiently small, in the range of $-0.07\text{\AA} < \Delta a_{\perp} < 0.03\text{\AA}$, in order for the film to grow on the substrate as a single crystal [Holt04].

If the film's lattice constant is larger than the substrate's lattice constant ($\Delta a_{\perp} < 0$) then the film is under compression; likewise, if the film's lattice constant is smaller

than the substrate's lattice constant ($\Delta a_{\perp} > 0$) then the film is under tension (see Figure 4.1).

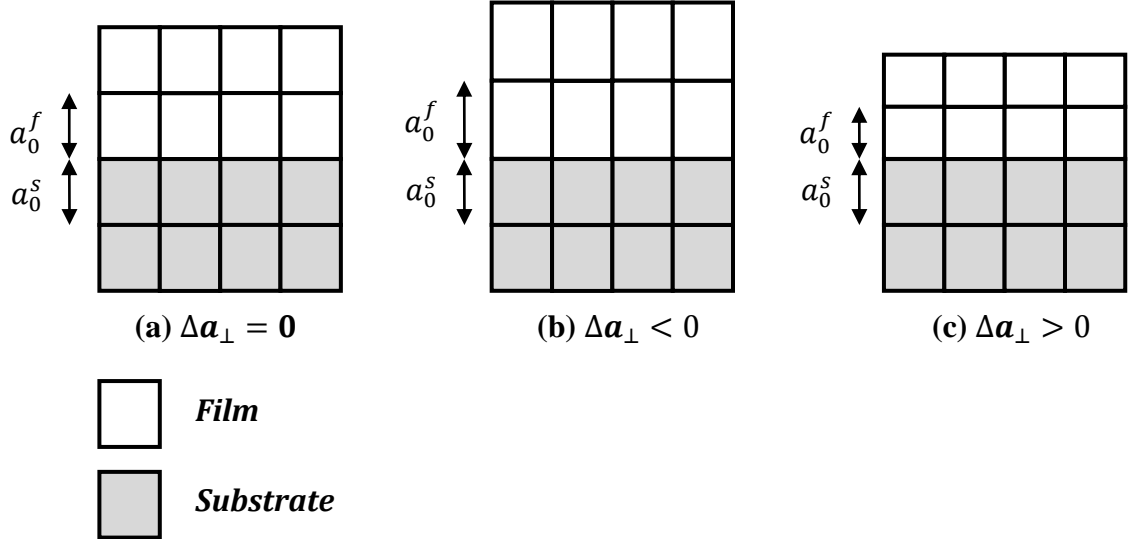


Figure 4.1: Lattice mismatch between the epitaxially grown garnet film and the substrate: (a) no mismatch, (b) film under compression, (c) film is under tension.

The x-ray diffractometer used in the measurements has an x-ray source emitting at the CuK_{α} lines with wavelengths $\lambda_1=0.15404\text{nm}$ and $\lambda_2=0.15444\text{nm}$. The beam is reflected off a GaAs crystal under the (400) or (800) directions. The detector and the sample are moved in such a way that the angle between the sample surface and the incident beam is always θ , and the angle between the incidence angle and the beam is always 2θ . The signal of the scintillation counter depends on the incidence angle θ and has a maximum if the Bragg condition is fulfilled:

$$m\lambda = 2d_{hkl} \sin \theta, \quad (4.2)$$

where $m=1,2,3,\dots$ is an integer and d_{hkl} is the atomic plane spacing.

The lattice mismatch can be calculated using the following equation:

$$\Delta a_{\perp} = \frac{\lambda_{\alpha} \sqrt{h^2 + k^2 + l^2}}{2} \left(\frac{1}{\sin \theta_s} - \frac{1}{\sin \theta_f} \right), \quad (4.3)$$

where (h, k, l) are the Miller indices, and θ_s and θ_f are the angles of maximum intensity for the substrate and film, respectively. Larger Miller indices provide measurements with better resolution. For (100)-oriented samples, the (8,0,0) diffraction peak is used with $\theta_s = 59.7^{\circ}$.

The diffractometer used for these measurements cannot measure the absolute values of the angles, but rather the relative values of the angles. Therefore, Eq. 4.3 cannot be used directly to calculate the lattice mismatch. Instead, since the peak separation $\Delta\theta$ is very small compared to θ_s , a linear approximation can be made [Nist06]:

$$\sin \theta_f = \sin(\theta_s + \Delta\theta) = \sin \theta_s + \Delta\theta \cos \theta_s. \quad (4.4)$$

Using the approximation in Eq. 4.4, Eq. 4.3 becomes:

$$\Delta a_{\perp} = \frac{\lambda_{\alpha} \sqrt{h^2 + k^2 + l^2}}{2} \left(\frac{1}{\sin \theta_s} - \frac{1}{\sin \theta_f} \right) = a_0^s \frac{\Delta\theta}{\tan \theta_s} \quad (4.5)$$

where $\lambda_{\alpha} = \frac{2a_0^s \sin \theta_s}{\sqrt{h^2 + k^2 + l^2}}$ is the Bragg condition. Equation 4.5 has to be corrected for elastic strain, yielding:

$$\Delta a_{\perp} = a_0^s \frac{1 - \nu}{1 + \nu} \frac{\Delta\theta}{\tan \theta_s} \quad (4.6)$$

where $\nu = 0.296$ is the Poisson Ratio. The values measured with the diffractometer are substituted into Eq. 4.6 to calculate the lattice mismatch between the film and the substrate.

Film Thickness Measurement

Measurement of the film thickness is one of the most important properties to measure because the film thickness is used to calculate parameters such as the growth rate and the specific Faraday rotation. The thickness is measured using a J.A. Woollam VASE ellipsometer with uv/visible and near infrared gratings. For sub-micron thick samples, use of the uv/visible grating is preferred over the infrared grating since the infrared grating is better suited for measurements of films that are several microns in thickness. The angle of incidence is set at $\theta_i = 45^\circ$ and the wavelength of the light is swept from 500nm to 1000nm in 2nm increments.

The thickness measurements are based on the principal of interference between multiple reflections from the air-film and film-substrate interfaces. Light with different wavelengths will travel different paths through the material and for some wavelengths the constructive interference condition is satisfied while other wavelengths suffer destructive interference. By measuring the intensity of the reflected beam at the different wavelengths that are swept over, peaks are observed in the output signal when constructive interference occurs. An example of a typical optical signal obtained for a thickness measurement is shown in Figure 4.2.

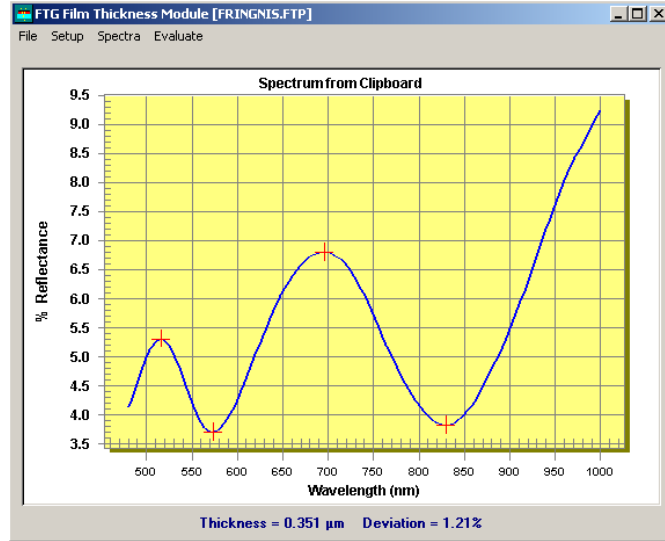


Figure 4.2: Typical optical reflectance signal measured using the ellipsometer being analyzed in the FTG Film Thickness Module to calculate the film thickness.

Given the wavelengths for the positions of the maxima in the reflected signal, the following equation can be used to determine the thickness of the measured sample [Nist06]:

$$t = \frac{\frac{1}{2}(N_1 - N_2) \sqrt{n_f^2 - \sin^2 \theta_i}}{n_f^2 \left(\frac{1}{\lambda_1} - \frac{1}{\lambda_2} \right)} \quad (4.7)$$

where n_f is the index of refraction of the film, and λ_1 and λ_2 are the wavelengths that correspond to the N_1 and N_2 peaks, respectively.

Transmission Measurements

The ellipsometer is used for more than just thickness measurements. Transmission coefficient measurements can also be performed using the ellipsometer to determine the presence of gold nanoparticles on the surface of the substrates and presence

of embedded gold nanoparticles after film growth by calculating absorption due to plasmon resonances excited in the gold nanoparticles.

The transmission measurements are performed in a perpendicular geometry where the incident light is normal to the film surface. The wavelength of the light is swept from 500 nm to 1000 nm in 2 nm increments. By measuring the intensity of the transmitted beam in comparison to the incident beam, the amount of light that is transmitted at different wavelengths is calculated (see Figure 4.3(a)). The result of this comparison is called the transmittance and is a measurement of the percentage of light that is transmitted through the sample.

By taking measurements at adjacent points on the sample in regions with and without gold nanoparticles, the transmission through the two regions can be compared. The absorption due to plasmon resonances in the gold nanoparticles can be derived from the comparison of the transmission coefficient curves by taking the difference between the transmission coefficient values for the area with gold and the transmission coefficient values for the area without gold. The resultant is a plasmon resonance peak that reveals plasmon resonance absorption versus wavelength. An example of the absorption calculation is shown in Figure 4.3(b).

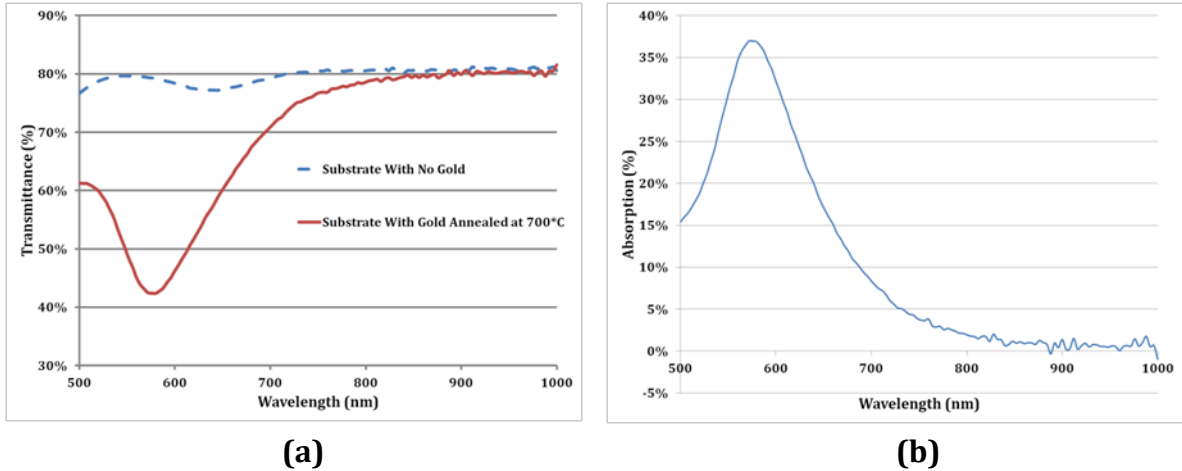


Figure 4.3: (a) Transmittance measurements for adjacent regions of a SGGG (100)-oriented substrate with gold nanoparticles populated on the surface (solid) and without gold nanoparticles (dashed). (b) Absorption due to plasmon resonances in the gold nanoparticles calculated from the two curves in (a).

Atomic Force Microscopy (AFM) Measurements

Atomic force microscopy (AFM) is used to capture images of the surface of substrates and samples. Gold nanoparticles are used to excite plasmon resonances that induce strong localized electric fields in the garnet films. It is therefore necessary to characterize the nanoparticle assemblies formed on the surfaces of garnet substrates and garnet films. AFM images of gold nanoparticles on the surfaces of substrates and samples can be analyzed using image processing in the AFM software to determine the dimensions and separation of the gold nanoparticles.

AFM measurements take a surface profile of the substrates and reveal the height and steepness of the nanoparticles along with their diameters. Small sections of the substrate surfaces are captured in the regions with and without gold nanoparticles to verify consistency of the nanoparticles assemblies and confirm that there are no

nanoparticles formed in the regions where gold had not been deposited. The size of the scans typically ranges from $1 \mu\text{m}^2$ to $20 \mu\text{m}^2$. The results for a typical AFM measurement are shown in Figure 4.4.

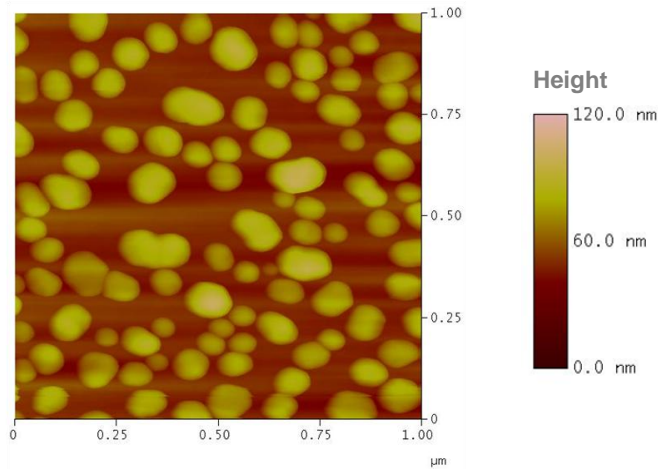


Figure 4.4: Typical atomic force microscopy measurement of the gold nanoparticles on a substrate surface. The vertical bar on the right is the scale for the height of the nanoparticles.

Once a measurement is complete, the results are processed to determine parameters of the nanoparticle assemblies such as average particle size, particle spacing, density of particles, and surface roughness.

Optical Hysteresis Loop Measurements

Optical hysteresis loop measurements are used to measure the Faraday rotation of a sample as a function of the applied magnetic field. The specific Faraday rotation, saturation magnetic field and coercivity field can be extracted from the measured loop data.

The experimental setup used for the optical hysteresis loop measurements is shown in Figure 4.5. The setup consists of a laser (L), two linear polarizers (P and A), a

ring shaped electromagnet with a gap cut in it (M), and a detector (D). The laser is either a red (633 nm) or green (532 nm) frequency stabilized laser. The beam is emitted from the laser and passes through a Glan-Thompson linear polarizer (P) that outputs linearly polarized light. The linearly polarized light then passes through the sample (S) that is mounted on a three-axis translational stage. The propagating beam experiences the Faraday Effect as it passes through the sample under the influence of an externally applied magnetic field perpendicular to the sample surface.

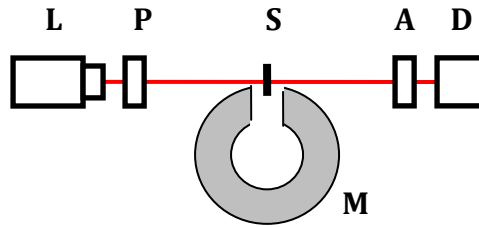


Figure 4.5: Optical hysteresis loop measurement experimental setup. The light from the laser (L) is linearly polarized by the polarizer (P) and then propagates through the sample (S) which is magnetized normal to the sample surface by the magnet (M). The transmitted beam then passed through the analyzer (A) which is another linear polarizer and finally reaches the detector (D) which is hooked up to the computer that measures the results.

The analyzer (A) is another Glan-Thompson linear polarizer mounted on an optical rotation stage. The optical rotation stage orients the analyzer so that the relative angle between the analyzer and the polarizer (P) is 45° . The analyzer acts as a reference to determine the relative change in the Faraday rotation angle which is subsequently proportional to the change in the intensity of the optical signal measured by the detector. The detector is attached to both an oscilloscope and a National Instruments NI USB-6229 data acquisition module (DAQ) that is used to capture the optical signal at the detector.

A computer is interfaced with the DAQ and samples the optical signal from the detector. A gaussmeter probe is also mounted at the center of the poles of the magnet to measure the magnetic field strength at the location where the laser beam is incident upon the sample.

A program has been designed in LabView to control the output voltage signal that is applied to the voltage controlled current source attached to the electromagnetic. By managing the voltage output at each increment of the measurement, the applied magnetic field perpendicular to the sample surface can be swept over a given range. The LabView program also synchronously captures the magnitude of the magnetic field measured by the gaussmeter and the optical signal measured by the detector. At each increment of the output voltage signal, several thousand data points are captured for both the magnetic field signal and the optical signal which are then post-processed by the LabView program. Upon post-processing, for every increment of the output voltage applied to the current source that controls the magnet, a pair of values is calculated which represent the average magnetic field magnitude and optical signal magnitude for the given applied output voltage. The averaged values are stored into a data table and later used to extract additional information.

An optical hysteresis loop can be obtained by plotting the data points in the data table for each measurement increment (see Figure 4.6). The magnitude of the optical signal is on the vertical axis and the magnitude of the applied magnetic field is on the horizontal axis.

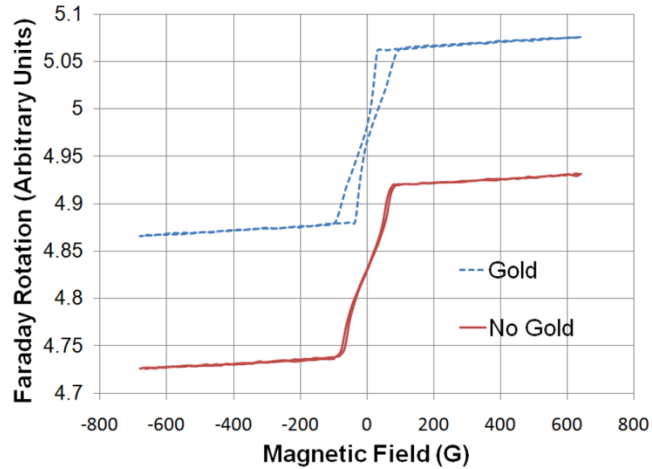


Figure 4.6: Typical optical hysteresis loop measurements obtained for samples with out-of-plane magnetization.

The saturation magnetic field and specific Faraday rotation can be calculated from an optical hysteresis loop by determining the point on the curve where the Faraday rotation reaches a constant value with respect to the applied magnetic field. The reason the optical loops in Figure 4.6 do not appear to saturate, but rather monotonically increase beyond approximately 100 G, is because of the paramagnetic nature of the substrate. The paramagnetic contribution from the substrate must be subtracted from the optical hysteresis loops of the sample before the saturation values can be observed. To measure the paramagnetic contribution from the substrate, a blank substrate is inserted in place of the sample and an optical loop is obtained for the blank substrate. The optical loop for a garnet substrate is typically a monotonically increasing linear curve with no coercivity. The loop obtained for the blank substrate can be subtracted from the loop obtained for a sample to produce a corrected optical hysteresis loop that removes the paramagnetic effect due to the substrate. A properly corrected optical hysteresis loop will reveal the saturation behavior of a sample where the Faraday rotation reaches a constant value with

respect to an increase in the applied magnetic field. The magnitude of the applied magnetic field at which the Faraday rotation first reaches saturation is considered the saturation magnetic field.

The Faraday rotation measured during an optical hysteresis loop measurement is in arbitrary units and not degrees. To convert the arbitrary units into degrees and determine the specific Faraday rotation for a sample, the following process is used:

1. A static voltage is applied to the current source so that the applied magnetic field magnitude is equal to the saturation magnetic field measured for the given sample.
2. The voltage equivalent to the intensity of the optical signal is measured on the oscilloscope for the positive polarity of the applied magnetic field.
3. The polarity of the applied magnetic field is flipped (same magnitude as in step 2 but the direction of the applied magnetic field is reversed) and the intensity of the optical signal measured by the detector will change.
4. The analyzer (at a 45° angle with respect to the polarizer) is then rotated until the voltage measured on the oscilloscope returns to the voltage value measured in step 2.
5. The angle by which the analyzer has been rotated in step 4 is measured and equated to twice that of the Faraday rotation of the given sample in degrees.
6. The Faraday rotation is calculated by dividing the angle found in step 5 by two.
7. The specific Faraday rotation (Faraday rotation per unit length) for the sample is calculated by taking the angle found in step 6 and dividing it by the thickness of the sample at the location where the measurement has been taken.

Ferromagnetic Resonance (FMR) Measurements

Ferromagnetic resonance (FMR) is an instance of maximum absorption of energy from a transverse rf field by a ferromagnetic material. The maximum absorption occurs when the frequency of the rf field equals the precession frequency of the magnetization of the material around an applied DC magnetic field. FMR can be used to obtain information about anisotropy fields that control the magnetization direction and magnetization dynamics in thin films.

FMR arises from the precession of the magnetization vector of a ferromagnetic material around the magnetic field lines of an externally applied DC magnetic field. The applied DC magnetic field causes a torque that aligns the magnetic spin moment of the free electrons with the applied field [Gilb04]. This torque can be expressed as

$$\vec{T} = \frac{d\vec{L}}{dt} = \vec{\mu} \times \vec{H} \quad (4.8)$$

where \vec{L} is the angular momentum, $\vec{\mu} = -\gamma\vec{L}$ is the magnetic spin moment, and \vec{H} is the magnetic field. The torque induces the precession of the magnetization vector. The dynamics of the precession of the magnetic spin moment around the magnetic field is described by

$$\frac{d\vec{\mu}}{dt} = -\gamma\vec{\mu} \times \vec{H} \quad (4.9)$$

where $\gamma = \frac{g|e|}{2m_e c}$ is the gyromagnetic ratio. The natural frequency of the precession, known as the Larmor frequency, is

$$f_L = \frac{\gamma H}{2\pi} \Rightarrow \omega = \gamma H. \quad (4.10)$$

The precession of the magnetic spin moment [dAqu04] for each free electron is denoted by a subscript j as follows

$$\frac{d\vec{\mu}_j}{dt} = -\gamma \vec{\mu}_j \times \vec{H}. \quad (4.11)$$

For a spatially uniform magnetic field, \vec{H} , a simple volume average can be taken on the magnetic spin moments of the free electrons over an elementary volume dV_r [dAqu04],

$$\frac{1}{dV_r} \frac{d \sum_j \vec{\mu}_j}{dt} = -\gamma \frac{\sum_j \vec{\mu}_j}{dV_r} \times \vec{H}. \quad (4.12)$$

The magnetization vector, \vec{M} , is defined as the sum of the magnetic spin moments per unit volume as follows

$$\vec{M} = \frac{\sum_j \vec{\mu}_j}{dV_r}. \quad (4.13)$$

By combining Eq. 4.12 and Eq. 4.13, the precession of the magnetization vector can be written as

$$\frac{d\vec{M}}{dt} = -\gamma \vec{M} \times \vec{H}_{eff} \quad (4.14)$$

where \vec{H}_{eff} now takes into account all the magnetic fields that effect the system. \vec{H}_{eff} is defined as

$$\vec{H}_{eff} = \vec{H}_0^{eff} + \vec{h}e^{j\omega t} \quad (4.15)$$

where $\vec{h}e^{j\omega t}$ is the AC component contributed by the rf field and \vec{H}_0^{eff} is the effective DC magnetic field, taking into account the external DC field, the material anisotropy

fields, and the shape anisotropy fields [Zhan04]. Likewise, the magnetization vector can also be written as a sum of a DC term and an AC term

$$\vec{M} = \vec{M}_0 + \vec{m}e^{j\omega t} \quad (4.16)$$

where \vec{M}_0 is the DC component and $\vec{m}e^{j\omega t}$ is the AC component [Zhan04].

The amplitude of the precession is limited, however, by damping, so Eq. 4.14 is modified to include a damping term to form the Landau-Lifshitz equation as follows:

$$\frac{d\vec{M}}{dt} = -\gamma\vec{M} \times \vec{H}_{eff} - \frac{\lambda}{|\vec{M}^2|}\vec{M} \times (\vec{M} \times \vec{H}_{eff}). \quad (4.17)$$

By taking a linear approximation of Eq. 4.17, the damping term can be ignored. Equation 4.17 can be expanded to into its various components:

$$\frac{d\vec{M}}{dt} = -\gamma(\vec{M}_0 \times \vec{H}_0^{eff} + \vec{M}_0 \times \vec{h}e^{j\omega t} + \vec{m}e^{j\omega t} \times \vec{H}_0^{eff} + \vec{m}e^{j\omega t} \times \vec{h}e^{j\omega t}). \quad (4.18)$$

It is assumed that the DC components are much larger than the AC components. Therefore, a small signal approximation can be made for Eq. 4.18 since $h \ll H_0^{eff}$ and $m \ll M_0$ and the term $\vec{m}e^{j\omega t} \times \vec{h}e^{j\omega t}$ can be neglected. The DC components of both the magnetization and magnetic field are parallel to each other so $\vec{M}_0 \times \vec{H}_0^{eff} = 0$. Equation 4.18 can therefore be approximated as

$$\frac{d\vec{M}}{dt} = -\gamma(\vec{M}_0 \times \vec{h}e^{j\omega t} + \vec{m}e^{j\omega t} \times \vec{H}_0^{eff}). \quad (4.19)$$

Since the DC component of the magnetization vector does not change with time,

$$\frac{d\vec{M}}{dt} = j\omega\vec{m}e^{j\omega t}. \quad (4.20)$$

By equating Eq. 4.19 to Eq. 4.20, the following equation is obtained:

$$j\omega\vec{m} = -\gamma(\vec{M}_0 \times \vec{h} + \vec{m} \times \vec{H}_0^{eff}). \quad (4.21)$$

The cross-products in Eq. 4.21 are evaluated and the results can be separated into the x, y, and z components:

$$\begin{vmatrix} \hat{x} & \hat{y} & \hat{z} \\ 0 & 0 & M_0 \\ h_x & h_y & h_z \end{vmatrix} = -h_y M_0 \hat{x} + h_x M_0 \hat{y} + 0 \hat{z}$$

$$\begin{vmatrix} \hat{x} & \hat{y} & \hat{z} \\ m_x & m_y & m_z \\ 0 & 0 & H_0^{eff} \end{vmatrix} = m_y H_0^{eff} \hat{x} - m_x H_0^{eff} \hat{y} + 0 \hat{z} \quad (4.22)$$

$$j\omega m_x = -\gamma(M_0 \times \vec{h} + \vec{m} \times H_0^{eff})_x = \gamma(M_0 h_y - m_y H_0^{eff})$$

$$j\omega m_y = -\gamma(M_0 \times \vec{h} + \vec{m} \times H_0^{eff})_y = \gamma(-M_0 h_x + m_x H_0^{eff})$$

$$j\omega m_z = -\gamma(M_0 \times \vec{h} + \vec{m} \times H_0^{eff})_z = -\gamma(0 + 0) = 0.$$

The components of \vec{m} are therefore:

$$m_x = \frac{\gamma(M_0 h_y - m_y H_0^{eff})}{j\omega}$$

$$m_y = \frac{\gamma(-M_0 h_x + m_x H_0^{eff})}{j\omega} \quad (4.23)$$

$$m_z = 0.$$

The three components of \vec{m} in Eq. 4.23 indicate that the magnetization vector precesses in a circular path about the magnetic field lines. The resonance frequency can

be calculated from Eq. 4.23. For small excitation powers, the resonance frequency of the magnetization precession is given by [BaWa88]:

$$\left(\frac{\omega}{\gamma}\right)^2 = \frac{1}{M^2} \left[\frac{\partial^2 E}{\partial \theta^2} \left(\frac{1}{\sin^2 \theta} \frac{\partial^2 E}{\partial \varphi^2} + \frac{\cos \theta}{\sin \theta} \frac{\partial E}{\partial \theta} \right) - \left(\frac{1}{\sin \theta} \frac{\partial^2 E}{\partial \varphi \partial \theta} - \frac{\cos \theta}{\sin^2 \theta} \frac{\partial E}{\partial \varphi} \right)^2 \right]. \quad (4.24)$$

where E is the free energy density described in Chapter 1. Equation 4.24 can be used to calculate the anisotropy fields.

The schematic for the FMR apparatus is shown in Figure 4.7. A ferromagnetic thin film sample is first placed in the mini box that is made out of a non-magnetic material so that it will not interfere with the measurements. Inside the mini box is an alumina substrate with a gold stripline on it that runs down the center of the mini box. The alumina substrate is used as an insulator to keep the gold conducting strip from being shorted out since the casing of the mini box is grounded. The sample is placed film side down in the mini box in such a way that the area of the sample that touches the stripline is maximized. Tape is applied to the back side of the sample to secure the sample in place and ensure that the sample has strong contact with the stripline.

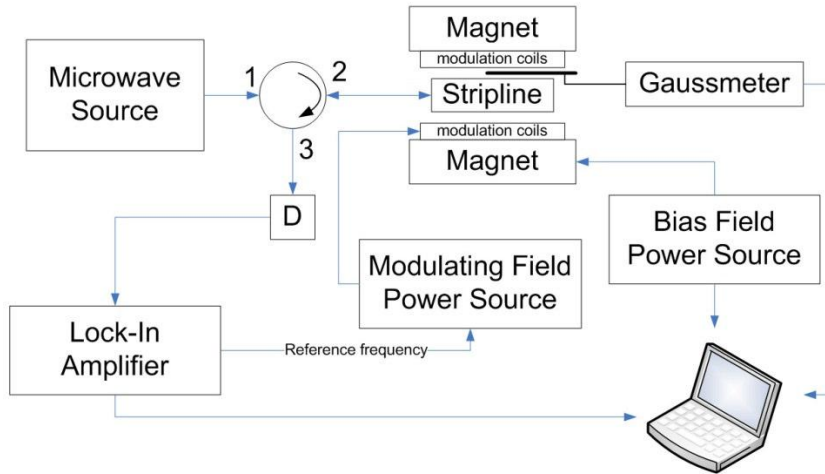


Figure 4.7: Schematic of the FMR system [STka11].

The microwave source generates the rf signal. The frequency of the rf signal is fixed at a value in the range of 4GHz to 7GHz, all in the microwave frequency band. The FMR measurement is performed for a fixed rf frequency in this range and is repeated at different fixed frequencies so that the resonance magnetic field can be determined as a function of the rf frequency.

The rf signal is transmitted down a coaxial cable from the microwave source that is connected to port 1 of the circulator. The rf signal enters port 1 and is redirected out of port 2 of the circulator which is connected to the input of the mini box via another coaxial cable. The rf signal enters the mini box and continues down the stripline inside the mini box. The stripline is shorted at the opposite end of the mini box so that the incident signal is reflected by the short. A small amount of the incident signal will be absorbed by the sample as well, except for at the instance of a resonance.

The reflected signal is directed back to port 2 of the circulator and proceeds to port 3. The reflected rf signal exits port 3 of the circulator which is connected to the diode detector. The diode detector outputs a DC voltage that is proportional to the magnitude of the reflected rf power.

The output from the diode detector is connected to the lock-in amplifier. The lock-in amplifier is used to extract the weak signal from its noisy environment using a phase-lock detection method. To allow the lock-in amplifier to function correctly, the input signal needs to be modulated. The large DC magnetic field is modulated by a small AC magnetic field at a frequency chosen by the user (100 Hz), and the lock-in amplifier is set to detect at that frequency. The AC magnetic field of 1 Oe amplitude is induced in

the modulation coils by the current that is amplified by the modulating field power supply.

The external DC magnetic field is swept over a chosen range so that the full resonance behavior can be observed. When a large decrease in the reflected power is measured, which translates into a large increase in absorbed power (see Figure 4.8), a resonance field is found for the given rf frequency. The output of the lock-in amplifier is proportional to the derivative of the absorption peak.

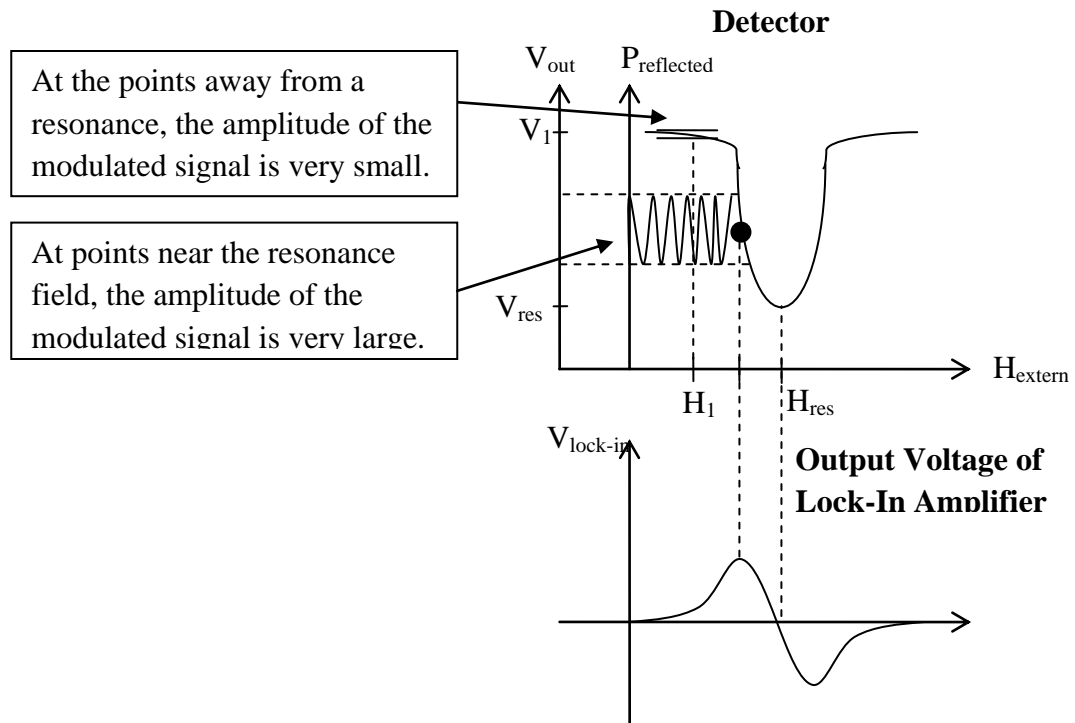


Figure 4.8: Input and Output Signals of the Lock-In Amplifier.

A computer attached to the FMR system collects the output of the lock-in amplifier as well as the measured DC magnetic field at the center of the coils where the mini box is mounted using the gaussmeter. The output of the lock-in amplifier is plotted as a function of the external magnetic field (see Figure 4.9) and the resonance field can

be determined (where the derivative of the absorption peak is zero). The resonance field can be measured for different rf frequencies to calculate the effective field of a sample. The resonance field can also be determined for different orientations of the sample with respect to the external field (see Figure 4.10) and the anisotropy fields can be obtained by numerically fitting the experimental data using Eq. 4.24 for the resonance frequency.

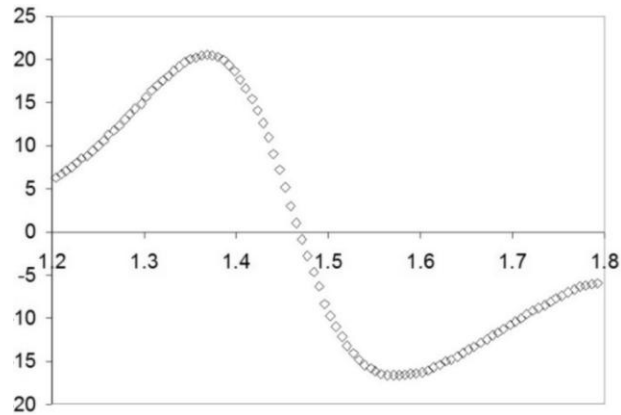


Figure 4.9: Typical signal measured in the FMR experiment. The x axis is the magnitude of the magnetic field in kOe [STka11].

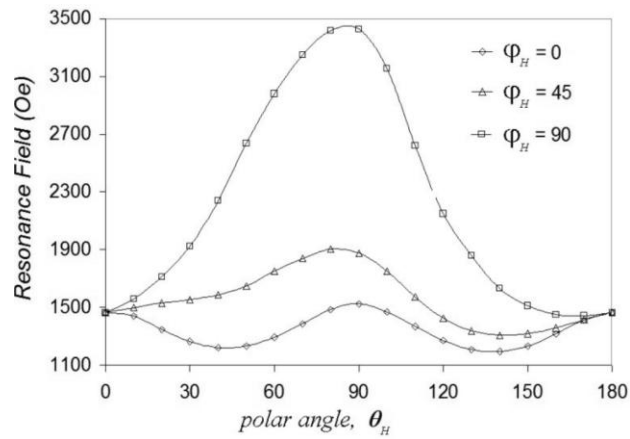


Figure 4.10: Dependence of the ferromagnetic resonance field on the orientation of the sample [STka11].

Optical Domain Imaging

Optical domain imaging is performed using an optical microscope with a polarized light source. The polarized light from the microscope illuminates the sample surface and reflects off a mirror placed underneath the sample. The polarized light interacts with the magnetic domains in the film. The reflected beam propagates through the optical lenses of microscope to a CCD camera that captures images of the domain structures of the film. The thickness of the domain walls can be measured from the captured images. Figure 4.11 shows an optical domain image for a sample with out-of-plane magnetization orientation.

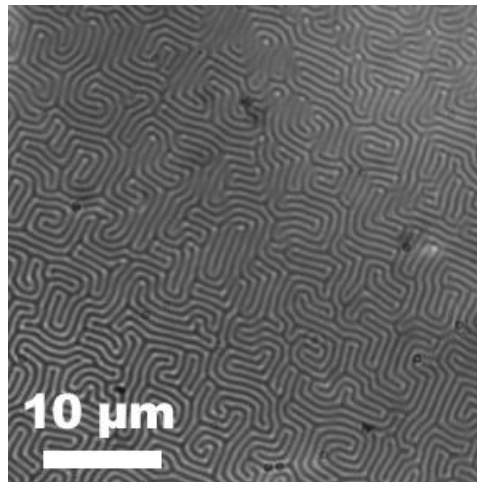


Figure 4.11: Optical domain image obtained for a sample with out-of-plane magnetization orientation.

Development of Improved Faraday Rotation Measurement Techniques

It is difficult to accurately measure small Faraday rotation angles using existing techniques. Mechanical error and signal instability are on the same order of magnitude of the effects being measured in some cases. Two new techniques have been developed to more accurately measure Faraday rotation.

The first technique to measure the Faraday rotation uses a modification of the optical hysteresis loop setup (see Figure 4.12). Rather than mechanically rotating the analyzer to rotate the polarization back to its initial angle and then measuring the relative change in the rotation stage, the analyzer is kept at a fixed position with respect to the polarizer and the Faraday rotation can be calculated directly from the measured intensity. This eliminates mechanical error and allows for time averaging which helps reduce systematic noise.

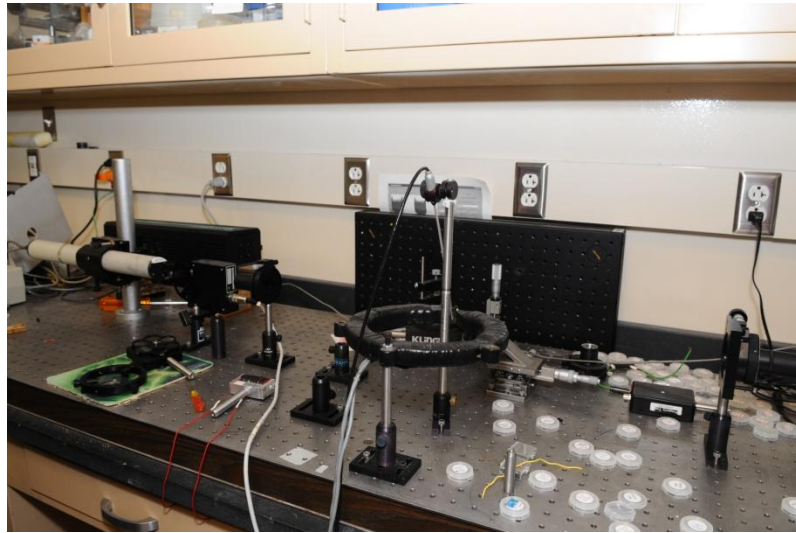


Figure 4.12: Experimental setup for modified optical hysteresis loop and Faraday rotation measurements.

The photo detector which measured output power of the optical radiation has been replaced with a TAOS TSL237 High-Sensitivity Light-to-Frequency Converter that measures light intensity which is independent of the beam spot size. The sensor combines a silicon photodiode and a current-to-frequency converter that outputs a square wave with frequency directly proportional to the light intensity on the photodiode. A

LabView program measures the frequency of the square wave and calculates the intensity of the light.

To calculate the Faraday rotation, a magnetic field is applied to fully saturate the sample and the intensity of the transmitted beam is measured. The polarity of the magnetic field is then flipped and the intensity of the transmitted beam is once again measured. The Faraday rotation angle can then be calculated from these two intensity values as is shown in Eqs. 4.25 to 4.35.

The incident light entering the magneto-optic media is

$$I_{inc} = I_0 \cos^2(\theta_{pol}) + I_{min} \quad (4.25)$$

where I_{min} is the background intensity, I_0 is the intensity of the light prior to entering the polarizer, and θ_{pol} is the incident polarization of the light set by the polarizer. The transmitted light that the detector sees once the light passes through the analyzer is

$$I_{trans} = I_0 \cos^2(\theta_A + \theta_F) + I_{min} \quad (4.26)$$

where θ_A is the angle between the polarizer and the analyzer and θ_F is the Faraday rotation angle. $I_{min} = 0$ because filters are used to block out background intensity.

Using trigonometric identities and small angle approximations for θ_F , $\cos(\theta_A + \theta_F)$ can be simplified.

$$\begin{aligned}
\cos(\theta_A + \theta_F) &= \cos \theta_A \cos \theta_F - \sin \theta_A \sin \theta_F \\
&\approx \cos \theta_A \left(1 - \frac{\theta_F^2}{2}\right) - \theta_F \sin \theta_A \\
&= \cos \theta_A - \frac{\theta_F^2}{2} \cos \theta_A - \theta_F \sin \theta_A \\
&\approx \cos \theta_A - \theta_F \sin \theta_A.
\end{aligned} \tag{4.27}$$

Using Eq. 4.27, $\cos^2(\theta_A + \theta_F)$ can be expanded as such:

$$\begin{aligned}
\cos^2(\theta_A + \theta_F) &= (\cos \theta_A - \theta_F \sin \theta_A)^2 \\
&\approx \cos^2 \theta_A - 2\theta_F \sin \theta_A \cos \theta_A + \theta_F^2 \sin^2 \theta_A \\
&\approx \cos^2 \theta_A - \theta_F \sin 2\theta_A
\end{aligned} \tag{4.28}$$

by dropping out the higher order terms since θ_F is very small. The result of Eq. 4.28 can be plugged back into Eq. 4.26 as follows:

$$I_{trans} = I_0(\cos^2 \theta_A - \theta_F \sin 2\theta_A). \tag{4.29}$$

As previously described, the intensity is measured for a given magnetic field \vec{H}_+ (I_{H+}) and the magnetic field with the same magnitude and opposite polarity \vec{H}_- (I_{H-}) (see Figure 4.13). From these measured intensities, the Faraday rotation angle can be calculated.

$$I_{H+} = I_0(\cos^2 \theta_A - \theta_F \sin 2\theta_A) \tag{4.30}$$

$$I_{H-} = I_0(\cos^2 \theta_A + \theta_F \sin 2\theta_A) \tag{4.31}$$

$$I_{H+} - I_{H-} = -2I_0\theta_F \sin 2\theta_A \tag{4.32}$$

$$I_{H+} + I_{H-} = 2I_0 \cos^2 \theta_A \quad (4.33)$$

$$\begin{aligned} \frac{I_{H+} - I_{H-}}{I_{H+} + I_{H-}} &= \frac{-2I_0\theta_F \sin 2\theta_A}{2I_0 \cos^2 \theta_A} = \frac{-\theta_F \sin 2\theta_A}{\cos^2 \theta_A} = \frac{-2\theta_F \sin \theta_A \cos \theta_A}{\cos^2 \theta_A} \\ &= -2\theta_F \tan \theta_A \end{aligned} \quad (4.34)$$

From Eq. 4.34, θ_F becomes

$$\theta_F = \frac{-1}{2 \tan \theta_A} \frac{I_{H+} - I_{H-}}{I_{H+} + I_{H-}}. \quad (4.35)$$

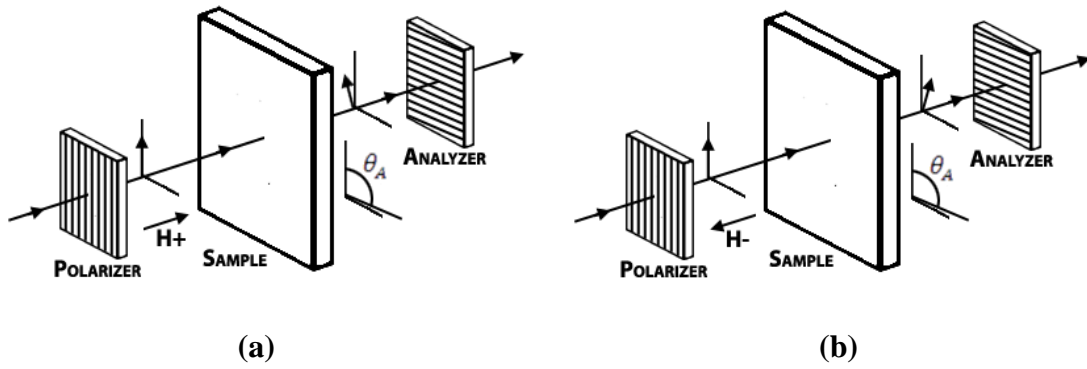


Figure 4.13: Configurations of modified optical hysteresis loop setup for externally applied magnetic field (a) \vec{H}_+ and (b) \vec{H}_- .

Therefore, by knowing θ_A and measuring I_{H+} and I_{H-} , θ_F can be found. The advantage of this technique for small rotation angle measurements is that the sensitivity of the measurement is increased when the angle between the polarizer and analyzer, θ_A , is increased. For example, when θ_A is 45° , the sensitivity is 2. However, when θ_A is 84° , the sensitivity is 19 which is 9.5 times as sensitive.

The second technique to measure Faraday rotation is to use transmission ellipsometry. This technique measures the change in the polarization state of light

transmitted through the surface of a sample. The measured values are expressed as psi (Ψ) and delta (Δ) which are related to the ratio of the Fresnel transmission coefficients, T_p and T_s , as follows:

$$\rho = \frac{T_p}{T_s} = \tan \Psi e^{i\Delta}. \quad (4.36)$$

Since ellipsometry measures the ratio of two values it can be highly accurate and very reproducible. The ratio is also a complex number which contains information about the phase, Δ , making the measurements very sensitive. The calculation of the detector signal will proceed by tracking the polarization state of the light beam through the ellipsometer. The analyzer is a continually rotating polarizer at a known frequency (see Figure 4.14).

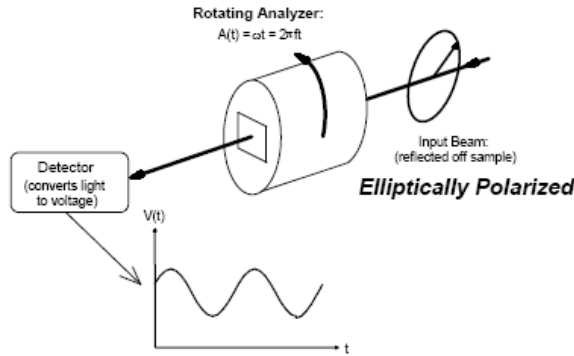


Figure 4.14: The detector signal for an arbitrarily elliptically polarized beam entering the rotating analyzer polarization detector [JAWo10].

Therefore, for general elliptical polarization, the detector signal is a sinusoid with a DC offset of the form:

$$V(t) = DC + a \cos 2\omega t + b \sin 2\omega t. \quad (4.37)$$

The two important quantities measured by the ellipsometer are the normalized Fourier coefficients of the signal, α and β , which can be represented in terms of the Ψ and Δ values for a given sample:

$$\alpha = \frac{a}{DC} = \frac{\tan^2 \Psi - \tan^2 P}{\tan^2 \Psi + \tan^2 P} \quad (4.38)$$

$$\beta = \frac{b}{DC} = \frac{2 \tan \Psi \cos \Delta \tan P}{\tan^2 \Psi + \tan^2 P} \quad (4.39)$$

where P is the input polarizer azimuthal angle with respect to the plane of incidence. The normalized detector signal has the form of a Fourier series in twice the analyzer azimuthal angle:

$$V(t) = 1 + \alpha \cos 2A + \beta \sin 2A \quad (4.40)$$

where the analyzer angle, A , is actually a harmonic function of time, since the analyzer is rotating continuously:

$$A(t) = 2\pi f_0 t + \theta. \quad (4.41)$$

Therefore, if the detector signal is measured as a function of time, a Fourier transform can be performed on the experimentally measured detector signal to obtain the Fourier coefficients α and β of the signal, effectively eliminating the analyzer azimuthal angle, A , as an experimental parameter [JAWo10].

Equations 4.38 and 4.39 can be used to solve for Ψ and Δ from the measured α and β values, and known input polarization, P :

$$\tan \Psi = \sqrt{\frac{1 + \alpha}{1 - \alpha}} |\tan P| \quad (4.42)$$

$$\cos \Delta = \frac{\beta}{\sqrt{1 - \alpha^2}} \cdot \frac{\tan P}{|\tan P|}. \quad (4.43)$$

These two equations form the basis of the ellipsometry measurements performed with a rotating analyzer ellipsometer. By setting the input polarization, P , to 45° , Eq. 4.38 can be simplified to:

$$\alpha = \frac{\tan^2 \Psi - 1}{\tan^2 \Psi + 1} = \frac{\frac{1 - \cos 2\Psi}{1 + \cos 2\Psi} - 1}{\frac{1 - \cos 2\Psi}{1 + \cos 2\Psi} + 1} = \frac{-2 \cos 2\Psi}{2} = -\cos 2\Psi. \quad (4.44)$$

The Faraday rotation angle can be extracted from the measured data. The Fourier coefficient α can be represented as a function of the Faraday rotation angle:

$$\alpha = \sin 2\theta_F. \quad (4.45)$$

Therefore, from Eqs. 4.44 and 4.45, θ_F can be realized from the measured value, Ψ :

$$\alpha = \sin 2\theta_F = -\cos 2\Psi = \sin\left(2\Psi - \frac{\pi}{2}\right) \quad (4.46)$$

which results in the following equation:

$$\theta_F = \Psi - \frac{\pi}{4}. \quad (4.47)$$

The experimental setup used for this technique is shown in Figure 4.15 and Figure 4.16 and uses a J.A. Woollam VASE Ellipsometer in the transmission regime. The

accuracy of the measurements requires careful calibration of the system to determine the absolute position of the polarizer and analyzer. Once the absolute positions of the polarizer and analyzer are determined, the sample is mounted on the sample holder. The permanent magnet holder (see Figure 4.17) is then placed on the translational stage which applies a perpendicular magnetic field to the location of measurement. The magnetic fields have been created by toroidal NdFeB permanent magnets. A gaussmeter is used to determine the magnetic field applied perpendicularly to the sample.

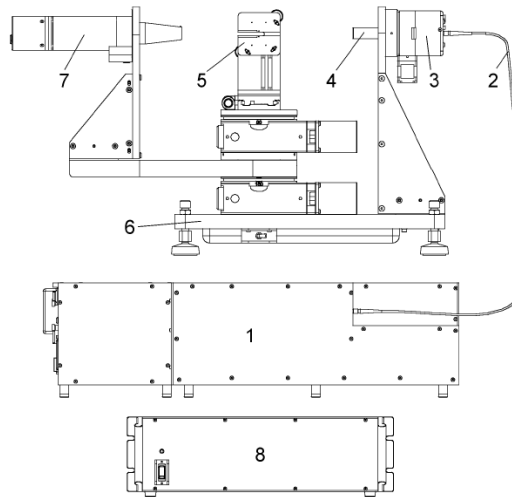


Figure 4.15: Schematic of the J. A. Woollam variable angle spectroscopic ellipsometer (VASE). The components of the system include: (1) monochromator, (2) fiber optic cable, (3) input unit with polarizer, (4) alignment detector, (5) sample stage, (6) goniometer base for automated angle control, (7) detector unit with rotating analyzer and solid state detectors, and (8) motor control box

[JAWo10].

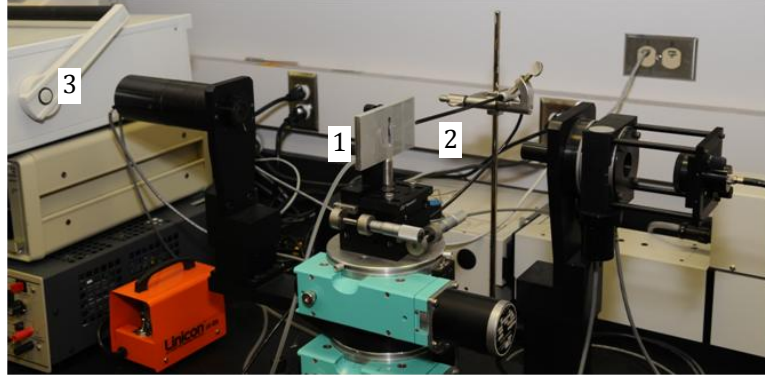


Figure 4.16: Actual experimental setup for ellipsometry-based Faraday rotation measurements. Additional components of the setup include: (1) mount for permanent magnets with slit in the center for light to pass through between the two permanent magnets, (2) gaussmeter probe, and (3) gaussmeter.

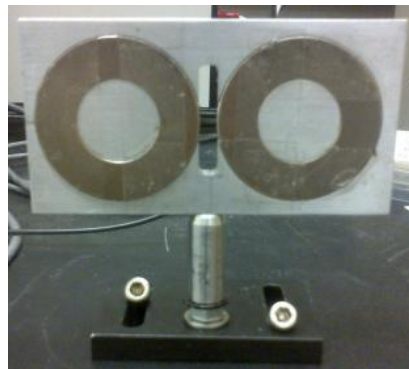


Figure 4.17: Permanent magnet holder with slit in between the two permanent magnets for the light to pass through the gap between the two magnets.

The system is set to take measurements every 5nm in wavelength from 500nm to 800nm with 120 revolutions of the analyzer per step. The entire sweep from 500nm to 800nm is repeated multiple times to allow for averaging to reduce random noise in the measurement results. To calculate the Faraday rotation, 45° , which is the input polarization, is subtracted from the measured output polarization, Ψ .

The two improved Faraday rotation measurement techniques allow for highly sensitive measurements of small amounts of Faraday rotation. This means that sub-micron thick samples can be characterized with better accuracy.

Chapter 5: Development of Garnet Films Utilizing Plasmon Resonances for Faraday Rotation Enhancement

In-Plane Garnet Films with Embedded Gold Nanoparticles and Faraday Rotation Enhancement

Numerical modeling has suggested that the extent of penetration of plasmon resonance induced electric fields is greatest when the metallic nanoparticles are embedded in the garnet films rather than on the film surface. Due to difficulties associated with milling garnet material, ion beam milling followed by deposition of gold could not be used to embed gold nanoparticles in the garnet films. Another way to embed gold nanoparticles in LPE grown garnet films is to form the gold nanoparticles on the garnet substrate and grow the film over the nanoparticles, trapping the nanoparticles between the garnet film and substrate.

Electron beam lithography has been considered for the formation of gold nanopillars on the substrate surface but this technique is very time consuming to cover a 1cm^2 substrate. The chosen method used for the formation of gold nanoparticles is deposition of thin nanolayers of gold using the evaporation technique on the substrate surface followed by annealing in air to form nanoparticles.

Once the nanoparticles are formed on the substrate surfaces, garnet films are grown over the nanoparticles using LPE, effectively embedding the nanoparticles in the garnet films. It is not natural for garnet to grow over metal since the LPE growth process depends on mimicking of the crystallographic structure of the substrate. Therefore, there

is no guarantee that the nanoparticles will survive the LPE growth process or that garnet can even be grown over metallic nanoparticles.

Since gold is not soluble in the garnet melt, there is no need to worry about the gold nanoparticles being incorporated in the melt during the LPE growth process. The only concern is that the garnet film will not grow over the gold nanoparticles. Experimental work by [Fuji08, Uchi09] used the rf-sputtering technique to deposit garnet over gold nanoparticles but there has been no prior evidence that anyone has embedded metallic nanoparticles in garnet films using liquid phase epitaxy.

To form the gold nanoparticles, thin layers of gold (about 5-10nm) are deposited on the garnet substrates using the evaporation technique. The substrates with the thin gold layer are then annealed in air at temperatures varying from 700°C to 900°C for 30 minutes [Fuji08, Uchi09]. The annealing process results in the formation of hemispherical nanoparticles on the surface of the garnet substrates. The determined shape of the nanoparticles is supported by AFM images of the nanoparticles on the substrate surfaces and numerical modeling. Depending on the temperature of the annealing process and the thickness of the gold layer, the segregation of the particles and the average size of the particles vary, but the shape remains relatively constant.

(100)-oriented SGGG substrates have been masked with a tape that leaves behind no residue on the substrate surfaces. The tape is used to create a checkerboard pattern so that when the gold is deposited on the substrates, only two quadrants have the gold deposited on them while the other two quadrants are without gold (see Figure 5.1).



Figure 5.1: Schematic of substrates with gold deposited on them.

The checkerboard pattern allows for the comparison of measurements in the adjacent regions with and without gold on the same sample which helps eliminate ambiguities due to thickness of the epitaxial films grown over the gold nanoparticles. Therefore, any changes to the properties of the films can be attributed to the presence of the embedded gold nanoparticles.

Several substrates have been prepared with gold layers of approximately 5nm in thickness deposited on them in the checkerboard pattern. These substrates have been later annealed in air at 830°C. The diameter of the particles varied from 10 to 250nm with the average being about 100nm and the height being about 0.4 to 0.5 times that of the diameter. After the substrates with gold have been annealed, they are characterized using atomic force microscopy, transmission measurements and x-ray diffraction. It is very important to confirm the presence and formation of the gold nanoparticles, and characterize their geometry and size before the film is grown over the nanoparticles.

Atomic force microscopy measurements have been performed on the substrates to verify the presence of the gold nanoparticles on the surfaces, and to measure the geometry, size and distribution of the nanoparticles (see Figure 5.2).

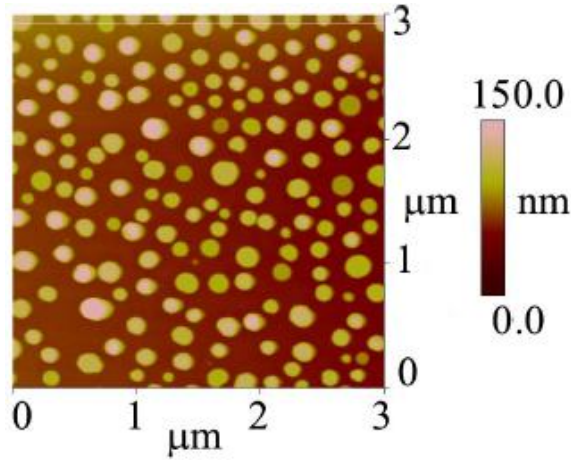


Figure 5.2: Atomic Force Microscopy image of gold nanoparticles formed on garnet substrate.

Light transmission experiments have also been performed to further verify the presence of the gold nanoparticles and demonstrate the excitation of plasmon resonances in the nanoparticles (see Figure 5.3). The difference in the transmission coefficient curves shown in the inset of Figure 5.3 can be attributed to the absorption of light energy caused by plasmon resonances excited in the gold nanoparticles. The difference curve shows that the resonance wavelength is approximately 600nm which is consistent with the theoretical simulations presented in Chapter 3. The sharpness of the difference curve implies that the nanoparticles are resonating at practically the same wavelength which suggests that the nanoparticles are self-similar.

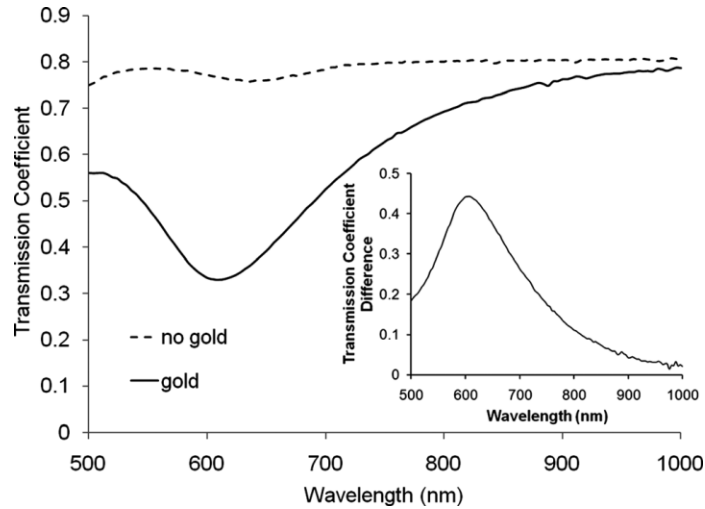


Figure 5.3: Transmission coefficients of the garnet substrates with and without gold nanoparticles [Tkac11].

In addition, X-Ray diffraction measurements have been performed to measure the gold peak of the nanoparticles on the substrate surface prior to LPE film growth.

After the characterization of the gold nanoparticles is complete, the substrates are mounted in the substrate holder and the liquid phase epitaxy technique is used for film growth as described in Chapter 2. Films with in-plane magnetization orientation have been grown from a melt with composition of $(\text{Bi, Pr, Y, Gd})_3(\text{Fe, Ga})_5\text{O}_{12}$. The G/F ratio has been decreased over two iterations of the melt design to lower the growth rate of the melt (see Table 5.1). Melt UMD210 has been used to grow the films for this experiment. After the film growth, the samples are further characterized to verify the presence of the gold nanoparticles embedded in the film.

	G/F	C _{Bi}	C _B	R ₁	Fe/Ga	Gd/Y	Pr/Y
UMD209	0.16	0.47	0.16	16.50	4.50	0.20	0.40
UMD210	0.15	0.44	0.14	16.50	4.50	0.20	0.40

Table 5.1: Cation ratios of the melt designs used to produce films with in-plane magnetization orientation with a film composition of (Bi, Pr, Y, Gd)₃(Fe, Ga)₅O₁₂.

X-ray diffraction measurements have been performed to measure the gold peak and compare its angle to the measurements taken before the film growth (see Figure 5.4). The measurements clearly reveal the presence of the gold (111) peak near 19.1° prior to the LPE film growth and near 19.2° after the LPE film growth. This suggests that the gold nanoparticles did in fact survive the LPE growth process in some crystalline form but it is uncertain if the nanoparticles maintained their shape and mutual separations. The difference of 0.1° between the two measured peaks prior to and after the LPE film growth is significant and suggests that the film could be experiencing some sort of stress due to the presence of the gold nanoparticles embedded in the epitaxial film.

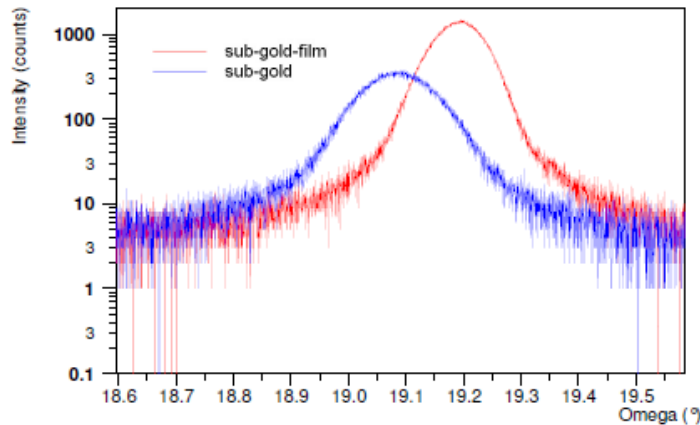


Figure 5.4: X-ray Diffraction Peaks for the gold (111) reflection seen both before and after LPE film growth over substrates populated with gold nanoparticles.

Transmission measurements have also been taken after LPE film growth in the regions with and without gold to compare the transmission coefficients due to the presence of gold after the film growth (see Figure 5.5). The transmission coefficient measurements have been taken for adjacent points on either side of the boundary between the regions with gold and without gold. Subtracting the two curves reveals the effect due to the excitation of plasmon resonances in the embedded gold nanoparticles (shown in the inset of Figure 5.5).

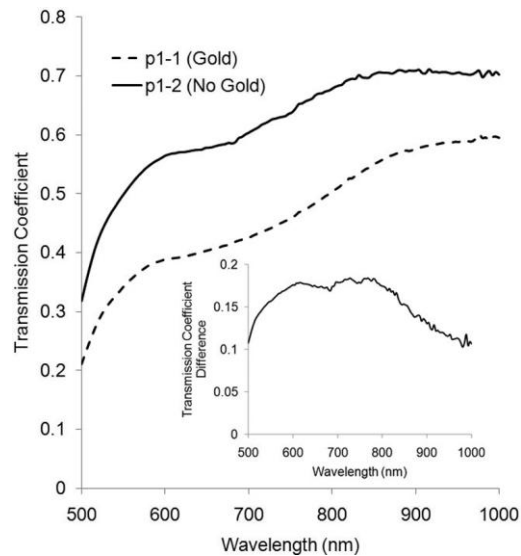


Figure 5.5: The results of the transmission coefficient measurement for two adjacent points on either side of the boundary between garnet with and without embedded gold nanoparticles. The inset shows the difference between the two transmission measurements which reveals the absorption due to the plasmon resonances in gold nanoparticles [Tkac11].

The curve for the transmission coefficient difference is much different for the measurements taken after the LPE film growth than those taken before the LPE film growth. The resonance curves have become much broader which could be caused by modification of the shape and mutual spacing between the nanoparticles embedded in the

garnet film. This suggests that after the LPE growth process, the nanoparticles are no longer self-similar and their plasmon resonances are being excited at different resonance wavelengths. If this is the case, the broad plasmon resonances could actually be beneficial because they would allow for Faraday rotation enhancement in a wide wavelength range.

Once the presence of the gold nanoparticles embedded in the garnet films is confirmed, the properties of the samples are measured. Measurements of properties such as thickness, specific Faraday rotation, FMR, transmission, saturation magnetic field, and domain sizes have been made on either side of the boundary between gold and no gold (see Figure 5.6). This allows for the quantification of the effects the gold has on the results without any ambiguities due to such variables as local film thickness.

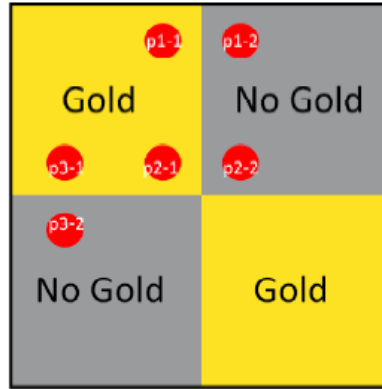


Figure 5.6: Diagram of the checkerboard pattern of a sample with three sets of adjacent points at which measurements have been taken for comparison purposes.

The Faraday rotation measurements have been conducted using 532nm and 633nm wavelength frequency stabilized lasers. The lasers are not, however, intensity stabilized which makes it difficult to accurately measure very small angles of Faraday rotation. To avoid error in the Faraday rotation measurements, the raw intensity values

are used to compare adjacent points rather than the specific Faraday rotation measurements that are more prone to error due to the small angles of rotation and the accuracy of the rotation stage of the analyzer. By scaling the intensities of the optical measurements taken in the gold and no gold regions, the Faraday rotation can be compared.

Figure 5.7 shows two optical loops measured at adjacent points on either side of the boundary between gold and no gold regions for one of the in-plane samples with Faraday rotation in arbitrary units. Faraday rotation is negative for the in-plane samples which is why the optical loops appear to be inverted. Due to the paramagnetic contribution from the substrates, the loops appeared to monotonically decrease in the saturation region. Therefore, the saturation values for the Faraday rotation are the maximum peak values. Comparing the two values for the particular sample shown in Figure 5.6, an enhancement of 8.4% has been calculated. Similar enhancement factors have been calculated for other pairs of adjacent points on this sample (see Table 5.2).

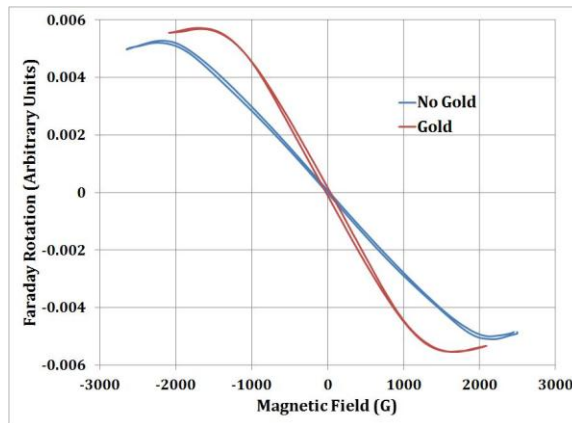


Figure 5.7: Optical hysteresis loop comparison for two adjacent points on either side of the gold/no gold boundary.

	Faraday Rotation Enhancement @ 633nm	Faraday Rotation Enhancement @ 532nm
p1-1 (Gold) vs p1-2 (No Gold)	9.2%	9.0%
p2-1 (Gold) vs p2-2 (No Gold)	8.4%	9.9%
p3-1 (Gold) vs p3-2 (No Gold)	8.8%	11.1%

Table 5.2: Faraday rotation enhancement measurements for sample with in-plane magnetization orientation.

Anisotropy Study of Out-of-Plane Garnet Films with Embedded Gold Nanoparticles

Due to the large magnetic fields required to saturate the in-plane samples, there is interest in growing samples with out-of-plane magnetization that saturate at smaller magnetic fields. A new melt has been engineered with the following composition: $(\text{Bi, Gd, Lu})_3(\text{Fe, Ga})_5\text{O}_{12}$. Extra efforts have been made to attempt to grow films below 300nm in thickness. To decrease the growth rate of the out-of-plane samples, the G/F ratio of the melt has been decreased over several iterations of the melt design to achieve a desired growth rate (see Table 5.3).

	G/F	C _{Bi}	C _B	R ₁	Fe/Ga	Gd/Lu
UMD300	0.17	0.45	0.14	19.01	4.50	7.01
UMD301	0.16	0.45	0.15	19.02	4.50	7.01
UMD302	0.15	0.45	0.15	19.02	4.50	7.01

Table 5.3: Cation ratios of the melt designs used to produce films with out-of-plane magnetization orientation with a film composition of $(\text{Bi, Gd, Lu})_3(\text{Fe, Ga})_5\text{O}_{12}$.

Four (100)-oriented SGGG substrates have been masked in the checkerboard pattern and thin layers of gold, about 7nm, have been deposited on the substrates using evaporation. One of the substrates with gold has been annealed at 700°C, one has been

annealed at 800°C, one has been annealed at 900°C and one has not been annealed. After annealing the samples, measurement techniques such as AFM, transmission, and XRD have been used to characterize the substrates and the gold nanoparticles. An AFM image of one of the substrates is shown in Figure 5.8. For this particular sample annealed at 900°C, the nanoparticles have an average height of about 35nm and diameters around 70nm.

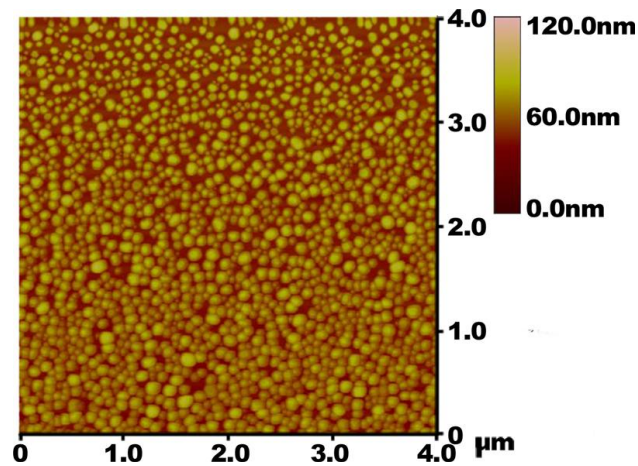


Figure 5.8: Atomic Force Micrograph of gold nanoparticles formed on SGGG substrate by annealing at 900°C [Lang12].

Transmission coefficient measurements for the four substrates are shown in Figure 5.9. The transmission coefficient measurements reveal that the annealing temperature does not affect the shape of the gold nanoparticles because the minimums are at roughly the same wavelength regardless of the annealing temperature. This means that the nanoparticles are self-similar and that only the mutual separation between particles and particle size vary with the annealing temperature. For the substrate with the gold unannealed, the transmission curve is much broader (see Figure 5.9), most likely due to plasmon resonances being excited at multiple resonance wavelengths.

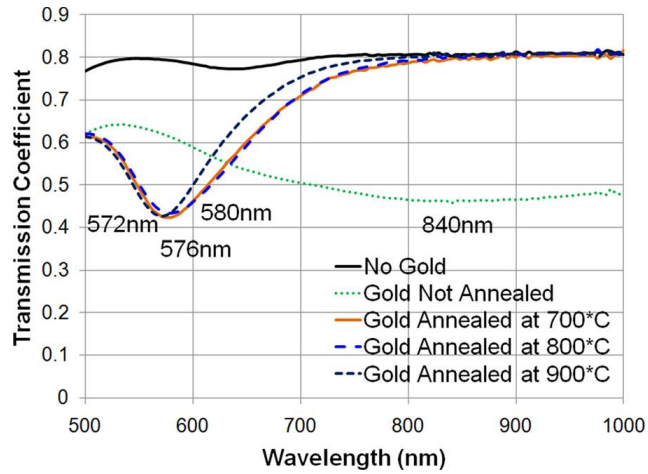


Figure 5.9: Transmission coefficient measurements of SGGG substrates with gold (unannealed, and annealed at 700°C, 800°C, and 900°C) and without gold [Lang12].

After complete characterization of the gold nanoparticles, garnet films have been grown over the four substrates using liquid phase epitaxy from melt UMD302 which has a saturation temperature of 813°C. The films have been grown at 772°C, a 41°C undercooling, with rotation rate of 49rpm and a growth time of approximately 15 seconds. The film thicknesses, growth temperatures, growth rates, and other growth parameters for the four samples are summarized in Table 5.4.

	Annealing Temp.	Film Thickness	Growth Temp.	Rotation Rate	Growth Time	Growth Rate
UMD302-281	800°C	0.31µm	771.1°C	49rpm	16s	1.17 µm/min
UMD302-283	900°C	0.26µm	771.6°C	49rpm	15s	1.04 µm/min
UMD302-284	700°C	0.28µm	771.9°C	49rpm	16s	1.04 µm/min
UMD302-285	--	0.26µm	772.8°C	49rpm	17s	0.92 µm/min

Table 5.4: Growth conditions and film thickness values for the four samples grown from melt UMD302 with out-of-plane magnetization orientation.

Looking at the out-of-plane samples under the microscope has revealed an appreciable difference in the magnetic domain structure in the gold and no gold regions of the samples (see Figure 5.10). This discovery has led to a further investigation of the effect that the embedded gold nanoparticles has on the magnetic properties of the garnet films. It is possible that the gold nanoparticles may have an effect on the epitaxial growth process, which in turn may result in different anisotropy properties of the garnet films. The anisotropies of garnet films grown by using liquid phase epitaxy are important parameters of the films because these parameters determine the magnetic properties of the films.

It is well known that garnet films with out-of-plane magnetization orientation exhibit a serpentine domain structure, the structure of which depends on the magnetic properties of garnet films [Lang12]. The optical domain images in Figure 5.10 clearly suggest that the magnetic properties of the epitaxially grown garnet films are different in the two adjacent regions with and without gold. The domain structure in the region without gold (see Figure 5.10(a)) is typical of out-of-plane magnetized garnets. The domain structure in the region with gold (see Figure 5.10(b)), however, has a smaller domain period and the pattern is more irregular, possibly due to a stress-induced anisotropy from the presence of the gold nanoparticles embedded in that region [Lang12].

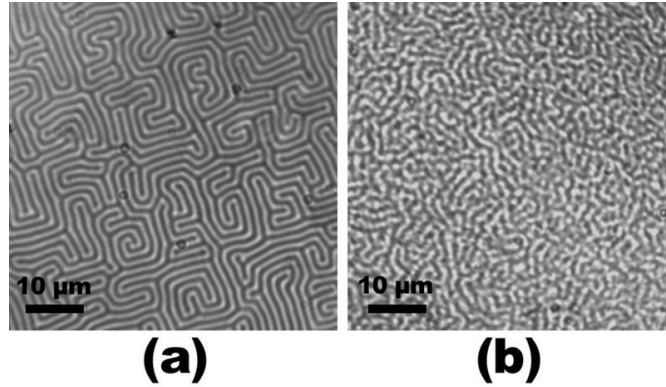


Figure 5.10: Optical domain images for (BiGdLu) garnet film in regions (a) without and (b) with embedded gold nanoparticles [Lang12].

FMR measurements have also been taken for the in-plane magnetized samples and the out-of-plane magnetized samples. The FMR results for the in-plane samples reveal that the effective anisotropy fields for the gold and no gold regions are substantially different (see Figure 5.11). The difference in the effective anisotropy fields suggests that there could be a difference in the uniaxial anisotropy of the garnet films in the gold and no gold regions of the samples. It can be further observed that the saturation fields seen in Figure 5.7 are very close to the effective anisotropy fields seen in Figure 5.11. This implies that there is consistency between the optical hysteresis loop measurements and the FMR measurements for the in-plane samples.

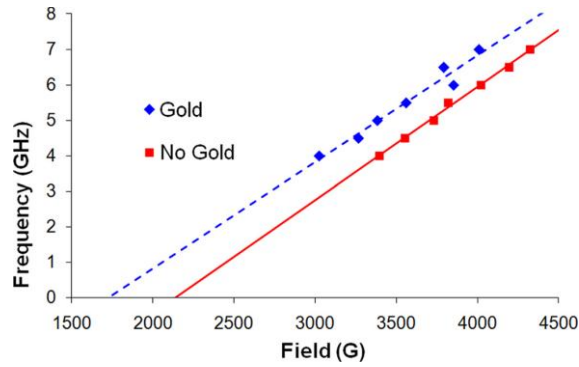


Figure 5.11: Ferromagnetic resonance frequency vs resonance field for (BiPrYGd) in-plane garnet sample regions with and without embedded gold nanoparticles [Lang12].

The FMR results for the out-of-plane measurements are also indicative of substantial differences between the gold and no gold regions. The FMR spectra shown in Figure 5.12 reveals two resonances in the region with gold nanoparticles embedded in the garnet film. The two ferromagnetic resonances in the region with gold are believed to be due to a difference in the effective anisotropy over the film thickness. The results suggest that near the interface with the gold nanoparticles, the film has a different effective anisotropy from that which is further away from the gold nanoparticles since the first resonance peak in the regions with gold is only observed in the gold region and the second resonance peak observed at the higher magnetic field value occurs at the same resonance field as the resonance peak observed in the regions without gold. This conclusion is supported by FMR results observed for multilayer films [NiHo06].

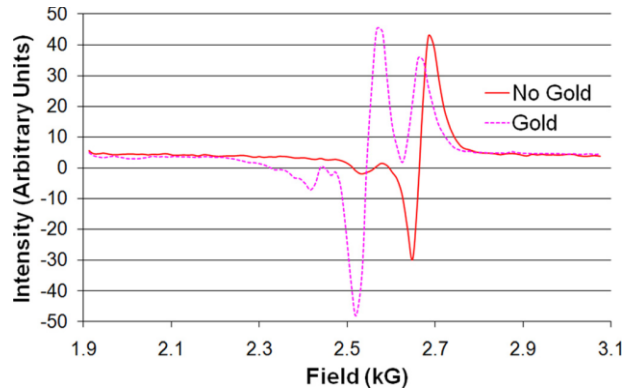


Figure 5.12: Ferromagnetic resonance spectra at 7 GHz for (BiGdLu) garnet showing response for regions with gold (dashed) and without gold (solid) embedded nanoparticles [Lang12].

Optical hysteresis loop measurements for the out-of-plane samples are also supportive of differences in the anisotropy of the films in the regions with and without embedded gold nanoparticles (see Figure 5.13). There is a noticeable broadening of the optical loops measured for the regions with gold that has not been observed in the regions without gold. The broadening of the optical loops can be attributed to an increase in the anisotropy in the regions with gold [Lang12].

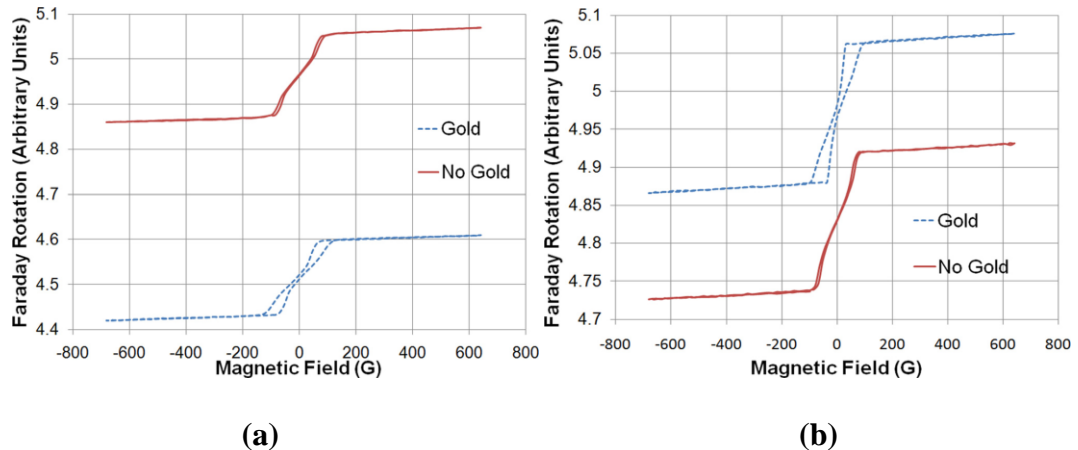
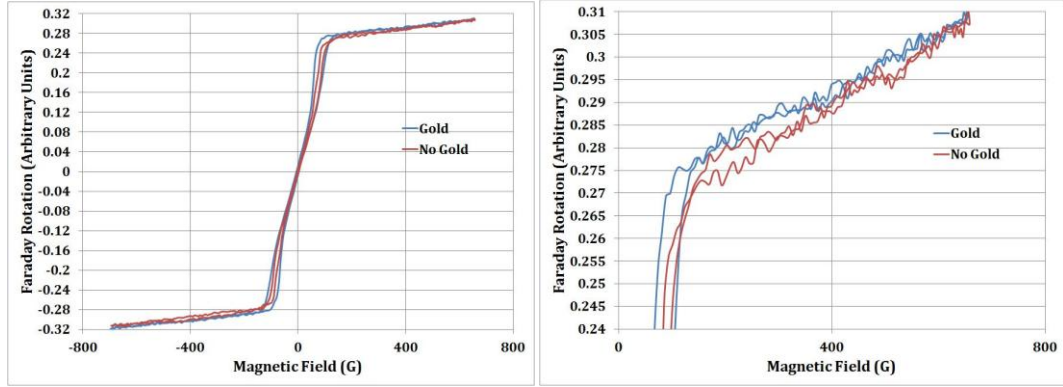


Figure 5.13: Optical hysteresis loops for (a) 900°C annealed out-of-plane garnet with and without embedded gold nanoparticles and (b) unannealed out-of-plane garnet with and without embedded gold nanoparticles [Lang12].

Based on the experimental results from the optical domain imaging, FMR measurements and optical hysteresis loop measurements, it is clear that there are different magnetic properties of the epitaxially grown garnet films in adjacent regions with and without embedded gold nanoparticles. The differences in the magnetic properties can be attributed to the presence of the embedded gold nanoparticles since these differences have been observed on the same garnet films in adjacent regions. These differences in the magnetic properties are most likely due to the effects that the gold nanoparticles have on the growth conditions of the garnet films grown over the nanoparticles using LPE. The embedding of nanoparticles in garnet films could be practically utilized to control localized anisotropy of the films.

The optical hysteresis loops measured for the out-of-plane samples have been used to calculate the Faraday rotation enhancement for the out-of-plane samples. To compare the optical hysteresis loops, the loops are scaled to account for differences in the optical intensity. Once scaled, the loops are shifted to the origin which reveals the Faraday rotation in arbitrary units as a function of the applied magnetic field. If the local thickness is not the same for all locations being measured, the loops have to then be scaled by the local thickness. An example of two optical loops measured for two adjacent points on the same sample is shown in Figure 5.14(a). The thicknesses of the two adjacent points measured in this example are the same and the film compositions are the same as well since they are measured on the same sample. The Faraday rotation enhancement for this particular sample is 2.6%. Enhancement factors for all four out-of-plane samples are summarized in Table 5.5.



(a)

(b)

Figure 5.14: (a) Optical hysteresis loop measurements for a sample with out-of-plane magnetization orientation. (b) An enlarged image of the upper saturation region of the loops shown in (a).

	Faraday Rotation Enhancement @ 633nm
Sample with Gold Annealed at 700°C	-5.1%
Sample with Gold Annealed at 800°C	2.6%
Sample with Gold Annealed at 900°C	-2.6%
Sample with Gold Unannealed	7.0%

Table 5.5: Faraday rotation enhancement measurements for sample with out-of-plane magnetization orientation measured with a red laser with wavelength of 633 nm.

The Faraday rotation enhancement data for the out-of-plane samples do not indicate much enhancement, if any at all, and in some cases the rotation is actually lower in the regions with gold. It has been determined that the error in the measurements is on the same order of magnitude as the Faraday rotation enhancements being measured.

While it is unclear why little or no enhancements have been observed, it is believed that the film thickness is too large in comparison to the size of the embedded nanoparticles to notice any significant change. The size of the nanoparticles formed on

the substrates before LPE film growth for the out-of-plane samples are half the size of the nanoparticles formed on the substrates which the in-plane films have been grown over. The size of the particles affects the extent of penetration of the plasmon resonance induced electric fields so it is possible that the electric fields penetrate a larger percentage of the overall thickness of the in-plane films than the out-of-plane films since the in-plane films are not much thicker than the out-of-plane films.

It is also believed that the laser measurements are off-resonance which means that the plasmon resonances in the embedded nanoparticles have not been optimally excited during the optical hysteresis loop measurements. The measurement technique used to measure the optical hysteresis loops has a measurement error of about 5% so this could explain the small negative enhancement values that have been calculated. There is a lot of noise in the optical hysteresis loop measurements and the sensitivity of the measurements may not be enough to accurately measure small changes in rotation. The thickness measurements and the optical hysteresis loop measurements are not performed at the same time so there could also be error in the location on the samples at which the measurements are taken. If the thickness measurements are not taken at the same locations on a sample as the optical hysteresis loop measurements and the sample has non-uniform thickness, then this could greatly affect the accuracy of the enhancement measurements.

Development of Sub-Micron Thick Out-of-Plane Garnet Films Using LPE

It is a difficult task to grow sub-micron thick garnet films using LPE due to restricting growth conditions. Garnet films in the range of 100-200nm in thickness are necessary to achieve uniform distribution of the plasmon resonance induced electric

fields over the thickness of the films. This requirement is supported by numerical calculations that showed that the extent of penetration of the induced electric fields has been around 1 to 2 times the height of the nanoparticles.

The growth of thinner films requires the melt composition and growth conditions to be altered to slow down the growth rate of the films. The slower growth rates also aid in the growth of better quality films because the films can be grown for longer periods of time at stable growth conditions. To maximize the spread of the plasmon resonance electric field, the garnet film must be less than twice the height of the embedded gold nanoparticles. That amounts to a film thickness of 100-200nm.

The growth rate has been previously reduced by lowering the G/F ratio of the melt composition and lowering the rotation rate of the substrate during growth. A decrease in the rotation rate is counter-productive to the growth of high quality films since it can cause non-uniformity of the film composition. Therefore, the rotation rate has been kept constant while changes to the undercooling and G/F ratios have been utilized instead to reach the necessary growth rates.

Modifications have been made to the melt composition to assist in the lowering of the growth rate of the melt. The G/F ratio has already been lowered to the lower limit required to still achieve garnet growth instead of another phase from the melt. Since the growth rate is proportional to both the concentration of garnet constituents and the undercooling, a decrease of the undercooling has been attempted but has resulted in a large lattice mismatch due to a decrease in the bismuth incorporation in the films.

As a result, a new melt has been designed to allow for film growth at lower undercooling. With the decreased bismuth concentration, the lattice parameter of the film cannot match that of the SGGG substrates so GGG substrates have been used instead. In order to match the lattice parameter of GGG, the melt concentration of lutetium has to be larger than that of gadolinium since lutetium is a smaller element than gadolinium. Modeling has been used to calculate the expected film lattice parameter given the melt composition to help ensure that the lattice parameter of the films will closely match the GGG substrates. The cation ratios for the iterations of the melt designs used to produce sub-micron thick films are shown in Table 5.6. Several samples have been grown from melt UMD311 on (111)-oriented GGG substrates to help characterize the melt and determine the ideal growth conditions. It turns out that saturation temperature has been significantly lowered with the new melt composition, UMD311, in comparison to melt UMD302 that has been previous used to produce out-of-plane films (see Figure 5.15).

	G/F	C_{Bi}	C_B	R₁	Fe/Ga	Gd/Lu
UMD310	0.12	0.45	0.15	18.99	4.50	0.34
UMD311	0.13	0.45	0.15	19.02	4.50	0.33

Table 5.6: Cation ratios of the melt designs used to produce sub-micron thick films with out-of-plane magnetization orientation with a film composition of (Bi, Gd, Lu)₃(Fe, Ga)₅O₁₂.

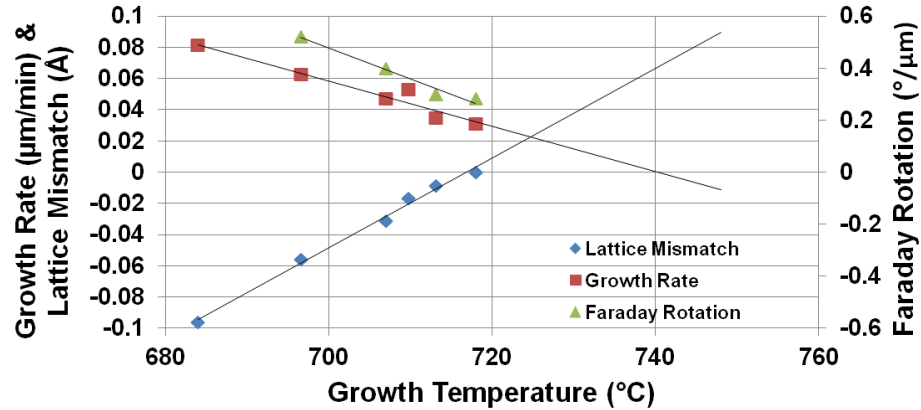


Figure 5.15: Along the left axis are the data points for the growth rate versus growth temperature (squares) and lattice mismatch versus growth temperature (diamonds), and along the right axis are the data points for the Faraday rotation per unit length versus growth temperature (triangles) for the samples produced from the new melt design.

X-Ray diffraction measurements indicate that there is a close lattice match between the films and substrates at a growth temperature of approximately 718°C and resulting growth rate of approximately 0.031 µm/min (see Figure 5.15). At these growth conditions, film thickness of approximately 200nm can be achieved when samples are grown for 7 minutes, resulting in films with the following composition: $\{\text{Bi}_{0.73}\text{Gd}_{0.91}\text{Lu}_{1.36}\}[\text{Fe}_{1.87}\text{Ga}_{0.13}](\text{Fe}_{1.8}\text{Ga}_{1.2})\text{O}_{12}$.

Experimental results indicate that the overall Faraday rotation per unit length and the bismuth concentration both decrease with a reduction in the growth rate (see Figure 5.16). This confirms that bismuth has the largest contribution to the overall Faraday rotation.

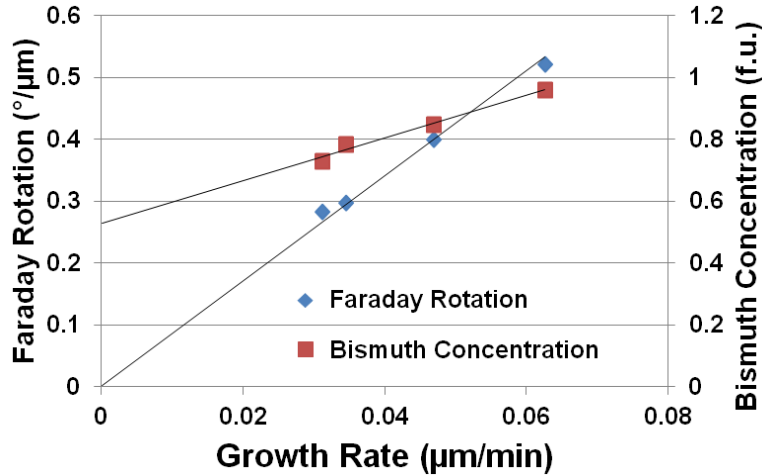


Figure 5.16: Along the left axis are the data points for the Faraday rotation per unit length as a function of the growth rate (diamonds) and along the right axis are the data points for the bismuth concentration as a function of the growth rate (squares) for the new melt design.

The optimized growth conditions have resulted in the production of high quality sub-micron thick films. However, the incorporation of gold nanoparticles in the garnet films has not been successful at these growth conditions. It has been discovered that at the 0.031 $\mu\text{m}/\text{min}$ growth rate, the gold nanoparticles annealed on the substrate prior to film growth do not survive the LPE growth process. Noticeable inclusions of the gold nanoparticles in the corners of the film where the nanoparticles have been formed suggest that the nanoparticles have been “washed off” during the rotation of substrate in the meniscus of the melt. Through trial and error, it has been determined that a growth rate of approximately 0.07 $\mu\text{m}/\text{min}$ is required to achieve the incorporation of embedded nanoparticles at the garnet film/garnet substrate interface. The only plausible explanations are that the incorporation of gold is not trivial and that there is a minimum growth rate necessary to “trap” the gold nanoparticles in the garnet films grown using the

LPE technique. This supports the original notion that the incorporation of gold is not favored by the LPE growth of garnet films.

Incorporation of Gold Nanoparticles on the Surface of LPE Grown Garnet Films and Faraday Rotation Enhancement

The growth of garnet films with thickness below 200nm is of higher importance to the study of Faraday rotation enhancement than the incorporation of the gold nanoparticles in the garnet films. Therefore, efforts have been focused on growing the garnet films without gold nanoparticles embedded in the films. The nanoparticles have instead been formed on the surface of the garnet films. This is advantageous to the study of Faraday rotation enhancement because by evaporating thin layers of various thicknesses of gold on the garnet film surfaces and then annealing the samples at various temperatures, assemblies of nanoparticles of various dimensions and separations can be achieved. When the nanoparticles are embedded in the garnet films, there is no certainty of the shape or relative proximity of the nanoparticles after LPE film growth over the nanoparticles, just that the nanoparticles survive the LPE growth process in some crystalline form.

It has been shown in the numerical modeling in Chapter 3 (see Figure 3.6) that the extent of penetration of the plasmon resonance induced electric fields into the garnet films depends on the dimensions and separation of the gold nanoparticles. This has opened the opportunity to better understand the mechanism by which the Faraday rotation enhancement occurs as well as control the Faraday rotation enhancement by inducing plasmon resonances in gold nanoparticles obtained through annealing gold nanolayers of various thicknesses.

Twelve films of approximately 200nm in thickness have been grown on (111)-oriented GGG substrates with the same film composition mentioned in the previous section. Thin nanolayers of gold of various thicknesses have been deposited on the film surfaces (5nm, 7.5nm, 10nm, and 15nm). Each thickness of gold has been deposited on portions of three samples. Each of the three samples with the same thickness of the gold nanolayer have been annealed in air for 30 minutes at a different temperature (700°C, 800°C, or 1000°C), resulting in assemblies of gold nanoparticles with different dimensions and separations. AFM images of the nanoparticles formed on the samples annealed at 700°C, 800°C, and 1000°C are shown in Figure 5.17, Figure 5.19, and Figure 5.21 respectively. Calculated ratios of the nanoparticle radius-to-height (R/H), nanoparticle radius-to-separation (R/S) and nanoparticle height to sample film thickness (H/F) are shown in Figure 5.18, Figure 5.20, and Figure 5.22 for the three different annealing temperatures. The data displayed in Figure 5.18, Figure 5.20, and Figure 5.22 is summarized in Table 5.7 along with other characteristics of the films and nanoparticle assemblies.

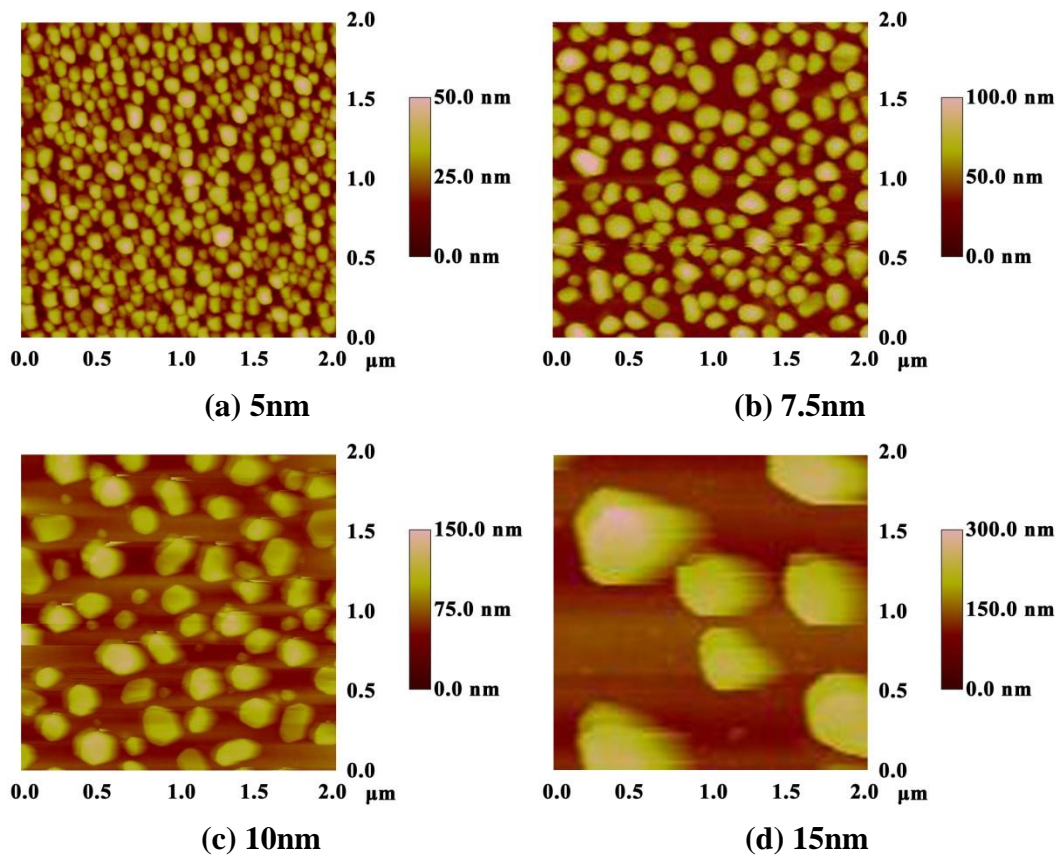


Figure 5.17: Atomic Force Microscopy images of the nanoparticles formed on the surfaces of the samples annealed at 700°C. The thickness of the gold nanolayer prior to annealing is (a) 5nm, (b) 7.5nm, (c) 10nm, and (d) 15nm.

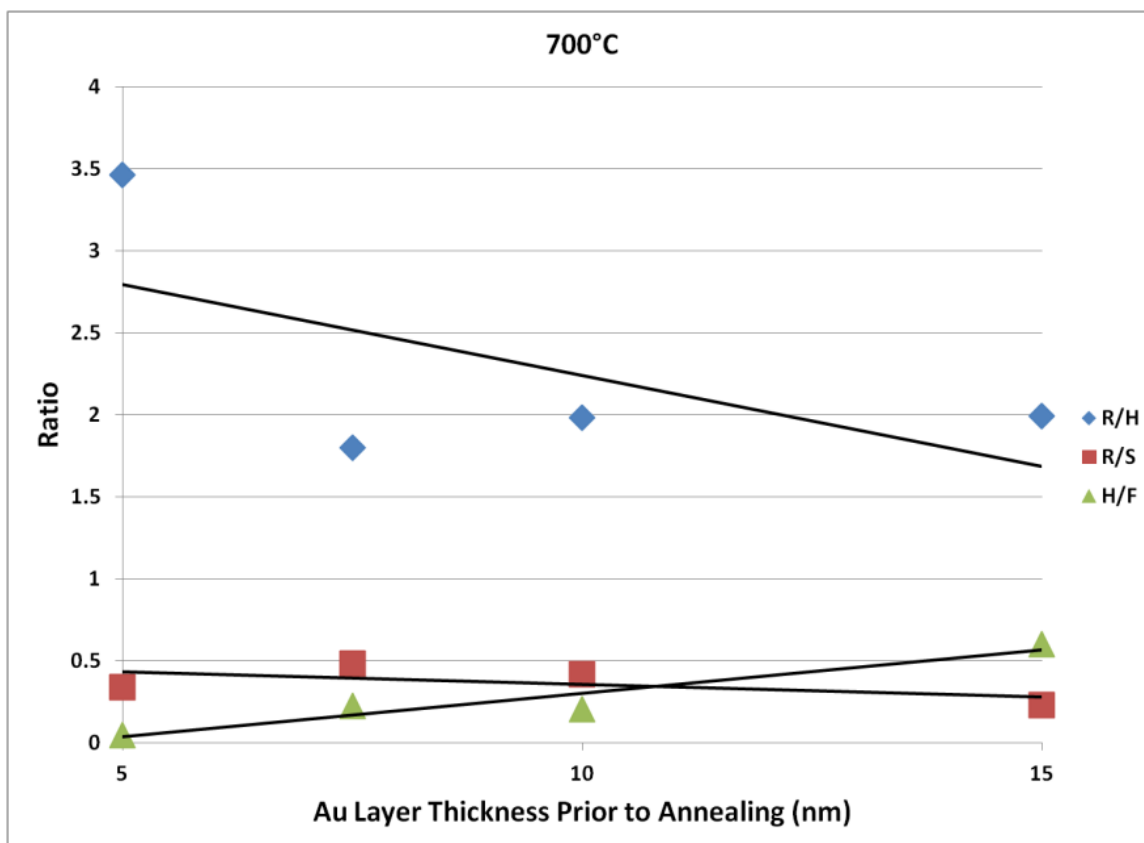


Figure 5.18: Ratios of the different dimensions and separations for the nanoparticles formed on the film surfaces of the samples annealed at 700°C. R/H is the nanoparticle radius-to-height ratio, R/S is the nanoparticle radius-to-separation ratio, and H/F is the nanoparticle height to sample film thickness ratio for each of the four samples annealed at 700°C.

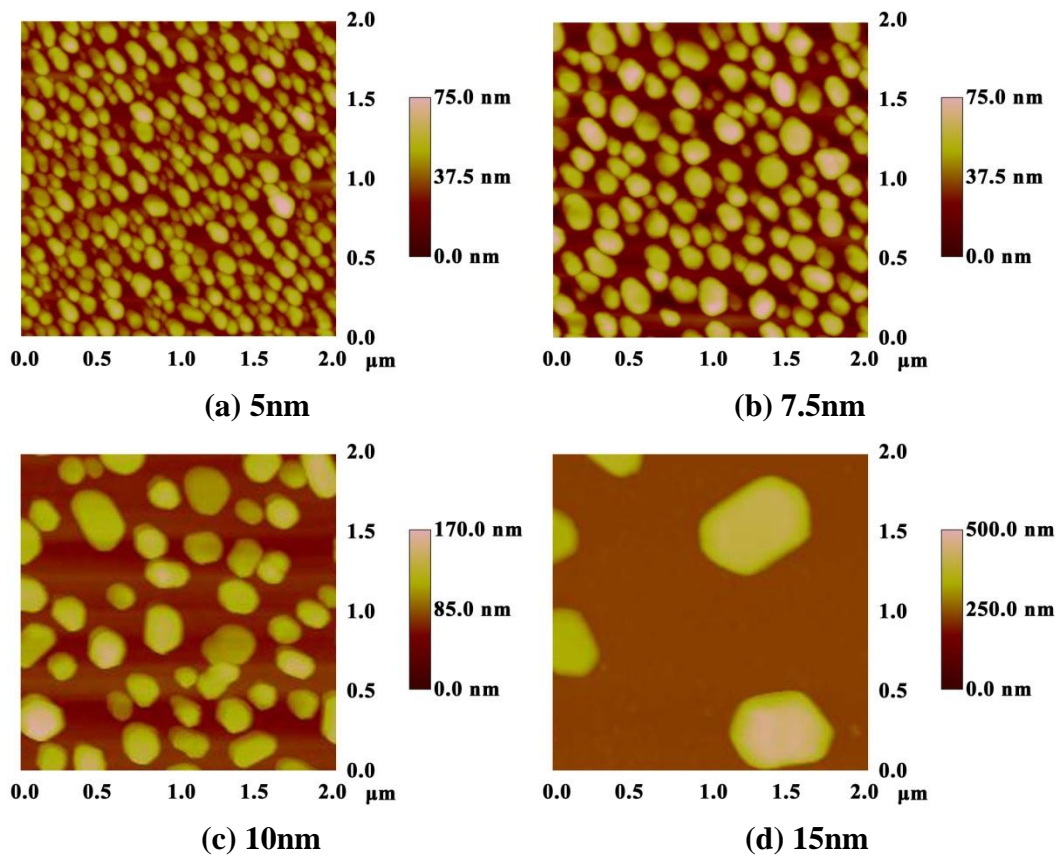


Figure 5.19: Atomic Force Microscopy images of the nanoparticles formed on the surfaces of the samples annealed at 800°C. The thickness of the gold nanolayer prior to annealing is (a) 5nm, (b) 7.5nm, (c) 10nm, and (d) 15nm.

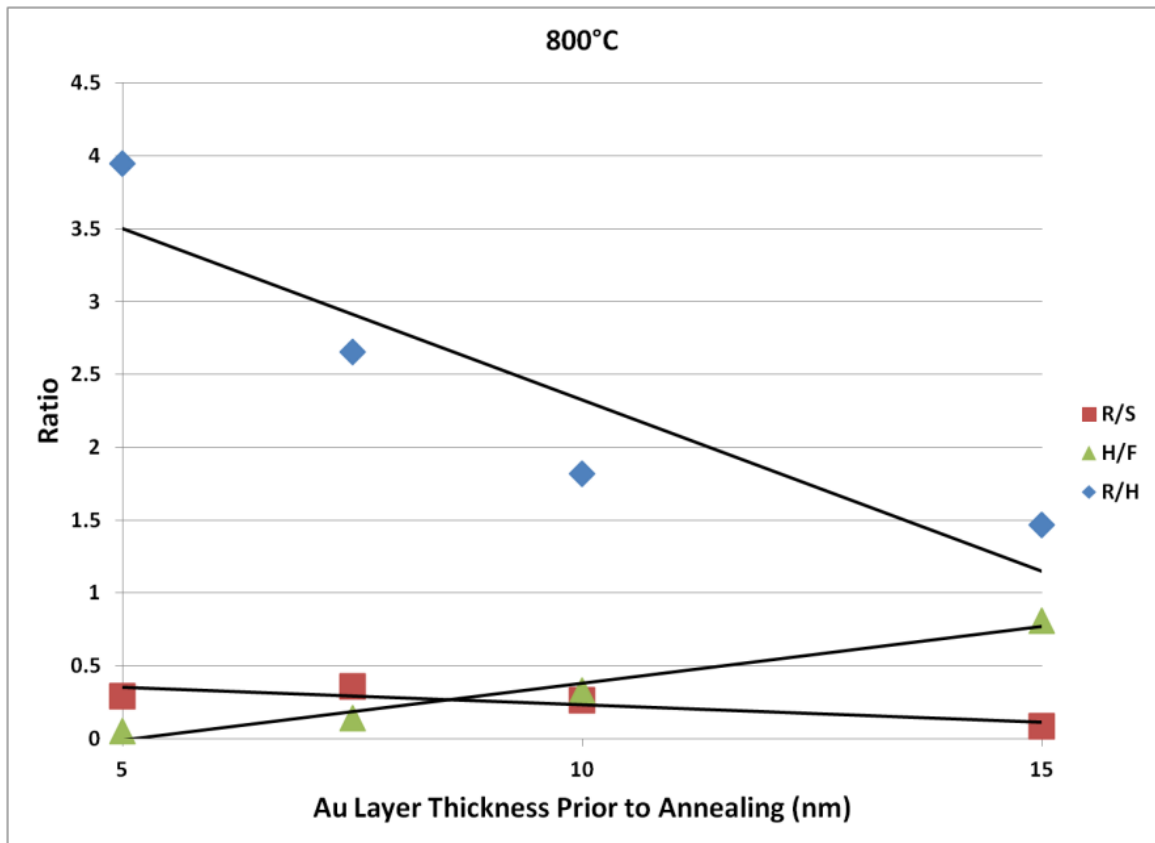


Figure 5.20: Ratios of the different dimensions and separations for the nanoparticles formed on the film surfaces of the samples annealed at 800°C. R/H is the nanoparticle radius-to-height ratio, R/S is the nanoparticle radius-to-separation ratio, and H/F is the nanoparticle height to sample film thickness ratio for each of the four samples annealed at 800°C.

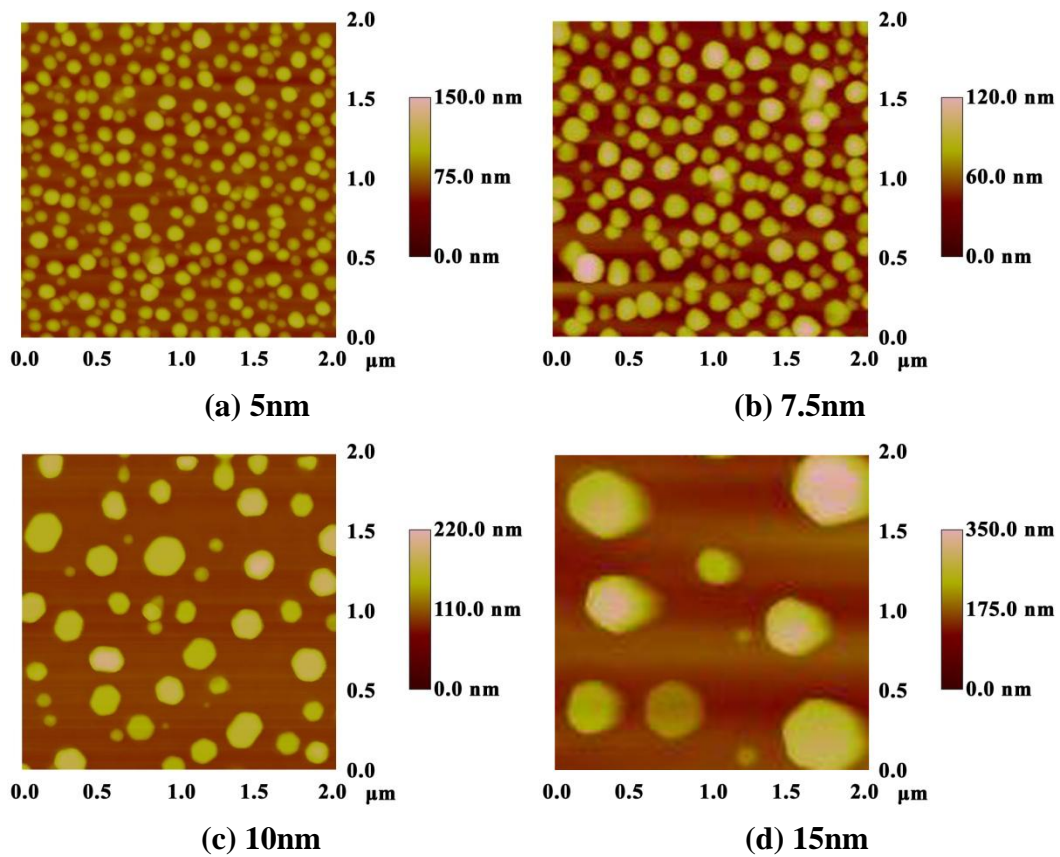


Figure 5.21: Atomic Force Microscopy images of the nanoparticles formed on the surfaces of the samples annealed at 1000°C. The thickness of the gold nanolayer prior to annealing is (a) 5nm, (b) 7.5nm, (c) 10nm, and (d) 15nm.

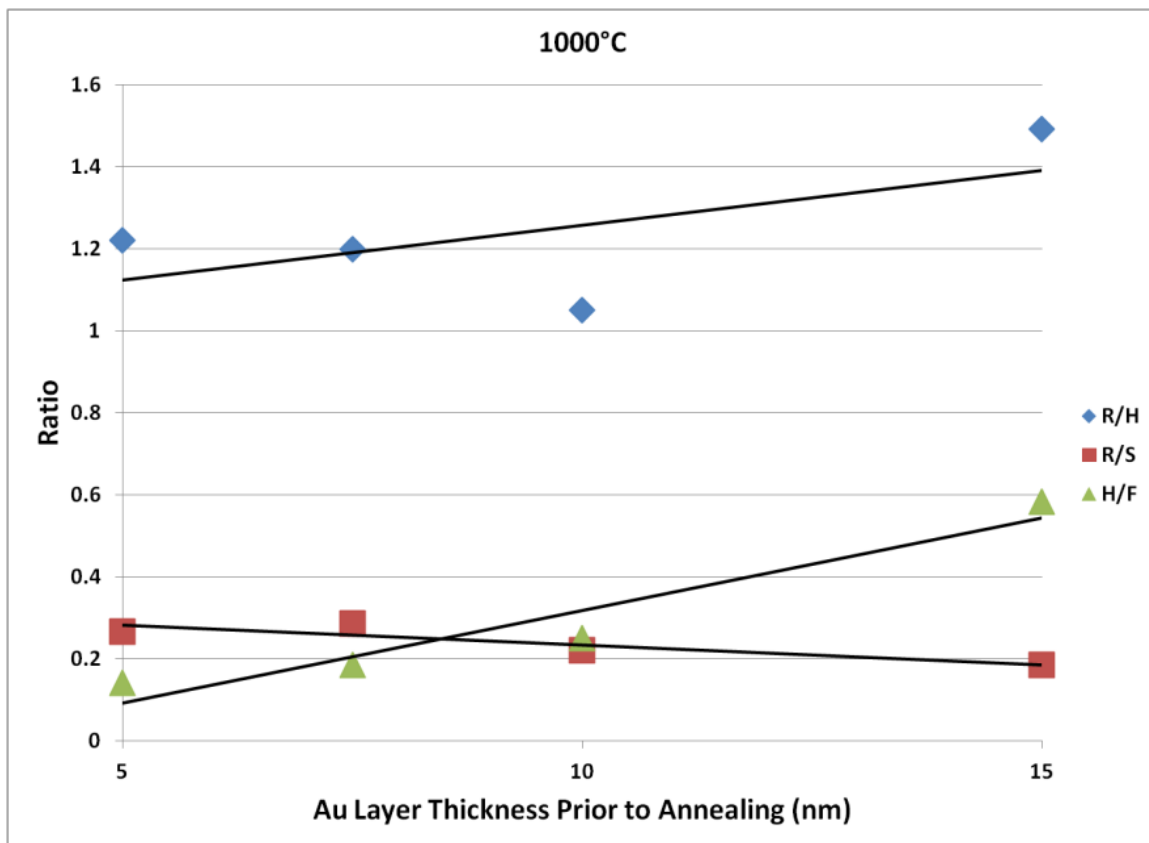


Figure 5.22: Ratios of the different dimensions and separations for the nanoparticles formed on the film surfaces of the samples annealed at 1000°C. R/H is the nanoparticle radius-to-height ratio, R/S is the nanoparticle radius-to-separation ratio, and H/F is the nanoparticle height to sample film thickness ratio for each of the four samples annealed at 1000°C.

Sample Name	UMD311-312	UMD311-313	UMD311-314	UMD311-315	UMD311-316	UMD311-317	UMD311-318	UMD311-319	UMD311-308	UMD311-310	UMD311-309	UMD311-311
Gold Layer (nm)	5	7.5	10	15	5	7.5	10	15	5	7.5	10	15
Annealing Temperature (°C)	700	700	700	700	800	800	800	800	1000	1000	1000	1000
Garnet Film Thickness (nm)	204	182	202	198	169	208	163	196	236	223	225	207
Nanoparticle Height (nm)	9.07	40.93	41.41	118.94	8.40	28.93	53.99	158.37	33.37	41.45	56.42	120.62
Δ Height (nm)	6.00	15.84	22.93	38.50	6.52	10.70	18.76	54.60	10.65	11.34	21.97	50.22
Nanoparticle Diameter (nm)	62.83	147.42	164.24	474.17	66.26	153.74	196.36	464.39	81.47	99.36	118.55	360.19
Δ Diameter (nm)	47.04	96.94	115.18	213.78	43.71	70.62	91.93	122.36	32.31	49.25	68.15	179.02
Nanoparticle Density (particles/μm)	64.50	18.40	12.99	1.24	58.23	17.92	8.22	0.88	54.34	32.73	14.97	1.51
Nanoparticle Spacing (nm)	69.45	100.96	138.63	466.01	74.56	98.16	174.89	720.13	60.61	85.91	154.72	484.59
R/H	3.47	1.80	1.98	1.99	3.95	2.66	1.82	1.47	1.22	1.20	1.05	1.49
R/S	0.34	0.48	0.42	0.23	0.29	0.36	0.26	0.08	0.27	0.29	0.22	0.18
H/F	0.04	0.22	0.20	0.60	0.05	0.14	0.33	0.81	0.14	0.19	0.25	0.58

Table 5.7: Summary of nanoparticle dimensions and separations as well as garnet film characterization for the twelve samples with different gold nanolayer thicknesses and annealing temperatures. R/H is the nanoparticle radius-to-height ratio, R/S is the nanoparticle radius-to-separation ratio, and H/F is the nanoparticle height to garnet film thickness ratio.

It has been observed that there is an increase in the H/F ratio as the gold nanolayer thickness is increased for the same annealing temperature for all three annealing temperatures and a decrease in the R/S ratio as the gold nanolayer thickness is increased for the same annealing temperature for all three annealing temperatures. The R/H ratio decreases with an increase in the gold nanolayer thickness for the 700°C and 800°C annealing temperatures but an increase is observed for the 1000°C annealing temperature although this could be due to an outlier reported for the sample that had a 15nm gold

nanolayer annealed at 1000°C. The density of the nanoparticles also decreases as the gold nanolayer thickness increases for all three annealing temperatures. These generalizations aid in a better understanding of how to obtain assemblies of gold nanoparticles with desirable dimensions and separations.

The extinction cross-sections of the nanoparticle assemblies for the twelve different samples can be found as the difference between the transmission measurements at various wavelengths performed before and after the deposition and annealing of the gold nanolayers on the surfaces of the garnet films. The plots of the extinction cross-sections for the twelve samples are shown in Figure 5.23, Figure 5.24, and Figure 5.25 for the annealing temperatures of 700°C, 800°C, and 1000°C, respectively. The peaks of the extinction cross-sections mostly coincide with the plasmon resonance wavelengths. It is expected based on theoretical grounds that the highest Faraday rotation enhancement will occur near the wavelengths where the extinction cross-section peaks occur.

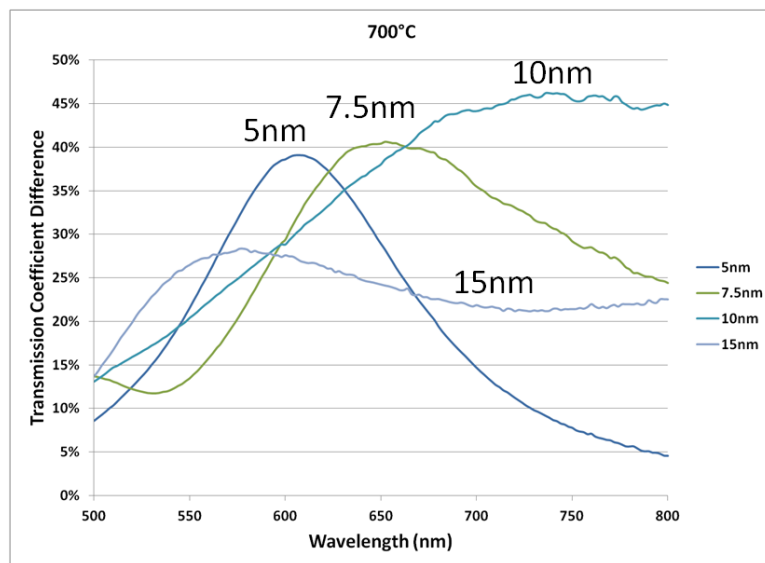


Figure 5.23: Transmission coefficient difference curves (extinction cross-sections) for the samples annealed at 700°C.

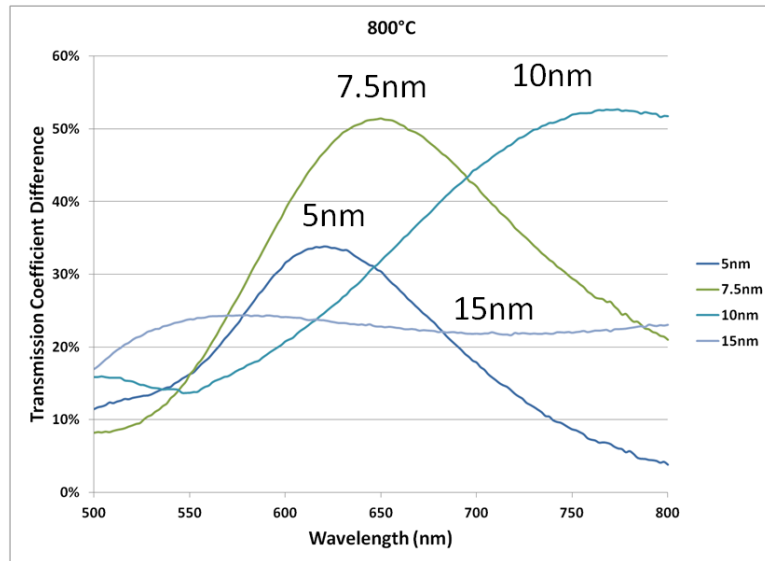


Figure 5.24: Transmission coefficient difference curves (extinction cross-sections) for the samples annealed at 800°C.

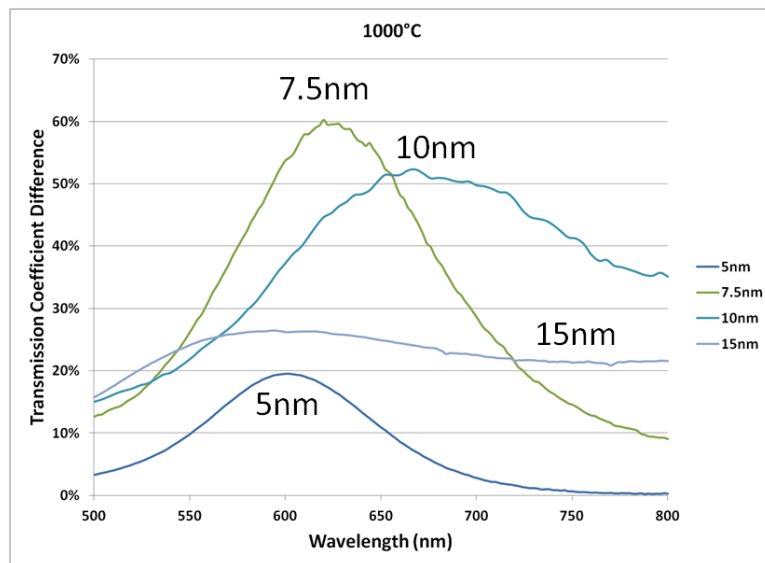


Figure 5.25: Transmission coefficient difference curves (extinction cross-sections) for the samples annealed at 1000°C.

As discussed in Chapter 3, the unique physical property of electrostatic resonances is that the resonance frequencies depend on the shape of the dielectric objects

but are scale invariant with respect to the geometric dimensions. This could be the cause of the broad peaks observed for the samples that had 10nm and 15nm nanolayers of gold prior to annealing since the shape of the nanoparticles formed on the surfaces of these samples are highly irregular in shape (see Figure 5.17, Figure 5.19, and Figure 5.21) which means the nanoparticles will resonate at different wavelengths.

Faraday rotation measurements have been performed by using the transmission ellipsometry technique described in Chapter 4. Measurements have been taken at 9 locations (see Figure 5.26) on the samples before gold has been deposited on the film surfaces and after gold has been deposited and annealed on the film surfaces. The samples have been saturated with a perpendicularly applied magnetic field at the measurement location. The measurements performed prior to deposition of gold have been compared to the measurements performed after the gold nanoparticles are formed on the film surfaces. The Faraday rotation enhancement is calculated as:

$$Enhancement = \frac{\theta_{F_{Au}} - \theta_F}{\theta_F} \quad (5.1)$$

where $\theta_{F_{Au}}$ is the Faraday rotation measured at a measurement location with gold nanoparticles on the film surface and θ_F is the Faraday rotation measurement at the same measurement location before the gold nanoparticles have been formed on the film surface (see Figure 5.27 as an example). The gaussmeter is used to ensure that the same magnetic field is applied during each measurement so that the results can be directly compared.

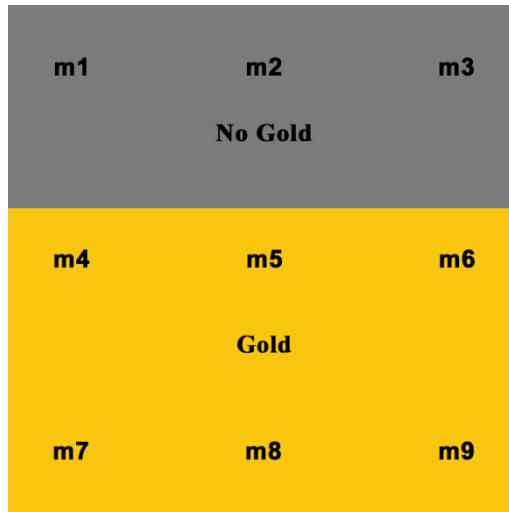


Figure 5.26: Outline of gold deposition pattern on garnet film surface. Marks m1-m9 correspond to the measurement locations. The size of the samples is 11mm x 11mm [Lang13].

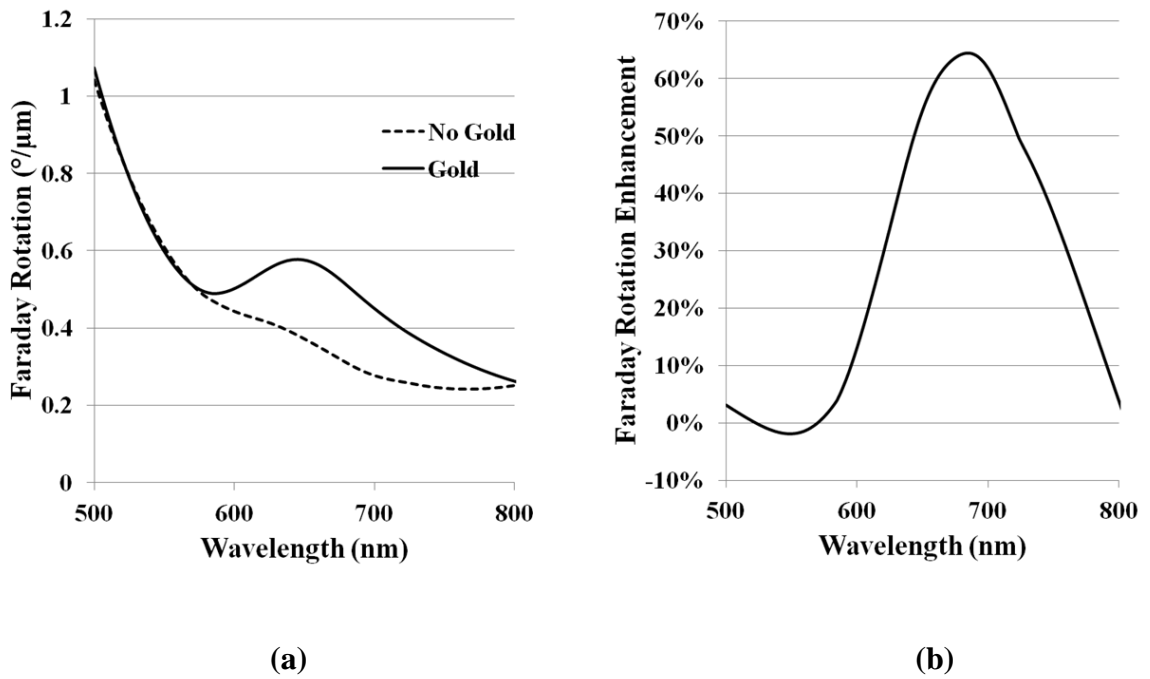


Figure 5.27: (a) Faraday rotation per unit length as a function of wavelength for one of the measurements for the sample that had 5nm of gold annealed at 800°C. (b) Faraday rotation enhancement as a function of wavelength for the same sample.

The Faraday rotation enhancement plots for measurements from all twelve samples are shown in Figure 5.28, Figure 5.29, and Figure 5.30 for annealing temperatures of 700°C, 800°C, and 1000°C, respectively. Smoothing is used due to the high level of noise observed when measuring very small values of Faraday rotation. The maximum enhancement values as well as the wavelengths at which the maximum has occurred for each sample are summarized in Table 5.8.

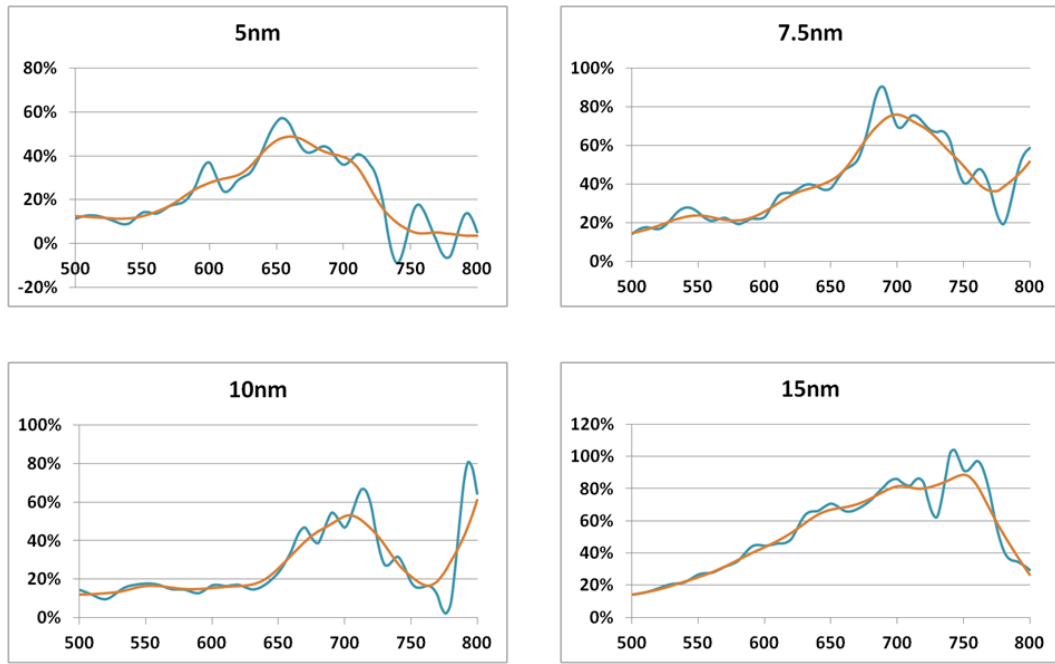


Figure 5.28: Faraday rotation enhancement plots for the four samples annealed at 700°C. The blue curves are the raw data curves and the green curves are the processed data curves after smoothing.

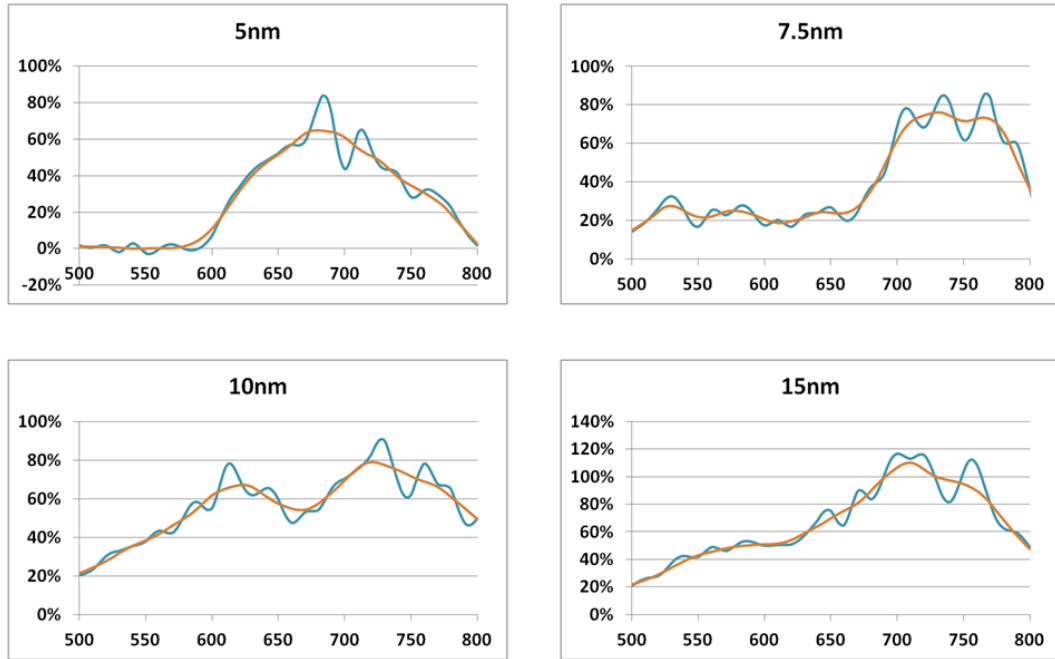


Figure 5.29: Faraday rotation enhancement plots for the four samples annealed at 800°C. The blue curves are the raw data curves and the green curves are the processed data curves after smoothing.

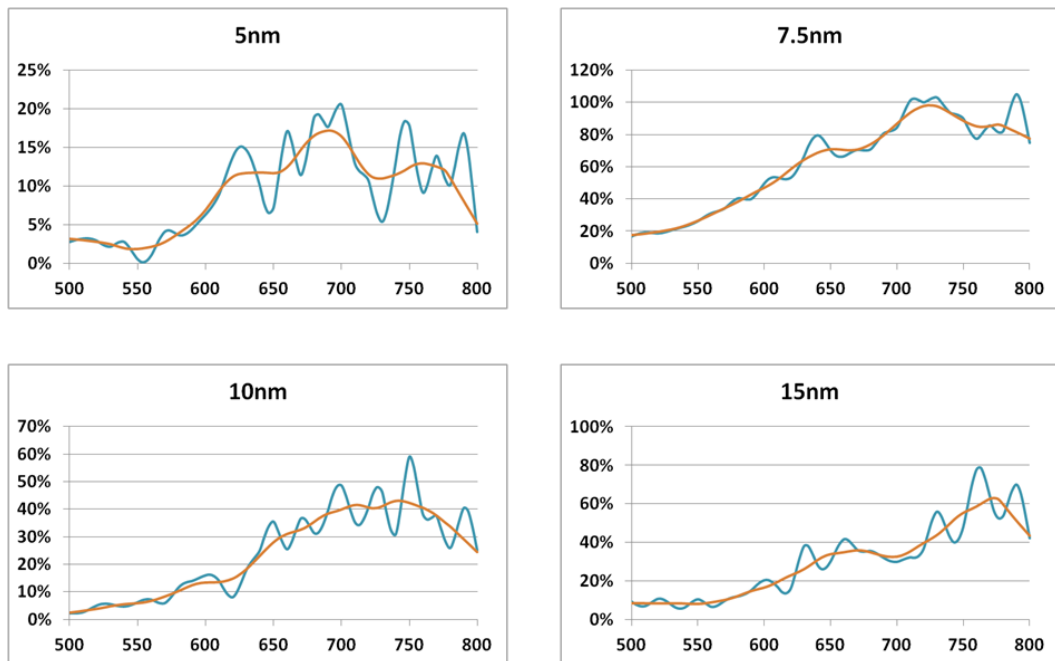


Figure 5.30: Faraday rotation enhancement plots for the four samples annealed at 1000°C. The blue curves are the raw data curves and the green curves are the processed data curves after smoothing.

Au layer (Before Annealing)	700°C (Maximum Enhancement)	800°C (Maximum Enhancement)	1000°C (Maximum Enhancement)
5nm	48% at 660nm	65% at 680nm	15% at 690nm
7.5nm	76% at 700nm	76% at 730nm	98% at 730nm
10nm	63% at 700nm	79% at 720nm	45% at 720nm
15nm	89% at 750nm	110% at 710nm	63% at 770nm

Table 5.8: Maximum Faraday rotation enhancement for each of the twelve samples and the wavelengths at which the maximum Faraday rotation enhancement has occurred. Each column in the table is for a different annealing temperature and each row in the table is for a different gold nanolayer thickness prior to annealing.

For the most part, general trends observed in Table 5.8 include an increase in Faraday rotation enhancement with an increase in the gold nanolayer thickness and an increase in the wavelength at which the maximum Faraday rotation enhancement occurs with an increase in the annealing temperature. While these trends are not supported by the measurements for all the samples, the data is fairly conclusive. Variations in these trends could be due to such variables as local film thickness, measurement error, and nanoparticle dimension non-uniformity.

The overall accuracy of the described transmission ellipsometry measurements is supported by Faraday rotation measurements performed using the improved optical hysteresis loop setup described in Chapter 4. Faraday rotation measurements have been performed at the wavelength of 633nm at the same measurement locations targeted in the case of the ellipsometry measurements. First, these measurements have been carried out for each sample before the gold deposition and after the gold deposition but prior to its

annealing, and no difference in Faraday rotation has been observed for any of the samples. Then, the same measurements have been carried out after the gold annealing and Faraday rotation enhancement has been observed. While the Faraday rotation enhancement varies slightly at the different locations on the samples, the average of the Faraday rotation enhancements observed using laser measurements coincide with the results found from the transmission ellipsometry measurements at the same wavelength of 633nm.

The experimental observations indicate that the dimensions and separations of the gold nanoparticles appreciably impact the Faraday rotation enhancement of thin garnet films. There is a strong correlation between the nanoparticle height to garnet film thickness ratio (H/F) and the enhancement of the Faraday rotation observed for the same sample. The larger the H/F ratio and the larger the particle separation, the higher the extent of penetration of the plasmon resonance induced electric fields into the garnet films and the stronger the Faraday rotation enhancement. This suggests that the Faraday rotation enhancement can be controlled by inducing plasmon resonances in gold nanoparticles formed by annealing nanolayers of gold of various thicknesses at various temperatures.

Conclusion and Future Work

Plasmon resonance induced Faraday rotation enhancement in garnet films offers the promise for development of compact and higher performance polarization dependent optical devices. Liquid phase epitaxy grown garnet films have been developed with gold nanoparticles on or in the films. Enhancement of Faraday rotation has been achieved for these films utilizing strong localized electric fields induced by the excitation of plasmon resonances in the gold nanoparticles. The enhancement is governed by the thickness of the garnet films, the dimensions and separations of the nanoparticles assemblies, and the relative ratio between the height of the nanoparticles and the thicknesses of the films.

For the samples with embedded nanoparticles, there have been noticeable effects on the magnetic properties of the films due to the presence of the gold nanoparticles embedded in the films. Films have been grown over gold nanoparticles from both melts that resulted in films with in-plane magnetization and film composition $(\text{Bi, Pr, Y, Gd})_3(\text{Fe, Ga})_5\text{O}_{12}$, and melts that resulted in films with out-of-plane magnetization and film composition $(\text{Bi, Gd, Lu})_3(\text{Fe, Ga})_5\text{O}_{12}$. In some cases, negative enhancement has been observed, meaning that the Faraday rotation has actually been reduced due to the presence of the nanoparticles embedded in the films, likely due to effects that the nanoparticles have on the magnetic and material properties of the films. As a byproduct of the research, it has been realized that the embedding of gold nanoparticles in the garnet films can be used to control the local anisotropy of the films.

While the extent of penetration of the induced electric fields is greater for nanoparticles embedded in the films, it is more difficult to control the shape and distribution of the nanoparticles once a film has been epitaxially grown over the

nanoparticles. In order to embed nanoparticles in the films, the thickness of the films grown over the nanoparticles is limited by a minimum growth rate necessary to trap the nanoparticles at the film/substrate interface. Limitations in the growth process for samples with embedded nanoparticles have led to the development of samples with gold nanoparticles incorporated on the surfaces of the films.

Special efforts have been made to improve the growth process and produce sub-micron thick films with thicknesses around 200nm to ensure that the induced electric fields are uniformly spread over the thickness of the films. At this thickness, nanoparticles have been incorporated on the surface of the LPE grown garnet films rather than embedded in the films due to the low growth rate necessary to grow the films. New techniques have been developed to increase the accuracy of Faraday rotation enhancement measurements. Faraday rotation enhancement as high as 110% has been observed for samples with nanoparticle assemblies on the surfaces of the films but the enhancement depends on a number of factors and can be substantially lower.

The distribution and dimensions of nanoparticle assemblies can be controlled better when the nanoparticles are formed on the surface of the films and therefore, the Faraday rotation enhancement can be effectively controlled. Nanoparticle assemblies can be formed in such a way that the resonance wavelength can be shifted to a desired range in the dispersion relation of the gold nanoparticles where a higher potential enhancement is possible. Stronger enhancement can be achieved by increasing the ratio between the height of the nanoparticles and the thickness of the films (H/F) as well as increasing the relative spacing between nanoparticles.

There is still room for improvement in the garnet film growth process and gold nanoparticle formation process that could potentially lead to stronger enhancement of the Faraday rotation than has already been observed. As a future project, there is interest in developing multi-layer films with nanoparticles embedded between each layer of the films. With a multi-layer design, plasmon resonance induced electric fields could penetrate both layers surrounding the nanoparticles, hence increasing the extent of penetration of the induced electric fields and ensuring there is a uniform spreading of the electric fields throughout the thickness of the films. This design could lead to the development of films that exhibit strong Faraday rotation enhancement while also providing flexibility in terms of the overall thickness of the multi-layer films by controlling how many sub-micron thick layers are grown on top of one another.

Bibliography

- [BaWa88] L. Baselgia, M. Warden, et al., “Derivation of the resonance frequency from the free energy of ferromagnets”, *Physical Review B*, **38**, 2237 (1988).
- [Berk81] G. W. Berkstresser, and S. L. Blank, “LPE of LuLaSmGaFe garnet from a PbO-V₂O₅ flux”, *Journal of Applied Physics*, **52**(3), 2332 (1981).
- [Blan72] S. L. Blank, and J. W. Nielsen, “The Growth of Magnetic Garnets by Liquid Phase Epitaxy”, *Journal of Crystal Growth*, **17**, 302-311 (1972).
- [Chik78] Chikazumi, Soshin. *Physics of Magnetism*. Translated by Stanley H Charap. Huntington: Robert E. Krieger Publishing Company (1978).
- [Cres12] M. Crescimanno, G. Mao, J. H. Andrews, K. D. Singer, E. Baer, A. Hiltner, H. Song, K. Comeau, B. Shakya, A. Bishop, and R. Livingston, “The role of group velocity delay in Faraday rotation in a multilayer polymer lattice”, *accepted to appear in the Journal of the Optical Society of America B* (2012).
- [Cros68] W. A. Crossley, R. W. Cooper, J. L. Page, and R. P. van Stapele, “Faraday Rotation in Rare-Earth Iron Garnets”, *Physical Review*, **181**(2), 896-904 (1968).
- [dAqu04] M. d'Aquino, “Nonlinear Magnetization Dynamics in Thin-films and Nanoparticles”, *PhD Dissertation Thesis*, University of Naples (2004).
- [Esch81] A. H. Eschenfelder, “Magnetic Bubble Technology”, *Springer-Verlag*, New York (1981).
- [Frat86] V.J. Fratello, S. E. G. Slusky, C.D. Brandle and M.P. Norelli. “Growth-Induced Anisotropy in Bismuth-Rare Earth Iron Garnets”, *Journal of Applied Physics*, **60**, 2488 (1986).
- [FrMa03] D. R. Fredkin, and I. D. Mayergoyz, “Resonance Behavior of Dielectric Objects (Electrostatic Resonances)”, *Physical Review Letters*, **91**, 253902 (2003).
- [Fuji08] R. Fujikawa, A. V. Baryshev, J. Kim, H. Uchida, and M. Inoue, “Contribution of the surface plasmon resonance to optical and magneto-optical properties of a Bi:YIG-Au nanostructure”, *Journal of Applied Physics*, **103**, 07D301 (2008).

- [GeGi57] S. Geller, and M. A. Gilleo, "The Crystal Structure and Ferrimagnetism of Yttrium-Iron Garnet, $Y_3Fe_2(FeO_4)_3$ ", *Journal of Physics and Chemistry of Solids*, **3**, 30-36 (1957).
- [GiGe58] M. A. Gilleo, and S. Geller, "Magnetic and Crystallographic Properties of Substituted Yttrium-Iron Garnet", *Physical Review*, **110**(1), 73-78 (1958).
- [Gilb04] T. L. Gilbert, "A Phenomenological Theory of Damping in Ferromagnetic Materials", *IEEE Transactions on Magnetics*, **40**(6), 3443-3449 (2004).
- [Holt04] C. Holthaus, "Development of sensitive indicators for magneto-optical pattern recognition", *PhD Dissertation Thesis*, University of Osnabrück (2004).
- [JAWo10] J. A. Woollam Co., Inc., "Chapter 2: A Short Course in Ellipsometry", *J. A. Woollam Co., Inc.* (2010).
- [JoCh72] P. B. Johnson, and R. W. Christy, "Optical Constants of the Noble Metals", *Physical Review B*, **6**, 4370-4379 (1972).
- [Kore79] R. Korenstein, and C. A. Castro, "LPE growth of double layer structures from molybdate and lead borate fluxes", *Journal of Applied Physics*, **50**(11), 7830 (1979).
- [LaLi84] L.D. Landau and E.M. Lifshitz, "Electrodynamics of continuous media", *Pergamon Press*, New York (1984).
- [Lang12] G. Lang, D. Bowen, L. Hung, C. Krafft, and I. Mayergoyz, "Anisotropy study of garnet films grown over substrates populated with gold nanoparticles", *Journal of Applied Physics*, **111**, 07A505 (2012).
- [Lang13] G. S. Lang, D. Bowen, C. Krafft, and I. D. Mayergoyz, "Deposition of gold nanoparticles on liquid phase epitaxy grown garnet films and Faraday rotation enhancement", *Journal of Applied Physics*, **113**, 17A929 (2013).
- [Magn07] V. Magnasco, "Elementary Methods of Molecular Quantum Mechanics", *Elsevier* (2007).
- [MaRu77] D. Mateika, and C. Rusche, "Coupled substitution of gallium by magnesium and zirconium in single crystals of gadolinium gallium garnet", *Journal of Crystal Growth*, **42**, 440 (1977).

- [MaSI79] Malozemoff, A P, and J C Slonczewski. *Magnetic Domain Walls in Bubble Materials*. Applied Solid State Science. New York: Academic Press (1979).
- [Maye10] I. D. Mayergoyz, G. Lang, L. Hung, S. Tkachuk, C. Krafft, and O. Rabin, “Plasmon resonance enhancement of magneto-optic effects in garnets”, *Journal of Applied Physics*, **107**, 09A925 (2010).
- [MaZM07] I.D. Mayergoyz, Z. Zhang, and G. Miano, “Analysis of Dynamics of Excitation and Dephasing of Plasmon Resonance Modes in Nanoparticles”, *Physical Review Letters*, **98**, 147401 (2007).
- [Niel58] J. W. Nielsen, and E. F. Dearborn, “The growth of single crystals of magnetic garnets”, *Journal of Physics and Chemistry of Solids*, **5**, 202 (1958).
- [Niel76] J. W. Nielson, “Bubble Domain Memory Materials”, *IEEE Transactions on Magnetics*, **12**(4), 327-345 (1976).
- [NiHo06] I. Nistor, C. Holthaus, I. D. Mayergoyz, and C. Krafft, “Determination of Layer-Specific Magnetization and Anisotropy Fields in Multilayer Garnet Films From FMR and VSM Measurements”, *IEEE Transactions on Magnetics*, **42**, 3261 (2006).
- [Nist06] I. Nistor, “Development of magnetic field sensors using Bismuth-substituted garnets thin films with in-place magnetization”, *PhD Dissertation Thesis*, University of Maryland (2006).
- [Pers67] P. S. Pershan, “Magneto-Optical Effects”, *Journal of Applied Physics*, **38**, 1482 (1967).
- [Skom087] R. Skomski, “Simple Models of Magnetism”, *Oxford University Press* (2008).
- [Smir03] B. M. Smirnov, “Physics of atoms and ions”, *Springer-Verlag New York, Inc*, 254-272 (2003).
- [STka11] S. Tkachuk, “Research and Development of Thin Garnet Film Based Magneto-Optical Imagers”, *PhD Dissertation Thesis*, University of Maryland (2011).
- [StSi06] J. Stohr, and H. C. Siegmann, “Magnetism from Fundamentals to Nanoscale Dynamics”, *Springer-Verlag Berlin Heidelberg* (2006).

- [Tkac11] S. Tkachuk, G. Lang, C. Krafft, O. Rabin, and I. Mayergoyz, “Plasmon resonance enhancement of Faraday rotation in thin garnet films”, *Journal of Applied Physics*, **109**, 07B717 (2011).
- [Uchi09] H. Uchida, Y. Masuda, R. Fujikawa, A. V. Baryshev, and M. Inoue, “Large enhancement of Faraday rotation by localized surface plasmon resonance in Au nanoparticles embedded in Bi:YIG films”, *Journal of Magnetism and Magnetic Materials*, **321**, 843-845 (2009).
- [Wett76] W. Wetting, “Magneto-optics of ferrites”, *Journal of Magnetism and Magnetic Materials*, **3**, 147-160 (1976).
- [Zhan04] J. Zhang, “Growth and FMR characterization of in-plane magnetization garnet thin films”, *Master Thesis*, University of Maryland (2004).
- [Zvez97] A. K. Zvezdin, and V. A. Kotov, “Modern Magneto-optics and Magneto-optical Materials”, *IOP Publishing Ltd*, Philadelphia (1997).